Venous Thrombosis: Formation, Evolution And Resolution Imaging Using Non-Invasive MRI Techniques

Andia Kohnenkampf, Marcelo

Awarding institution:
King's College London

Venous Thrombosis: Formation, Evolution And Resolution Imaging Using Non-Invasive MRI Techniques

Marcelo E. Andia-Kohnenkampf

Thesis submitted for the degree of
Doctor of Philosophy
2012

Division of Imaging Sciences and Biomedical Engineering
School of Medicine
King's College London

Statement of originality

The work contained in this thesis is my own original work, except where acknowledged in the text.

Acknowledgements

I would like to thank my supervisor Professor Rene Botnar for his continued support, guidance, advice and kindness. He has been a great model of passion for research.

I would also like to express my gratitude to Dr Andrea J Wiethoff and Professor Alberto Smith for their advice and discussion during the developing of this work.

I would like to acknowledge Mr David Eastham and Mr David Thakor for technical assistance, and the financial support of the Chilean Agency for Research in Science and Technology (CONICYT).

Most importantly I would like to thank Dr Prakash Saha, without his hard work and commitment, this work would never have been possible. I am grateful for his friendship and for his scientific rigor.

Finally, I would thank my family: mum and dad for all their sacrifices and unconditional love, what I am and what I am not, I owe it to them; and Antonieta, Sofia and Joaquin, the true reasons of my life.

Abstract

Deep venous thrombosis (DVT) remains a major health problem. Although thrombolytic therapies are effective in recanalising the veins, restoring blood flow, preventing pulmonary embolism and post-thrombotic complications, there is still no consensus on the selection criteria for this invasive treatment. Experimental data suggest that thrombus rich in fibrin has better response to thrombolysis than red cell rich (acute phase) or collagen rich (chronic) thrombus. Thus, there is a need for a diagnostic technique that provides better information on the stage of thrombus organization in-vivo and allows identification of thrombus suitable for thrombolysis.

Current imaging modalities for the diagnosis of DVT do not provide information on the biological stage of thrombus organization. Contrast venography is still considered the gold standard for the diagnosis of DVT, even though thrombi are not clearly visualized and they are indirectly detected due to alterations in blood flow.

The aim of this thesis was to develop and validate new imaging methodology for the better evaluation of DVT using Magnetic Resonance Imaging (MRI). The first aim was to investigate the potential of non-contrast enhanced MRI sequences including T1 mapping, T2* mapping, Magnetization Transfer Contrast (MTC), and Apparent Diffusion Coefficients (ADC) maps for the detection of thrombus in a murine model of deep venous thrombosis. The second aim was to investigate the merit of a fibrin and macrophage specific MR contrast agent for the detection of DVT. Both fibrin and macrophages play a major role in thrombus organization. The third aim was to investigate the merits of the fibrin binding contrast agent for the guidance of thrombolysis. We also developed two new non-contrast enhanced venous spin labelling approaches in order to obtain venograms without the need of a contrast agent and thereby to improve non-invasive DVT diagnosis using MRI.

In conclusion, this thesis proposes a new imaging methodology for the accurate staging of thrombus organization and the successfully detection of thrombus amenable for thrombolysis in a murine model of DVT. The translation of this technique into the clinic should have great potential to change clinical evaluation and treatment of patients with DVT.

Table of Contents

Index of Figures

Chapter 1

Chapter 2

Chapter 3

Chapter 4

Chapter 5

Chapter 6

Chapter 7

Index of Tables

Chapter 1

Chapter 2

Chapter 6

Abbreviations

ΔB	Magnetic field inhomogeneity
Δf	Frequency offset
2D	Two dimensional
3D	Three dimensional
ADC	Apparent diffusion coefficient
ANOVA	Analysis of variance
Ao	Aorta
ASL	Arterial spin labelling
AUC	Area under curve
b-SSFP	Balanced Steady-State Free Precession
CDT	Catheter-directed thrombolysis
CE-MRA	Contrast-enhanced Magnetic Resonance Angiography
CI95%	95% confidence interval
CNR	Contrast-to-noise ratio
CT	Computed tomography
DVT	Deep Vein Thrombosis
DIR	Dual-inversion recovery
DTMRI	Direct thrombus magnetic resonance imaging
ECG	Electrocardiography
Fe2+	Ferrous iron
Fe3+	Ferric iron
FFE	Fast field echo
FOV	Field of view
FSMRI	Fibrin specific magnetic resonance imaging
Gd	Gadolinium
GRE	Gradient-echo
H&E	Haematoxylin and eosin
Hb	Haemoglobin
ICP-MS	Inductively coupled plasma mass spectrometry

IR	Inversion recovery
IVC	Inferior vena cava
KCN	Potassium cyanide
LGE-IR	Late gadolinium enhanced inversion recovery
MetHb	Methemoglobin
mM	Millimolar
MRDTI	Magnetic resonance direct thrombus imaging
MRI	Magnetic resonance imaging
MSB	Martius/scarlet/blue
MTC	Magnetization Transfer Contrast
MTR	Magnetization Transfer ratio
Mxy	Transverse magnetization
Mz	Longitudinal magnetization
NSF	Nephrogenic Systemic Fibrosis
PD	Proton density
PE	Pulmonary embolism
PMNs	Polymorphoneuclear neutrophils
PTS	Post-thrombotic syndrome
QIR	Quadruple inversion recovery
RBCs	Red blood cells
RCT	Randomized controlled trial
RF	Radio frequency
ROC	Receiver operating characteristic
ROS	Reactive oxygen species
SD	Standard deviation
SE	Spin-echo
SNR	Signal to noise ratio
SSFP	Steady-state free precession
T1	Spin-lattice relaxation time
T2	Spin-spin relaxation time
T2*	T2 star relaxation time

T2prep	T2 preparation prepulse
TE	Echo time
TFE	Turbo-field-echo
Th	Thrombus
TI	Inversion time
TIR4ASL	Triple Inversion Recovery Prepulse for Arterial spin labelling
TOF	Time-of-flight
tPA	Tissue plasminogen activator
TR	Repetition time
USPIO	Ultrasmall superparamagnetic iron oxide nanoparticles
VENC	Velocity encoding value
VSOP	Very small iron oxide particle
VT	Venous thromboembolism

Chapter 1 Introduction

1.1 Deep Vein Thrombosis overview

Deep venous thrombosis (DVT) and pulmonary embolism (PE) are manifestations of a single disease entity, namely, venous thromboembolism (VT). Thrombus is an aggregation of platelets, fibrin, coagulation factors and cellular elements of blood attached to the interior wall of a vein or artery, causing a total or partial obstruction of blood flow. If venous thrombus forms in the deep veins of the leg or arm, it is termed Deep Vein Thrombosis (DVT) (1,2).

DVT and their most common complication, pulmonary embolism (PE), are major causes of morbidity and death. The average annual incidence of venous thromboembolism in Western countries is approximately 1–2 per 1,000 person-years. Each year, in the US, two million patients suffer from DVT and more than 600,000 develop PE (3,4).

The pathophysiology of VT involves three interrelated factors ("Virchow's triad") (5): damage to the vessel wall, slowing down of blood flow and a prothrombotic state. The classic risk factors for VT include: age, cancer, major surgery, immobilisation, pregnancy, use of oestrogens and thrombophilic abnormalities (antiphospholipid syndrome, deficiencies of antithrombin, protein C, protein S and factor V Leiden) (6).

VT now is recognized as a chronic disease with episodic recurrence. About 30% of patients develop recurrence within the next 10 years of its first episode (7). The observed survival after VT is significantly worse than the expected survival for age and gender, and survival after PE is worse than after DVT alone (8).

The clinically important problems associated with DVT are: death from PE, morbidity resulting from the acute event, recurrent venous thromboembolic events, and post-thrombotic syndrome (PTS) (8,9).

Despite the use of the traditional anticoagulant therapy, re-thrombosis and PTS are still the most common chronic sequels after a DVT event (7-9). PTS has a cumulative incidence of 20 to 50% two years post DVT (10,11). PTS is characterized by persistent limb pain, swelling and ulceration (Figure 1.1, (12)). These conditions lead to reduced quality of life and disability. Most patients affected are of working age, resulting in a significant social cost (11). The cost of managing venous ulcers in the United Kingdom alone was estimated to be £600 million per year

(13). The annual expenditure on DVT in the US including the managing of PTS totalled $1.5 billion, and patients with recurrent DVT or severe PTS doubling the average health care cost for DVT (14).

Figure 1.1- Clinical manifestation of post-thrombotic syndrome (PTS) (12)

The pathophysiology of PTS is incompletely understood, but it is thought that the acute thrombus itself, associated inflammatory mediators, and the process of thrombus organization and vein recanalization induces damage to the venous valves, leading to incompetence (reflux) (10,15). Valvular incompetence and persistent venous obstruction cause venous hypertension, which leads to oedema, tissue hypoxia, and skin ulceration (Figure 1.2 (16)).

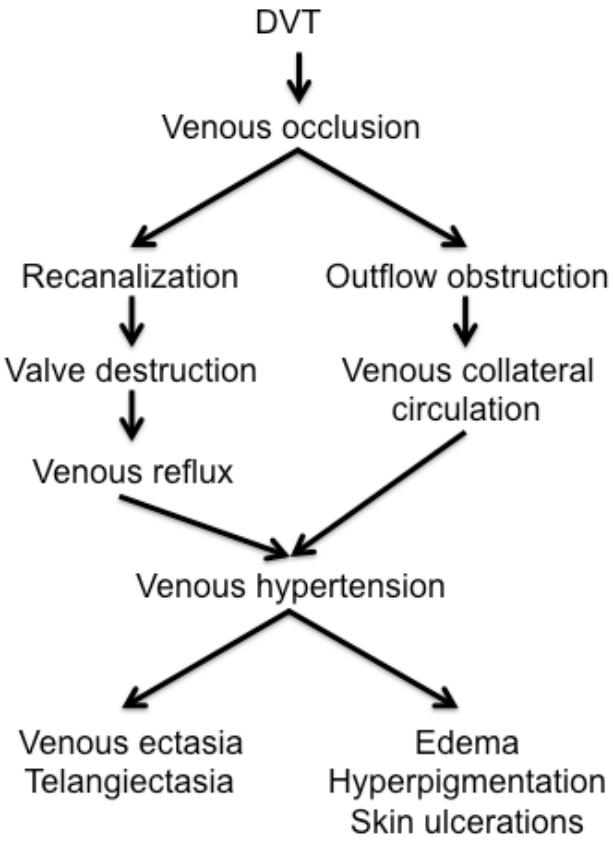

Figure 1.2- Schematic pathophysiology of the post-thrombotic syndrome (PTS) (16)

It has been hypothesized for many years that rapid thrombus elimination and restoration of venous flow may prevent valvular reflux, venous obstruction, and PTS, the so called “open vein hypothesis” (17). Recently it has been shown that thrombolytic therapies for DVT recanalize the veins more quickly and are associated with less recurrence, preservation of venous valve function, and fewer post-thrombotic complications (18-20), however they still have a low success rate of venous recanalization. The selection criteria for DVT patients amenable for systemic thrombolysis are still under discussion, mainly because of the high complication rate of bleeding (21). The introduction of catheter-directed thrombolysis (CDT) is thought to improve results and decrease the rate of complications but selection criteria are not well established yet. Experimental data suggest that young thrombus rich in fibrin has a better response to thrombolysis than old, collagen rich thrombus (22). Thus, there is a need for more objective criteria based on thrombus composition rather than morphology or duration of symptoms to better identify patients eligible for thrombolytic therapy (19,23,24).

1.2 Diagnosis of DVT

DVT acutely presents with calf pain and swelling that is commonly unilateral. The differential diagnosis includes cellulitis, ruptured Baker's cyst, muscular injury, tumour, popliteal aneurysm, Achilles tendon inflammation or rupture, and lymphedema (2,25,26). The clinical diagnosis of DVT is challenging, mainly because calf pain and leg swelling are non-specific symptoms. A combination of risk stratification, D-dimer testing, and imaging to assess venous flow are currently used (27,28). No single marker or modality is, however, able to determine acute thrombosis accurately.

Scoring systems that combine history and clinical examination can help predict the probability of DVT. The Wells' Criteria (28) or similar modified systems are widely used in clinical practice (Table 1.1).

Clinical feature	Score
Active cancer (treatment on-going or within the previous 6 months or palliative)	+1
Paralysis, paresis, or recent plaster immobilization of the lower extremities	+1
Recently bedridden for more than 3 days or major surgery within 4 weeks	+1
Localized tenderness along the distribution of the deep venous system	+1
Entire leg swollen	+1
Calf swelling by more than 3 cm when compared to the asymptomatic leg (measured below tibia tuberosity)	+1
Pitting oedema (greater in the symptomatic leg)	+1
Collateral superficial veins (non-varicose)	+1
Alternative diagnosis as likely or greater that that of DVT	-2
Additional feature in the Modified Wells Score	
Previously documented DVT	+1

Note: Risk category: low risk < 1 point; intermediate risk = 1 or 2 points; high risk > 2 points

Table 1.1- Clinical model for predicting pre-test probability for DVT (The Well's Criteria) (27,28)

The D-dimer blood test demonstrates the presence of blood clot degradation products. It has a sensitivity of 95.3% and specificity of 44.7% for DVT diagnosis. The negative predictive value is high at 97.7%, making it a useful test for ruling out DVT (29). A negative D-dimer blood test and

a Wells scores <1 are effective for ruling out DVT without the need for any imaging test. Those not excluded, however, require imaging to confirm thrombosis before commencing therapy.

The currently available imaging techniques for the diagnosis of DVT include: contrast venography and non-invasive radiological methods. Contrast venography (also called phlebography) is still considered the gold standard for the diagnosis of DVT (30,31). This X-ray examination provides an image of the veins after an iodinated contrast agent is injected into a dorsal foot vein. Main findings with this technique are filling defect, interruption of contrast in a vein and collateral branches. Phlebography relies on the anatomy of the venous system, lacking physiological information. Additionally, this technique is also invasive, expensive, exposes the patient to a high dose of radiation, and can cause complications related to nephrotoxicity and allergic reactions to iodinated contrast agents (32). Additionally, most guidelines suggest avoiding the use of iodinated contrast agents in pregnant women, elderly and patients with renal dysfunction (33-35), who, paradoxically, are the patients with highest risk of developing DVT (6).

Venous ultrasonography imaging (with Doppler and compression technique) is most widely used due to its high accuracy, relatively low cost and lack of ionizing radiation (30). However, this technique is very “operator-dependent”, its application is limited to easily compressible venous areas (lower limb for example) and only provides information about vein morphology and blood flow velocity (36). With this technique, thrombus is not clearly visualized and it is indirectly detected because of the alteration of blood flow.

Other techniques are occasionally used for the diagnosis of DVT, including impedance plethysmography, computed tomography (CT) and magnetic resonance imaging (MRI) (30).

Therefore, the actual algorithm for DVT diagnosis starts with the Wells score using the risk stratification: low, intermediate and high risk. In patients with low risk and negative D-dimer, no further analysis would be necessary and DVT is ruled out. For the rest of the patients figure 1.3 shows the currently used diagnostic algorithm (28), where the “gold standard”, contrast venography, is used to confirm the diagnosis of DVT in cases when ultrasonography and the pre-test probability are not in agreement.

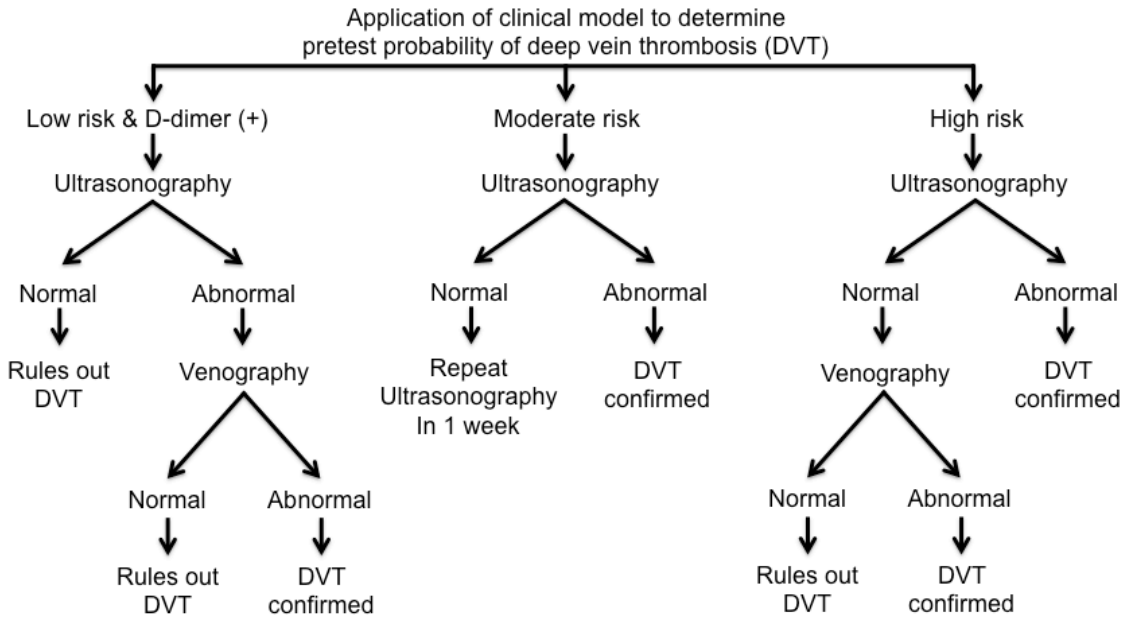

Figure 1.3- Diagnostic approach in outpatients with suspected DVT (28)

1.3 Treatment of DVT

Once DVT is diagnosed, the goals of treatment are to relief symptoms and to prevent embolization and recurrence. Current treatment of DVT commonly begins with anticoagulation with heparin followed by oral anticoagulation (9,37). Although this prevents propagation it has little effect on thrombus resolution. Recanalization of the occluded vessel is often incomplete, leaving vein segments partially or completely occluded; therefore patients remain at increased risk of pulmonary embolism, recurrence of DVT, and post-thrombotic syndrome (38).

Systemic thrombolysis has been investigated to achieve early thrombus resolution, but it was associated with unacceptably high rates of serious bleeding complications, such as retroperitoneal hematoma and intracranial haemorrhage, while rates of thrombus clearance were only relatively modest (21). Catheter directed thrombolysis (CDT) allows a more localized delivery of thrombolytic agents. This may be therefore more effective in achieving local resolution and restoring venous patency while significantly reducing the risks of bleeding complications (13).

A recent Cochrane review (19) compared thrombolysis with standard anticoagulation across 12 randomized controlled trials (RCTs) comprising of 700 patients. The majority of these studies included only patients treated with systemic thrombolysis. Clot lysis was seen more frequently in

the thrombolysis group (relative risk, 4.14; CI95%, 1.22 to 14.01). The incidence of PTS was reduced significantly (relative risk, 0.66; CI95%, 0.47 to 0.94), and a 50% reduction of relative risk for the formation of lower limb ulcers was demonstrated with an average follow-up of 12 months. Bleeding complications were significantly higher in the thrombolysis group (relative risk, 1.73; CI95%, 1.04 to 2.88). The suggestion of this review was that thrombolysis offered potential advantages but that indications were not clearly defined. In addition, according to 2 RCTs comparing CDT with mechanical thrombectomy (39,40), catheter-delivered therapy was found to be useful in restoring blood flow and resulting in venous patency in the short and long term. In addition, significant improvements in quality of life have also been demonstrated. However, defining which group of patients will benefit most from the use of this newer technology is one of the major challenges in optimal DVT treatment (40,41).

The success of venous recanalization, preservation of valve function, and symptom relief may depend on the timing of therapy post thrombosis. These factors influence effectiveness of intervention and the subsequent incidence of PTS. Freshly formed thrombi respond better to thrombolysis than established, organized ones. The time limit after which lysis is ineffective remains unknown, and ten (23), fourteen (20) and twenty one days (40,42) from the onset of symptoms have been proposed. This interval requires further definition as a result of these inconclusive trials to determine the optimal time frame for intervention to prevent valvular destruction and venous hypertension, which may increase the likelihood of longer-term sequels.

The current criteria for the selection of patients for thrombolysis therapy are listed in table 1.2 while the contraindications are summarized in table 1.3 (13,23). As most studies conclude, the inclusion criteria are mainly based on physical examination and patient history, however there are currently no objective biological biomarkers that would allow assess the stage of thrombus organization at the moment of diagnosis and to predict successful thrombolysis.

A recent prospective study has evaluated the proportion of DVT patients that match the current thrombolysis criteria and are eligible for thrombolysis treatment (24). The results of this study showed that only 12 out of 576 patients with DVT (2.1%) admitted to the vascular surgery department were eligible for thrombolysis using the classical criteria. This prospective study demonstrates that the number of patients who are eligible for thrombolysis is very low and that current guidelines may exclude patients that may benefit from thrombolysis.

Extensive thrombosis with high risk of pulmonary embolism
Proximal DVT (ilio-femoral or femoral vein)
Threatened limb viability
Underlying predisposing anatomic anomaly
Good physiological reserve (18-75 years old)
Life expectancy over 6 months
Recent onset of symptoms (<14 days)
Absence of contraindications to thrombolysis

Table 1.2- Indications for DVT Thrombolysis (13,23)

Bleeding diathesis/thrombocytopenia
Organ specific bleeding risk (e.g. recent myocardial infarction, cerebrovascular accident, gastrointestinal bleed, surgery, or trauma)
Renal or hepatic failure
Malignancy (i.e. brain metastases)
Pregnancy

Table 1.3- Contraindications for Thrombolysis (13,23)

1.4 Biological aspects of venous thrombosis

Venous thrombosis organizes and resolves by a process that is similar to the formation of granulation tissue in healing wounds (43,44).

A thrombus initially consists of layers of platelets, leukocytes and fibrin ('lines of Zahn') that encompass the main red cell mass and subsequently resolves through a process of tissue remodelling (44), thought to be regulated by inflammatory cell infiltration (45).

Unlike in arterial thrombi (white thrombi), in venous thrombosis (red thrombi), red blood cells (RBCs) play an important role in the pathophysiology of thrombosis. The cytoplasm of RBCs is rich in iron, which when released into the circulation from a lysed RBC is highly inflammatory because of its oxidative effects on the endothelium (46). The first cell type in a thrombus is the neutrophil (PMN). PMN may cause vein wall injury because of release of inflammatory mediators and its role is fundamental in thrombus organization by promoting both fibrinolysis and collagenolysis (47,48). PMN accumulation in the subendothelial layer and subsequent exposure of collagen causes platelet aggregation and further PMN sequestration, establishing a nucleus for thrombus formation. Reactive oxygen species (ROS), released from the vessel wall

and leukocytes, oxidize haemoglobin (Hgb(Fe^{+2})) to methemoglobin (Hgb(Fe^{+3})). As trapped RBCs lyse, Fe^{+3} contained in methemoglobin is released and induces further RBC lysis. This leads to a positive feedback loop with increased areas of endothelial dysfunction, resulting in thrombus propagation (48).

Monocyte influx into the thrombus peaks at day 8 after thrombogenesis. Monocytes are probably the most important cells responsible for thrombus resolution as well as for recovery and recycling of the toxic free iron released from dead RBCs (49-51). Monocytes play a major role in thrombus neovascularization and fibrinolysis, which can lead to partial or full restoration of vein blood flow; and finally monocytes are associated with fibrosis of the remaining granulation tissue (45,50).

The recruitment of inflammatory cells (52,53) and the proportion of thrombus formed by red cells, fibrin and collagen are important markers of the stage of thrombus organisation (49,54). Figure 1.4 shows histological images and a schematic of thrombus composition at different stages of evolution and organisation. The formation, growth and degradation of the fibrin matrix, the recruitment of macrophages, and the replacement of the fibrin network by collagen rich scar-like tissue in the latest stages, are key events in thrombus organisation and resolution (45).

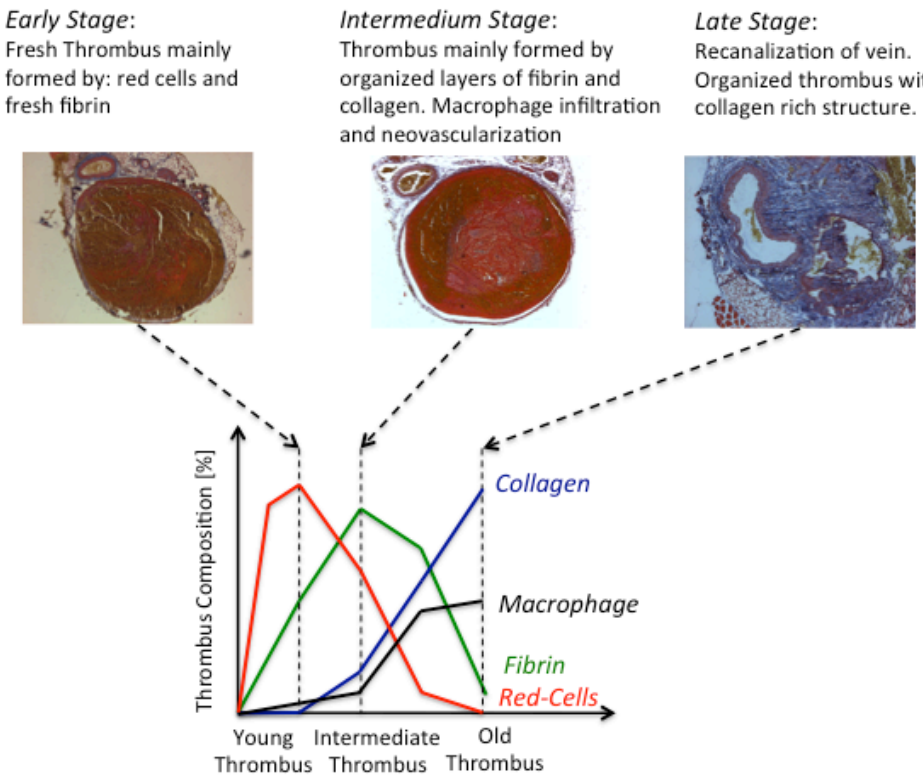

Figure 1.4- Schematic evolution of thrombus organization

1.5 Murine model of DVT

1.5.1 DVT mouse model

In order to study the dynamics of thrombus organisation and correlate those changes with the MRI signal at different time points, we decided to use an in vivo animal model of venous thrombosis.

A number of models of thrombosis ranging from rodents to primates, have been developed to study venous thrombosis (44). Although thrombus resolves within weeks in murine models (months in man), mice are frequently used in pre-clinical studies because they are relatively easy to breed and keep; the histological structure of thrombus is similar to those found in man; they offer the possibility of manipulating their genome to aid study of disease; and there are a sufficient number of antibodies available for immunohistochemistry to help interrogating biology in these models.

The St Thomas' mouse model of venous thrombosis is highly reproducible (>95%), has low mortality (<1%), and produces thrombi with a similar structure and that resolve in a similar manner to those found in man (55). All studies were carried out under the Animals Scientific Procedures Act, 1986.

Thrombus was induced in the inferior vena cava (IVC) of age-matched adult male BALB/C mice (22–30 g) using a combination of reduced blood flow with endothelial disturbance. Briefly, mice were anaesthetised with isoflurane prior to surgery (5% induction, 3% maintenance, Abbott, UK). A midline laparotomy was carried out and the IVC and aorta isolated by retracting the bowels to the left, (kept moist in sterile gauze). A gap between the IVC and adjoining aorta was created just below the left renal vein using blunt dissection with fine forceps and a dissecting microscope at ×10 magnification (Leica, UK) in order to avoid damage to the lumbar veins. A silk ligature of 4/0 length (Ethicon, UK) was passed under the IVC just below the left renal vein, and a piece of 5-0 polypropylene suture (Ethicon, UK) laid on top of the IVC (Figure 1.5). The silk suture was tightened and tied around the IVC and overlaying 5-0 polypropylene. Endothelial damage was induced through application of a neurosurgical vascular clip (Braun Medical, UK) onto the mobilised section of the IVC for 45 seconds, followed by a rest period of 30 seconds, repeated 3 times. The polypropylene suture was removed leaving an ~90% stenosis in the IVC that restricted but did not occlude blood flow. Mice were rehydrated by administration of normal

saline (0.5ml/25g body weight) into the peritoneum, immediately prior to closure using 4/0 polydiaxonone (Ethicon, UK). The skin was closed separately using 4/0 polydiaxonone (Ethicon, UK). Buprenorphine (2µl/g) was administered subcutaneously for post-operative analgesia. Following operation, mice had free access to water and chow (SDS, Essex, UK) and subjected to cycles of 12 hours of daylight followed by 12 hours of darkness.

Surgeries were carried out in collaboration with Dr. Prakash Saha from the Academic Department of Surgery at King's College London.

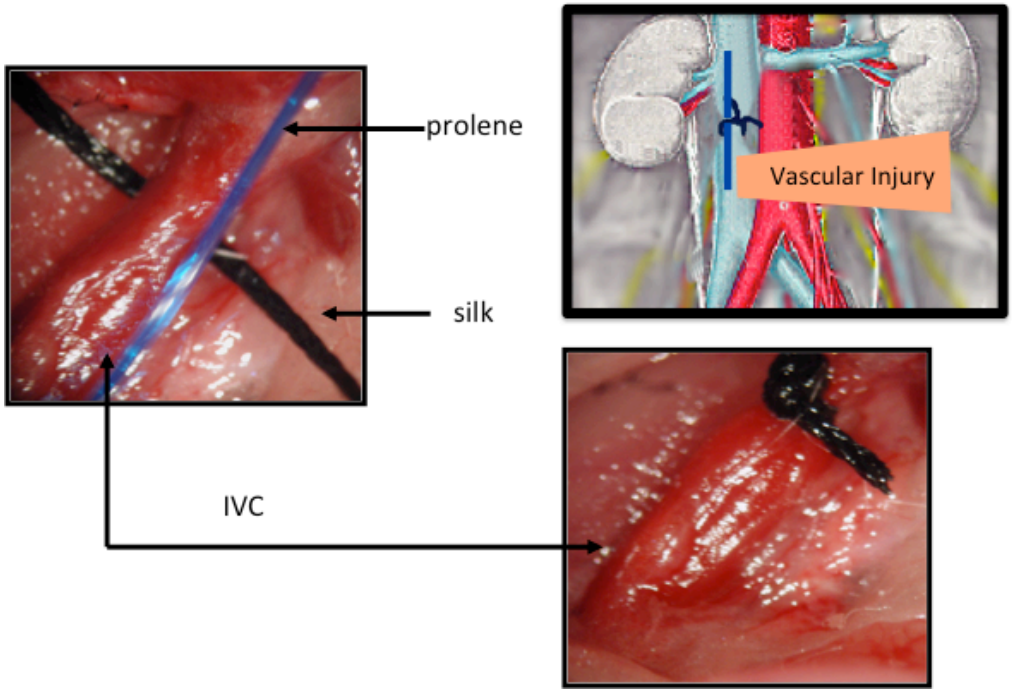

Figure 1.5- Venous thrombosis procedure in the inferior cava vein (IVC) of BALB/C mice. Thrombus formation procedure involved flow disruption and mechanical endothelial damage.

1.5.2 Histology and ICP analysis of venous thrombi

In order to correlate the MR imaging findings with the organisation stage of venous thrombus, all thrombi where analysed in order to estimate their main cell and macromolecule composition: red blood cells, macrophages, fibrin, collagen and iron. Gadolinium concentration was also measured to estimate the local concentration of the fibrin binding Gd-based contrast agent used in this study. Classical histology and immunohistochemistry was performed for fibrin and macrophage visualisation and quantification. Inductively coupled mass spectroscopy (ICP-MS) was used for visualisation and quantification of gadolinium and iron concentration using the different protocols.

1.6 Preclinical MRI using a Clinical 3T scan

All Magnetic Resonance Imaging studies were performed using a clinical 3 Tesla Philips Achieva Gyroscan MR scanner (Philips Healthcare, Best, The Netherlands). The rationale for use of a clinical scanner instead of a pre-clinical high field system was to facilitate translation of the results into clinical practice. Additionally, gadolinium based contrast agent have lower r1 relaxivities at higher field strengths potentially lowering the MR signal and making clinical interpretation of the imaging findings more difficult. In order to maximize the MR signal without compromising the field of view and penetration depth, all the images were acquired using a dedicated 47 mm small animal surface coil (Figure 1.6).

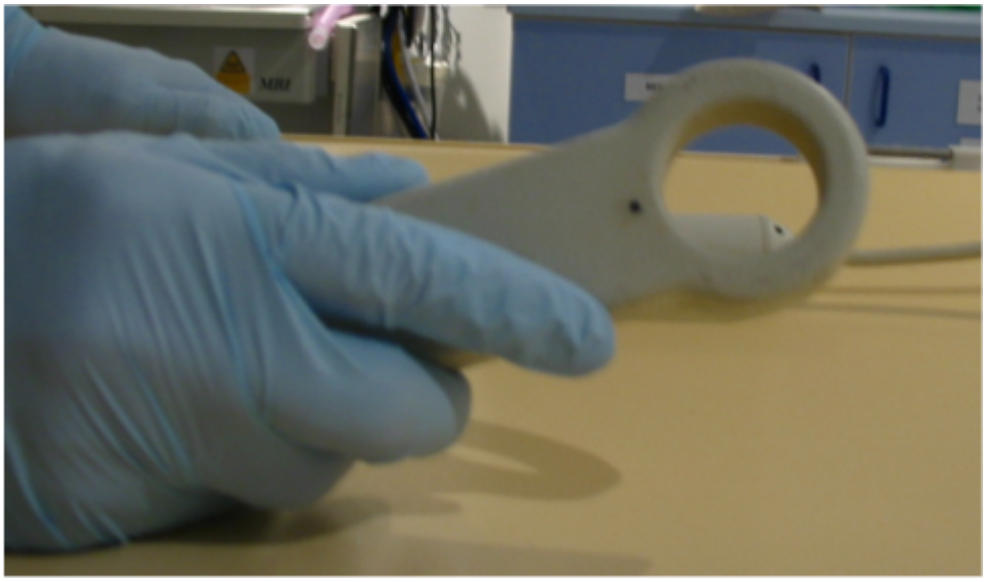

Figure 1.6- Single loop, 47 mm, small animal surface coil

Mice were anesthetized with 1.5-2% isofluorane and 100% oxygen delivered through a nose cone and scanned in prone position. Mice were monitored using a small animal physiological monitoring system (SA Instruments Inc., Stony Brook, NY) and a MRI compatible video camera system (Philips Healthcare, Best, The Netherlands) (Figure 1.7).

Figure 1.7- Set-up of 3T scanner for pre-clinical applications

The basic MRI protocol included:

- Scout Image: To quickly identify the mouse anatomy an initial survey scan was acquired. Scout imaging was performed by acquiring low-resolution, multi-planar images with a multi-slice, segmented, fast gradient echo (GRE) pulse sequence. The field of view (FOV) of the scout images was chosen to encompass the full dimensions of the mouse body. Standard survey pulse sequences are readily available on all clinical MR scanners and only require minor modifications for murine scanning (Figure 1.8).
- Angiography: a Time-of-Flight (TOF) sequence was used to identify the inferior cava vein (IVC) and the abdominal aorta. The renal vein and union of the two common iliac veins were used as a main reference for all subsequent scans. The imaging parameters included: TE/TR=6.9/30.8, flip angle=60°, a 20x33 mm^2 FOV, multi-slice acquisition with 80 slices, a slice thickness of 0.5 mm, gradient-echo spoiled acquisition, and a 112x110 acquired image matrix resulting in a 0.3x0.3x0.5 mm^3 acquired voxel size and a 0.13x0.13 x0.5 mm^3 reconstructed voxel size (Figure 1.9).
- Flow sequence: The average velocity of blood was measured across the thrombus in order to confirm the presence of a thrombus and to measure the changes in

recanalization over time. A phase contrast sequence was used with the following imaging parameters: spatial resolution=100x100 μm, slice thickness=2 mm, TR/TE= 17.5/7.2 ms, flip angle=30°, number of averages=6 and VENC=50 cm/s (Figure 1.10).

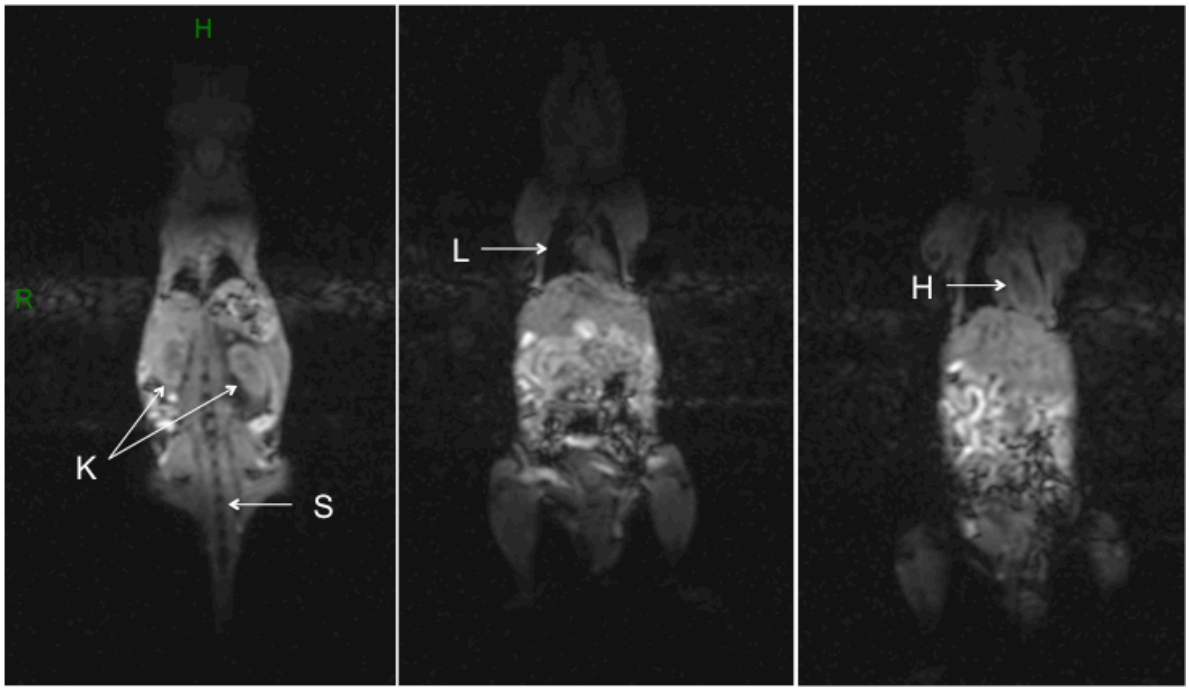

Figure 1.8- Coronal mouse scout images for planning. K: Kidneys, L: Lungs, H: Heart, S: Spine.

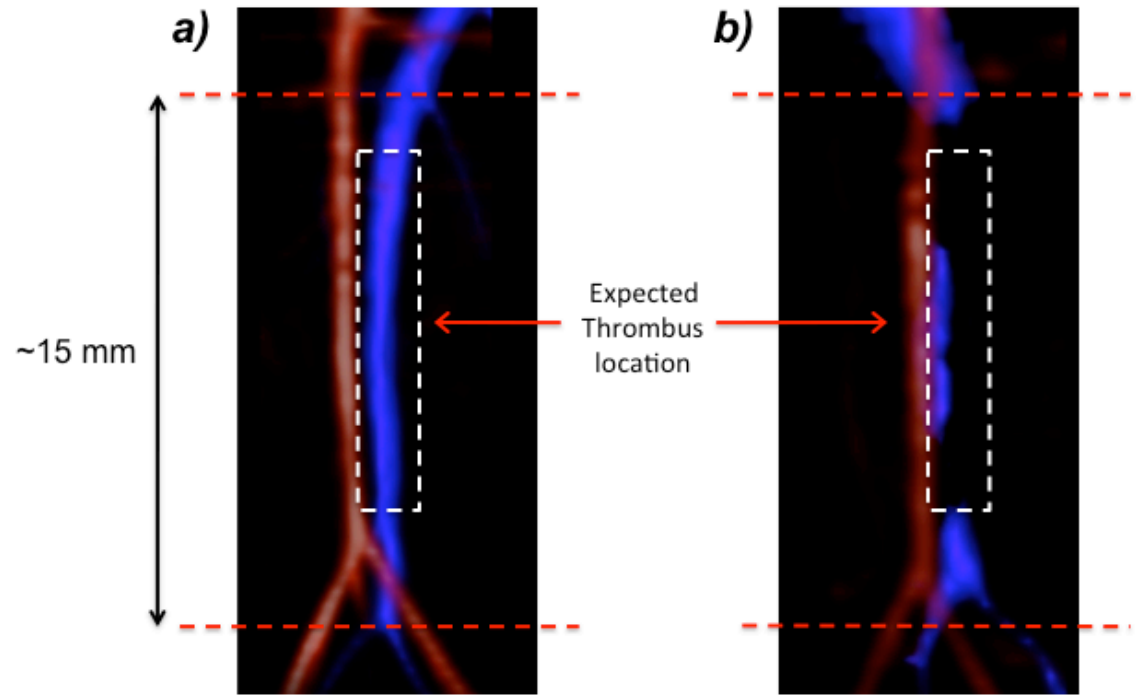

Figure 1.9- Time of Flight reconstruction of inferior cava vein (IVC) (blue) and abdominal aorta (red) in a control (a) and in a mouse with a venous thrombus in the IVC (b). Lines show the area of interest between the renal veins until the union of the two common iliac veins.

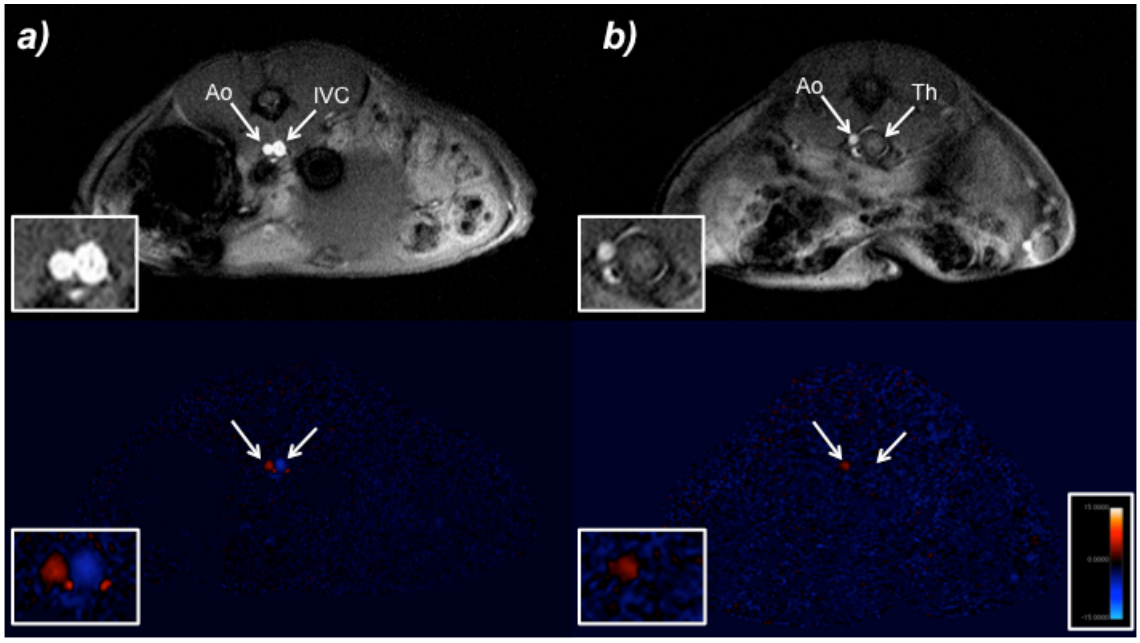

Figure 1.10- Phase contrast MR images in a normal mouse (a) and mouse with a venous thrombus in the IVC (b) showing a flow defect due to the intravascular thrombus. (Ao: Aorta, IVC: Inferior cava vein, Th: Thrombus).

1.7 Hypothesis and aims

We hypothesize that the detection of fibrin deposition, macrophage infiltration and the composition of thrombus, mainly red blood cells (RBC) and collagen content, serve as a surrogate marker of thrombus organisation *in-vivo*.

One of the main advantages of MRI over other diagnostic imaging modalities is its excellent soft tissue contrast and the relatively high spatial resolution of molecular MR images. MR pulse sequences can be designed to emphasize different tissue properties. The most commonly used MR contrasts in clinical routine include: proton density (PD), spin-lattice relaxation time (T1 relaxation time) and spin-spin relaxation time (T2 relaxation time) weighting that facilitate differentiation between normal tissues and pathology. However there are other intrinsic contrasts that are less often used in clinical routine but could help improving the diagnosis of DVT: these include T2* mapping, Magnetization Transfer Contrast (MTC) and Apparent Diffusion Coefficient (ADC).

In this work we propose to analyse the changes in the MRI signal throughout the different stages of thrombus organisation by using T2* mapping as a surrogate marker of the thrombus iron content and indirectly the RBC content, T1 mapping as a surrogate marker of

methemoglobin concentration (a paramagnetic sub-product of the haemoglobin oxidative process). The collagen content in thrombus will be estimated using a Magnetization Transfer Contrast (MTC); and the Apparent Diffusion Coefficient (ADC) images will be used as a surrogate marker of thrombus permeability.

Additionally we sought to study the uptake of two molecular MRI contrasts: one gadolinium-based contrast agent that specifically binds to fibrin, EP-2104R (EPIX Pharmaceuticals, Lexington, MA) (56-58) and a citrate-coated very small iron oxide super-paramagnetic nanoparticle, VSOP (59,60) as marker of macrophage infiltration. We investigated these agents throughout the different stages of thrombus organisation in a murine model of deep venous thrombosis.

We hypothesise that this non-invasive method could provide novel information about the stage of thrombus organisation at the moment of diagnosis and could provide important biological information to better identify thrombus with a higher likelihood of successful lysis after thrombolytic treatment.

In order to develop a complete MRI protocol for the evaluation of a patient with suspected VT we also sought to develop and implement two novel MR angiography techniques, based on either arterial spin labelling (ASL) (61) or T2 blood contrast, to obtain angiograms and venograms without the need of a potentially nephrotoxic MR contrast agent. The proposed ASL sequence is flow-dependant but does not require two acquisitions nor image subtraction (62). In order to take into account the slow venous blood flow, we maximized the labelling delay (time delay between blood labelling and image acquisition). The labelling delay was fitted in 2 or 3 heartbeats to allow the labelled venous blood to reach the area of interest and, at the same time, providing excellent background suppression (63). The second approach is a flow independent sequence which takes advantage of the differences in T2 relaxation time of arterial and venous blood using a spatially non-selective T2 preparation prepulse (T2prep) (64). The technique is based on the acquisition and subtraction of two 3D steady-state free precession (SSFP) data sets; one obtained with and one without a spatially non-selective T2prep (65). This allows for nulling of signal of arterial blood and surrounding tissue while maintaining the signal of venous blood in the subtracted image.

In conclusion I propose a new MRI protocol for the evaluation of patients with suspected VT that provides in-vivo information on the stage of thrombus organization in order to better guide medical treatment decisions.

Hypothesis

The non-invasive estimation of the fibrin and macrophage content in venous thrombosis by MRI can improve the diagnosis of VT and provide accurate information on the stage of thrombus organization *in-vivo*.

Aims

1. To investigate the relationship between T2* and T1 mapping, MTC and ADC MR sequences and venous thrombus composition *in vivo*.
2. To investigate the merits of both a macrophage and fibrin-specific MR contrast agent to estimate the fibrin and macrophage content in venous thrombus *in-vivo* and to correlate MR findings to histological analysis.
3. To investigate the best combination of MRI sequences which allow identification of venous thrombus amenable for thrombolysis.
4. To develop a novel non-contrast MR angiography technique that avoids the risks of MR contrast agents and can be used to diagnose patients with suspected VT or other vascular diseases.

Chapter 2 Venous thrombus characterization using MRI without the use of contrast agents

2.1 Aims and objectives

Patients with the highest risk of developing DVT include those after major surgery, undergoing oncological treatment, elderly, and pregnant women. In most of these patients the use of intravenous contrast agents is not recommended because of the high risk of renal failure or the high probability that the contrast agent can cross the placenta (33-35). These adverse events are therefore an important incentive to develop a new imaging methodology to visualize and characterise venous thrombi without the need of a contrast agent.

One of the main advantages of Magnetic Resonance Imaging (MRI) over other diagnostic imaging modalities is the excellent soft tissue contrast. MR pulse sequences can be designed to emphasize different tissue properties. The most common contrasts used in clinical scans include proton density (PD), spin-lattice relaxation time (T1) and spin-spin relaxation time (T2) to differentiate between normal and pathological tissues. However there are other intrinsic contrasts that are less often used in clinical scans but could improve the diagnosis of DVT. These contrasts include the T2* relaxation time, Magnetization Transfer Contrast (MTC) and Apparent Diffusion Coefficient (ADC) among others.

As it was discussed in the Chapter 1, thrombus organization follows well-known steps starting from its formation until its organisation through continuous dynamic changes in its composition where red blood cells, fibrin, and collagen constitute the principal components (Figure 1.4).

Early thrombus consists of layers of platelets, leukocytes and fibrin (‘lines of Zahn’) that encompass the main red cell mass, which accounts for almost 85% of the thrombus volume in the earliest stage (66). The cytoplasm of RBCs is rich in iron. During thrombus organization, red cells are lysed and iron is subsequently released. The released iron is highly inflammatory because of its oxidative effects on the endothelium (46). Reactive oxygen species (ROS) released from the vessel wall and leukocytes, oxidize haemoglobin ($Hgb(Fe^{+2})$) to methemoglobin ($Hgb(Fe^{+3})$) (67). Free methemoglobin ($Hgb(Fe^{+3})$) induces further RBC lysis that lead to an inflammatory cascade resulting in thrombus propagation (48).

One of the main purposes of thrombus formation is to isolate the toxic iron released from RBCs (68) and the cross-linked fibrin matrix plays a major role in accomplishing this task during this early inflammatory response. This early inflammatory response also provides a time window for removal of iron by leukocytes, in particular mononuclear phagocytes that accumulate within the thrombus during its resolution (43,48,52). In later thrombus resolution stages, the fibrin matrix is replaced by granulation tissue, which in the latest stage is replaced by a collagen matrix, with no to little fibrin and red blood cells (48,53).

We hypothesize that non-contrast enhanced MRI would allow characterization of the dynamic transformation of thrombus and thus to biologically characterize thrombus at the moment of diagnosis.

The non-invasive estimation of the total iron content in thrombus could be used as a surrogate marker of the red blood cell content in the thrombus, and thus could provide a good indication of the stage of thrombus organisation. This thus may allow differentiation between a RBC rich early thrombus and an old RBC devoid thrombus.

The gradient echo sequence is particularly sensitive to magnetic field inhomogeneities generated by e.g. iron, and has been successfully used in many clinical applications to obtain T2* maps to estimate the iron content of a specific tissue (69-72). Here we propose to use the T2* mapping protocol to estimate the iron content in venous thrombus and to correlate imaging findings with histological analysis and inductively coupled mass spectroscopy (ICP-MS) total iron measurements.

The heme iron undergoes changes in its molecular structure during thrombus evolution. It has been speculated that the formation of methemoglobin ($Hgb(Fe^{+3})$) is responsible for the hyper-intense signal observed in T1-weighted images acquired during the evolution of intracranial haemorrhage (73) and venous thrombosis (74).

The heme iron in oxyhemoglobin ($Hgb(Fe^{+2})$) is diamagnetic, with no unpaired electrons and is thus not detectable with MRI. When the haemoglobin is removed from the high oxygen environment, the heme iron undergoes oxidative denaturation to a ferric state (Fe^{+3}), forming Methemoglobin ($Hgb(Fe^{+3})$). Methemoglobin has five unpaired electrons and the ultrastructure of heme allows binding to water molecules that result in a shortening T1 time effect (67,73).

Finally most of the iron is taken up by macrophages and stored as hemosiderin, which does not show any significant T1-shortening effect as it its water-insoluble (68,75).

In this work we analysed the thrombus T1 relaxation time during thrombus organization and correlated the imaging findings with the total iron and methemoglobin ($Hgb(Fe^{+3})$) concentration by ICP-MS and with histological analysis at different stages of thrombus organization. For this purpose we used a T1 mapping sequence for accurate estimation of the T1 relaxation time of the thrombus at different time points of thrombus organization (76).

Magnetization Transfer Contrast (MTC) takes advantage of the different macromolecular composition of tissues in order to create contrast (77-79). MTC is based on a saturation exchange between the bound protons of macromolecules and free water protons when the two pools are coupled by dipolar interactions and/or through chemical exchange (80,81). The two most important macromolecules of thrombus are fibrin and collagen, which have different sensitivities for magnetization transfer pulses that result in different MR contrast (81). In this work we optimized the MTC sequence in order to estimate the collagen content of venous thrombi *in-vivo*, and to differentiate between young and old thrombus.

2.2 Materials and Methods

2.2.1 DVT mouse model

Venous thrombosis was induced in the inferior vena cava (IVC) of 8-10 weeks old male BALB/C mice as described in section 1.5.1. MRI was performed at day 2, 4, 7, 10, 14, 21 and 28 following thrombus induction. Fourteen mice were scanned at each time point. 6 mice at each time point were used for histological analysis, and the remaining 8 mice where either used for ICP-MS measurement of the total thrombus iron content (4 mice) or measurement of Fe^{+3} concentration (4 mice) (figure 2.1).

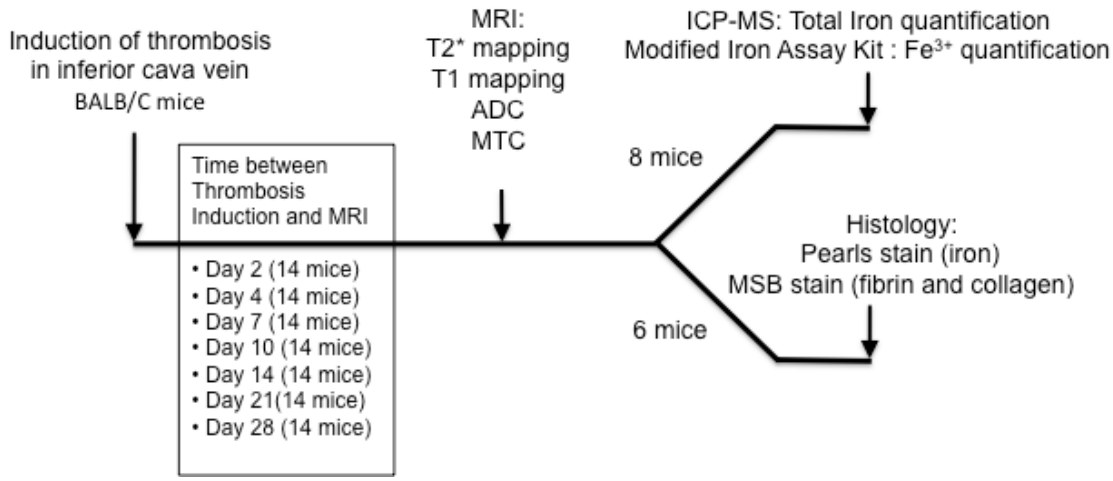

Figure 2.1- Study design. Fourteen mice were scanned at each time point (day 2, 4, 7, 10, 14, 21 and 28) after IVC thrombosis induction. At each time point, 6 mice were used to correlate MRI findings with histology. Another 8 mice were used to measure the total iron (4 mice) and Fe^{3+} concentration (4 mice).

2.2.2 Histology and ICP analysis

All thrombi were harvested immediately after the MR imaging session. Abdominal laparotomy was performed to allow visualization of the whole abdominal IVC and to measure the distance from the renal branches until the union of the two common iliac veins. The IVC was harvested en-bloc, including the thrombus and the IVC extending from the renal branches down to the union of the two iliac veins. The harvested IVC was then pinned onto cork mats and stretched to the same length as measured *in-situ* prior to harvest.

For histology analysis, thrombi were stored in 10% formalin for 24 hours before being embedded in wax. Paraffin sections (5 μm) of the entire IVC were taken at 500 μm intervals to allow comparison with the corresponding MRI slices. Sections were stained with haematoxylin and eosin (H&E) for anatomical detail; with Martius Scarlet Blue (MSB) trichrome stain for RBC, fibrin and collage visualization and quantification (82); with Immunohistochemistry for fibrin and macrophages; and with Perls' Prussian Blue for iron deposition visualization.

Inductively coupled mass spectroscopy (ICP-MS) (PE 200 LC system linked to PerkinElmer Sciex Elan 6100 DRC, PerkinElmer, Boston, US) was performed on a subset of thrombus samples for total iron concentration quantification. Thrombus was digested in 70% nitric acid at 37°C overnight followed by dilution with deionized water for ICP-MS analysis. A standard curve was run with each sample set for Fe concentration determination.

A commercially available method was modified to obtain quantification of Fe^{3+} content within the thrombus. The Quantichrom Iron Assay Kit (BioAssay Systems, CA, US) uses a chromogen that specifically forms a blue coloured complex with Fe^{2+}. Other reagents in this kit reduce any Fe^{3+} within a sample to Fe^{2+}, allowing the assessment of total iron concentration. By subtracting Fe^{2+} content of the thrombus from the total iron content, it was possible to calculate the amount of Fe^{3+} within processed thrombi (83).

2.2.3 Image Analysis

Digital images of stained histology sections were captured using a light microscope (Leitz, Leica, UK) and a microscope-mounted camera (EXi Blue, QImaging). The images were analysed using the image analysis software ImageJ (National Institutes of Health, Bethesda, MD, USA) and the colour-threshold tool was used to estimate the percentage of fibrin, collagen, iron, macrophages and red blood cell content in the intravascular region of the IVC in each stained histological slice.

2.2.4 MRI Protocol

All Magnetic Resonance images were obtained using a clinical 3T Philips Achieva Gyroscan MR scanner (Philips Healthcare, Best, The Netherlands). As was described in section 1.6, mice were anesthetized with 1.5–2.0% isofluorane and 100% oxygen delivered through a nose cone and scanned in prone position using a dedicated 47 mm small animal surface coil. Mice were monitored using a small animal physiological monitoring system and a MRI compatible video camera system. The basic sequences used included: Scout image, abdominal TOF for cava vein and aorta identification and a phase contrast quantitative flow sequence for measurement of IVC flow was used as previously described in section 1.6. Specific sequence parameters of each imaging protocol will be described in the corresponding sections.

2.2.5 Statistical Analysis

Continuous data are expressed as mean ± 1 SD. Data were compared using a one-way ANOVA test or paired t-test as needed. Measures of agreement between MRI and histology findings were calculated using linear regression analysis and Bland-Altman plots. All statistical analysis was done using SPSS Statistics software package release 19.0 (IBM Corporation, Somers, NY, USA). A P-value of <0.05 was considered statistically significant.

2.3 Thrombus volume and IVC flow during venous thrombus organisation

2.3.1 Introduction

In order to detect the presence of venous thrombus *in-vivo* we first performed a Time-of-Flight (TOF) sequence to identify the inferior vena cava (IVC) and the abdominal aorta. The observation of a flow defect in the IVC was used as an indication of the presence of a venous thrombus. Additionally a phase contrast sequence was used to measure blood flow in a cross section of the IVC and to measure the changes in recanalization over time. The parameters used in both sequence are described in Section 1.6.

2.3.2 Results

Filling defects in the IVC were successfully visualized in all mice. During thrombus organisation and resolution the filling defect declined over time as shown in Figure 2.2.

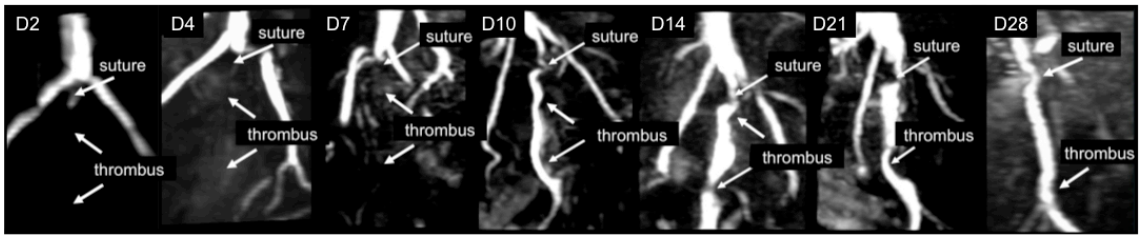

Figure 2.2- TOF images demonstrate the presence of thrombus in the murine inferior vena cava, which recanalises over 21 days.

The volume of the filling defect was estimated using the TOF images and significantly reduced with time ($P<0.001$, One-way ANOVA, Figure 2.3). At day 1 thrombus was larger than at any other day ($P<0.001$, Bonferroni post-hoc test). There was no significant difference between the thrombus volume at day 4 and 7, however after day 7, thrombus was significantly smaller at day 10, 14, 21 and 28 compared to day 4 (Bonferroni post-hoc test).

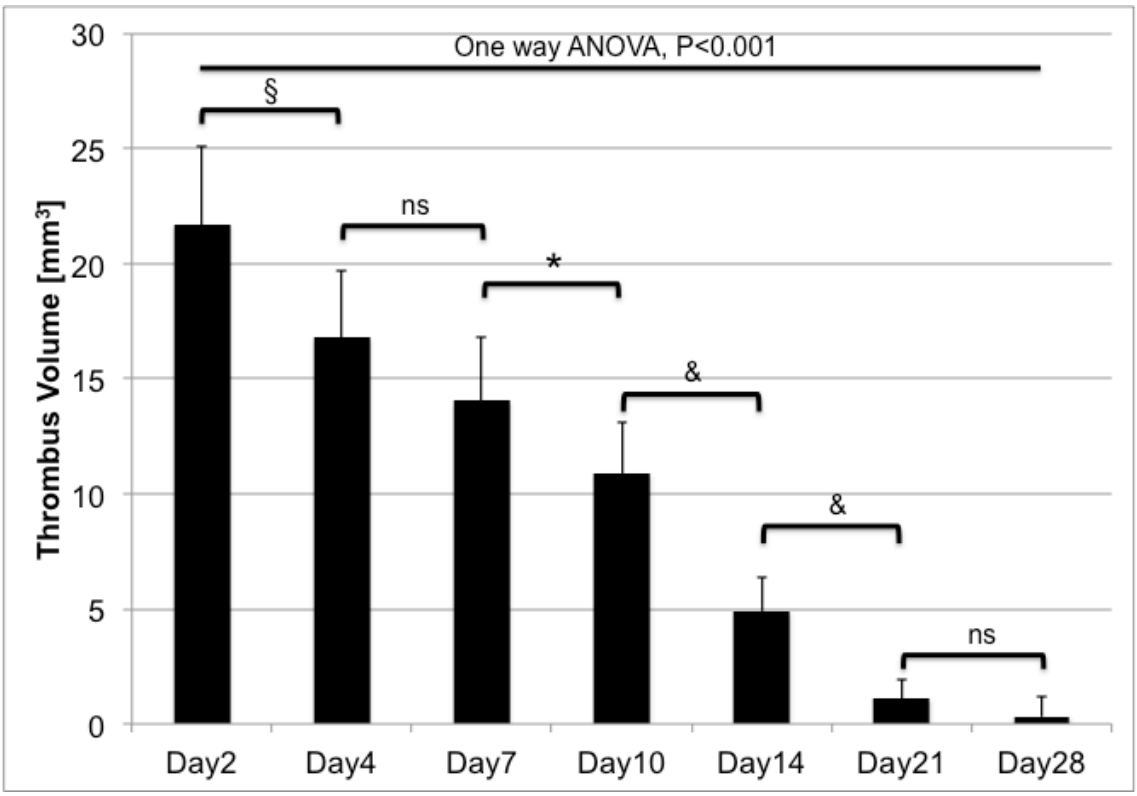

Figure 2.3- Average thrombus volume (mm^3) at different time points during thrombus organisation. One-way ANOVA analysis with Bonferroni post-hoc test (*=P<0.05, &=P<0.01, §=P<0.001, ns: non significant)

In normal mice the average blood flow across the IVC measured using Phase-Contrast MRI was 0.55 ± 0.05 ml/min (Figure 2.4). Between day 1 and 28 after thrombus induction there was an increase in blood flow detected in the IVC (P<0.01, One-way ANOVA). In agreement with variable thrombus size during thrombus organization, there was high variability in IVC blood flow during thrombus organization. No IVC flow was detected in the early stages of thrombus evolution. No significant differences were found in IVC blood flow between Day 2 and Day 7. From day 10 on a significant increase in IVC blood flow was detected (Bonferroni post-hoc test).

Strong and significant correlation was found between the average IVC blood flow and the thrombus volume at different time points during thrombus organisation (Figure 2.5, R^2=0.938, P<0.005).

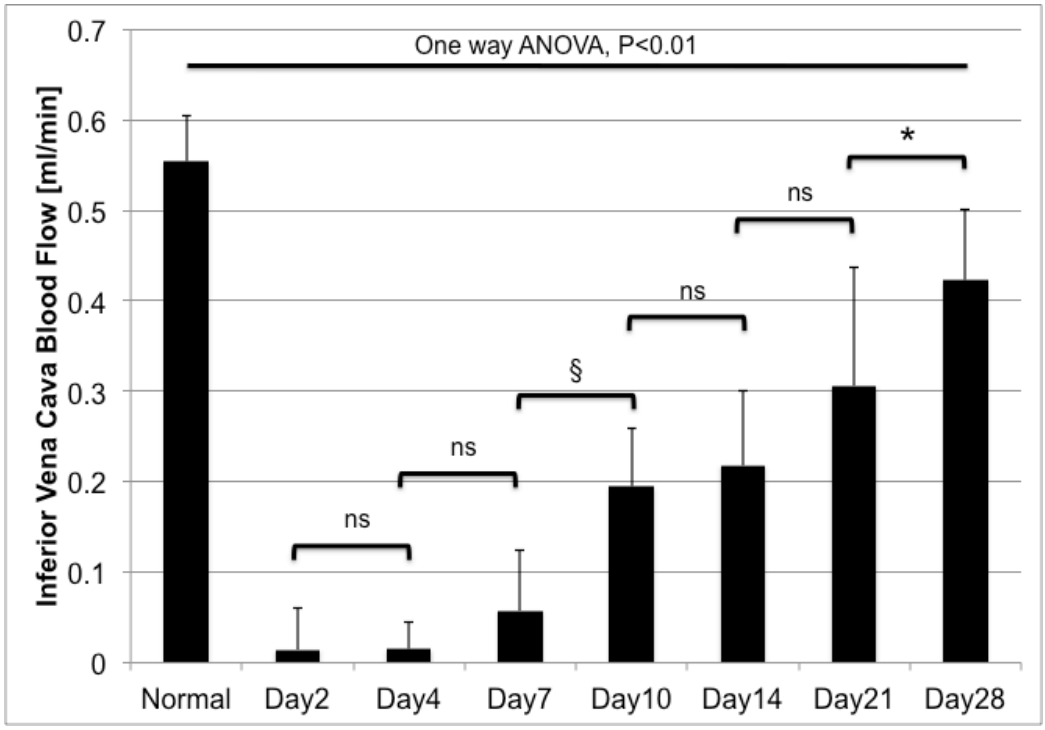

Figure 2.4- IVC blood flow (ml/min) in normal mice and at different time points during thrombus organisation. One-way ANOVA analysis with Bonferroni post-hoc test (*=P<0.05, &=P<0.01, §=P<0.001, ns=non significant)

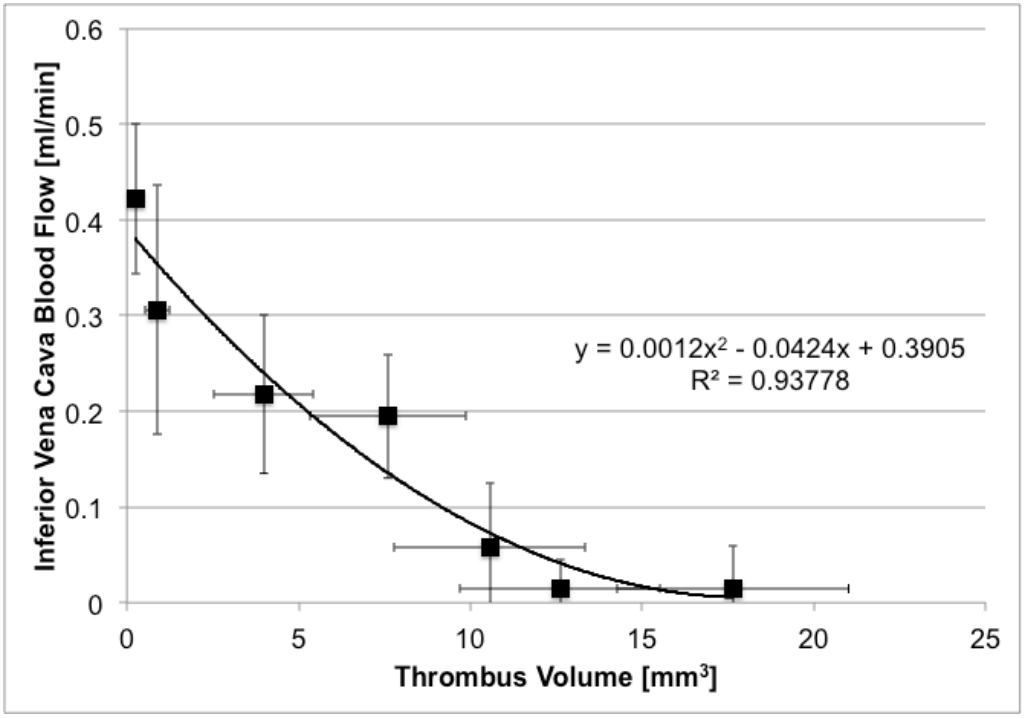

Figure 2.5- Relationship between the average IVC blood flow (ml/min) and average thrombus volume (mm^3) at different time points during thrombus organisation (R^2=0.938, P<0.005)

2.4 T2* mapping

2.4.1 Introduction

The use of MRI for estimation of iron concentration in tissues has been first described in the early 1980s (84). The presence of objects with different susceptibilities induces local magnetic field distortions that are detected in MRI through the inherent negative contrast due to local spin dephasing (71,85). The intracellular iron of trapped RBCs in venous thrombus is a big source of magnetic field inhomogeneities that can be detected using a Gradient Echo acquisition. The magnitude of the transverse magnetization Mxy in the Gradient Echo acquisition decays according to the following equation:

$$M_{xy}(t) = M_{xy}(0) \cdot e^{\frac{-t}{T_2^*}} \qquad \text{Eq. 2.1}$$

Where T_2^* (T_2 star) is related with the T_2 value by the following equation:

$$\frac{1}{T_2^*} = \frac{1}{T_2} + \frac{1}{T_2'} \qquad \text{Eq. 2.2}$$

Where T_2 is the spin-spin relaxation time and T_2' is inversely proportional to the magnetic field inhomogeneity ΔB in each imaging voxel, i.e.:

$$T_2' \propto \frac{1}{\gamma \cdot \Delta B} \qquad \text{Eq. 2.3}$$

Because of the T_2^* dependence, Gradient Echo images are much more prone to signal loss than the spin echo sequence in regions with magnetic field inhomogeneity. However this susceptibility effect can be used to estimate iron concentration in tissues because of the local magnetic field disturbances generate by iron. The reciprocal of T_2^* ($R_2^*=1/T_2^*$) is directly proportional to the iron concentration (71) and has been successfully used in clinical scans to estimate the cardiac and liver iron content in patients with transfusional siderosis (69-72).

Because red cells are the most abundant cells in young thrombus, and the removal of free iron is a critical event during thrombus organization, we hypothesized that the accurate

measurement of the thrombus' T2* value could provide information about the thrombus organization stage *in-vivo*.

2.4.2 Materials and Methods

MRI Protocol

A 3D T2* multi-echo gradient echo sequence was implement on a 3T Philips Achieva Gyroscan MR scanner (Philips Healthcare, Best, The Netherlands) (Figure 2.6). Because of the lack of the refocusing 180° pulse (like in the spin-echo sequence) the decay of the signal is given by the T2* time, as was shown in equation 2.1. T2* multi-echo gradient echo imaging parameters included: acquired spatial resolution 200x200 μm, slice thickness of 500 μm, TR=354 ms, and flip angle=35°. Six images at different echo times were acquired starting at TE=4.6 ms and with an echo spacing of 6.9 ms.

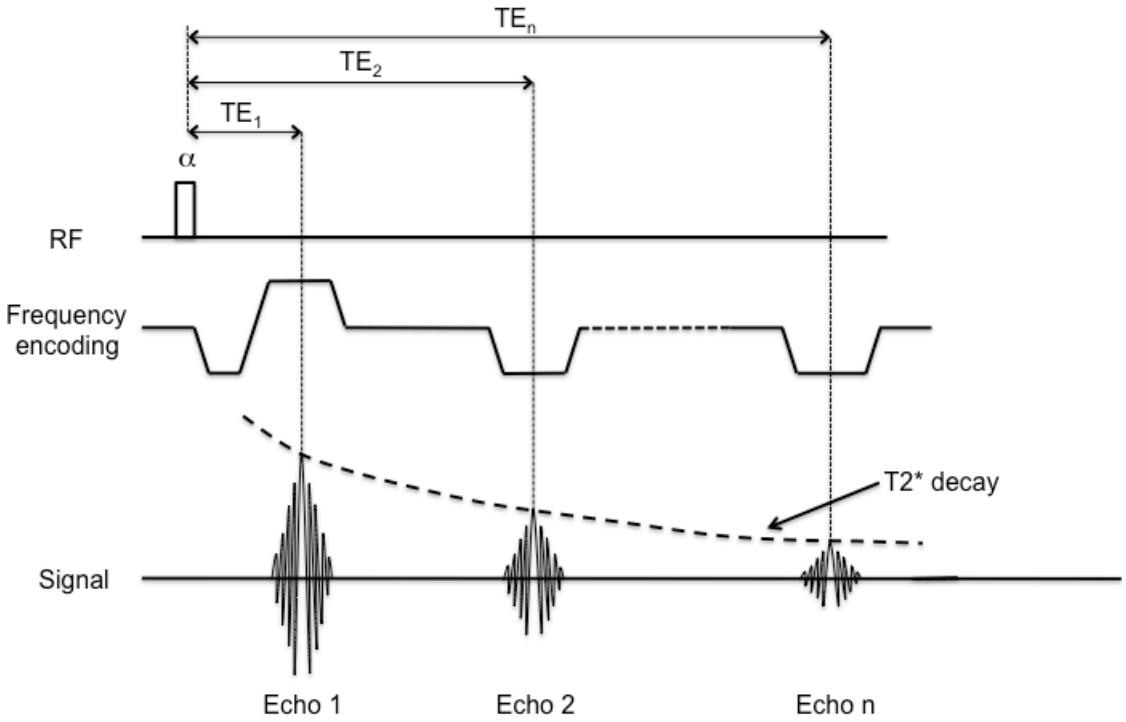

Figure 2.6- T2* multi-echo gradient echo sequence for T2* mapping

T2* maps from 30 slices were obtained using a custom-made software written in Matlab (Mathworks, Natick, MA, USA) which fits pixel-by-pixel the T2* equation decay (Eq. 2.1) and finds the average T2* value in a region of interest. Figure 2.7 shows the user interface of the T2* mapping Matlab tool.

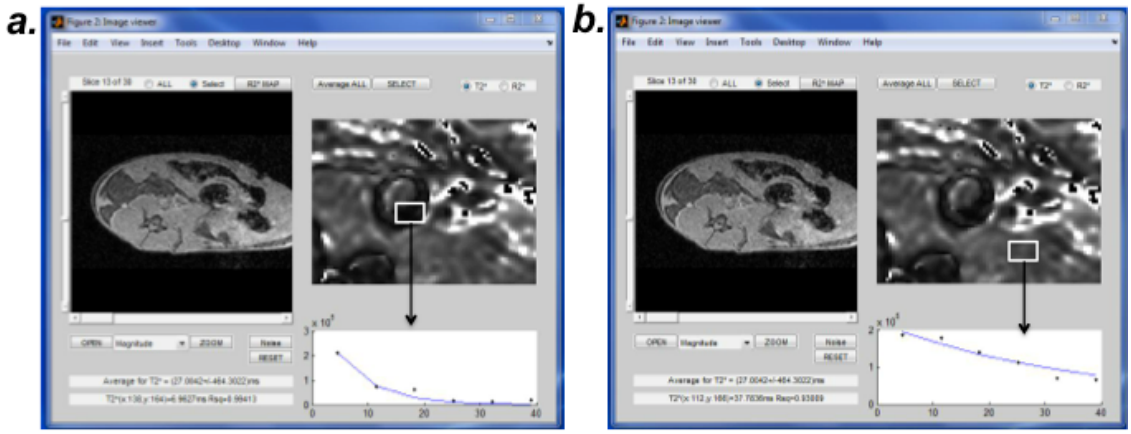

Figure 2.7- Pixel-by-Pixel T2* time quantification using a custom-made software in Matlab. Darker pixels represent shorter T2* values. (a) shows the T2* quantification in a ROI with short T2* (faster decay of the signal); (b) shows the T2* quantification in a ROI with long T2*

Histology and ICP analysis

The total iron content in the thrombus was analysed using ICP-MS as described in section 2.2.2. MSB stain was used to identify red blood cells and Perls' Blue stain was used to identify iron deposition in the thrombus (section 2.2.2). In the MSB slices, red blood cells appear yellow and on the Perls' stain, hemosiderin deposition appears blue.

2.4.3 Results

Fourteen mice at each time point (day 2, 4, 7, 10, 14, 21 and 28) where successfully scanned with the T2* multi-echo gradient echo acquisition and T2* maps were obtained with the Matlab software.

The average thrombus T2* time increased with thrombus organization (Figure 2.8a). Younger thrombus (Day 2 and 4) showed shorter T2* time than older thrombus ($P<0.01$, One-way ANOVA). The reciprocal of the T2* relaxation time, R2* [Hz], shows the inverse trend with a monotonically decreasing R2* value during thrombus organisation (Figure 2.8b).

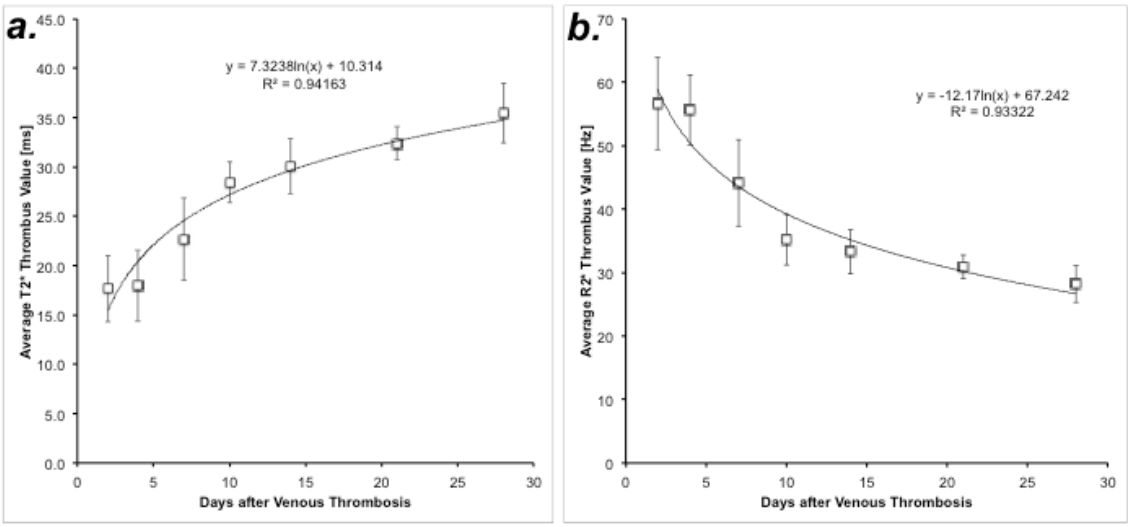

Figure 2.8- Average (a) T2* and (b) R2* times at different time points during venous thrombus organization

The total iron content in the thrombus measured by ICP-MS decreased during thrombus organisation (Figure 2.9a), which is in concordance with the hypothesis that the main purpose of fibrin matrix formation is to isolate the toxic iron released from RBCs and to provide sufficient time for removal of iron by mononuclear phagocytes that accumulate within the thrombus during its resolution (68). The total iron content in thrombus [μg] showed a strong correlation with the average thrombus R2* value [Hz] (R^2=0.852, P<0.01, Figure 2.9b), and a significant correlation between total iron content [μg] and average R2* [Hz] at different time points of thrombus organisation was also found (R^2=0.843, P<0.01, Figure 2.9c).

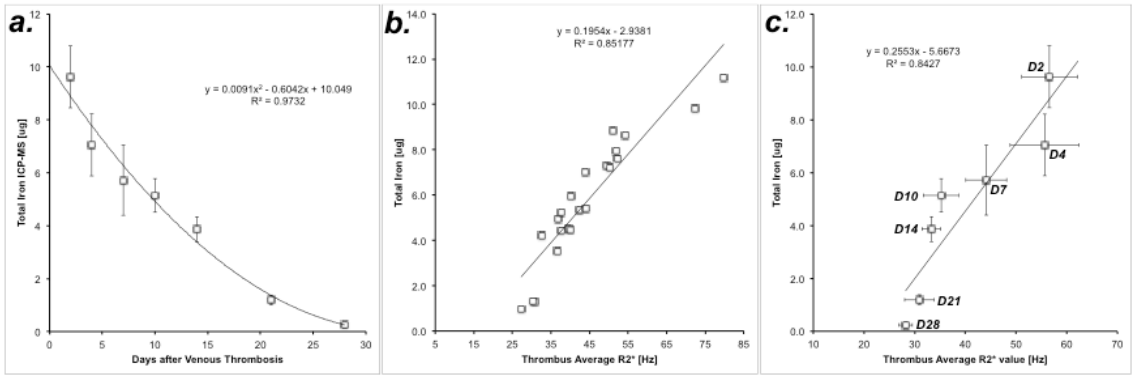

Figure 2.9- (a) Total thrombus iron content [µg] measured by ICP-MS during venous thrombus organization. (b) Relation between thrombus total iron content [µg] and the corresponding thrombus R2* [Hz]. (c) An almost linear relationship between the total iron content [µg] and the average R2* at different time points during thrombus organization was observed.

Figure 2.10 shows a representative Perls' and MSB stained histological slice at different time points of thrombus organisation and the corresponding T2* map. Red blood cells (RBCs) appeared brown-yellow on MSB stained slices. At day 2 after thrombus induction almost 90% of the transversal surface of the thrombus was covered by RBCs. At day 4 it was possible to visualize the fibrin matrix in the thrombus periphery and still a large amount of RBCs. At day 10, thrombus consisted primarily of a tight fibrin matrix with some early signs of collagen deposition (blue stain on MSB) and some residual RBCs. At Day 21 and 28, thrombus was mainly composed of a collagen matrix.

No positive Perls' staining was observed in the earliest stages (day 2, 4 and 7) after thrombus induction. An increase in positive Perls' staining (blue stain) was observed from day 10 until 28, reaching a maximum cross-sectional thrombus area of approximately 40% at day 28 (Figure 2.10).

Figure 2.11 shows the quantification of the percentage of thrombus volume covered by RBCs and iron at different time points of the thrombus organization. At the earlier stages the RBCs are the primary cells within the thrombus while hemosiderin deposition is a late event of thrombus organization and only becomes significant starting at day 14 after thrombus induction.

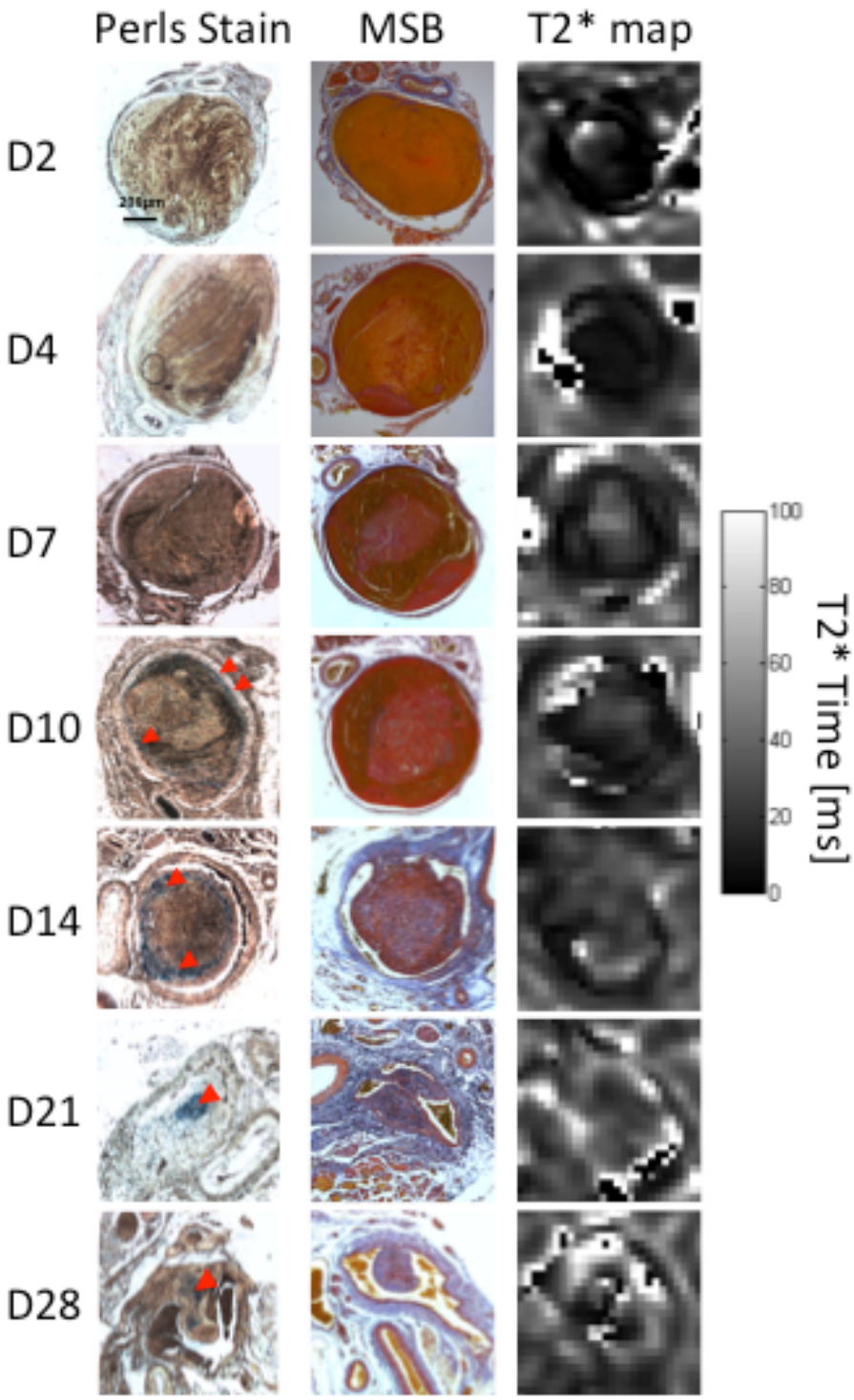

Figure 2.10- Perls' stain for iron deposition (hemosiderin) quantification (blue staining); MSB for Red Blood Cell (RBC) quantification (yellow staining) and T2* mapping of venous thrombus at different time points during thrombus organisation.

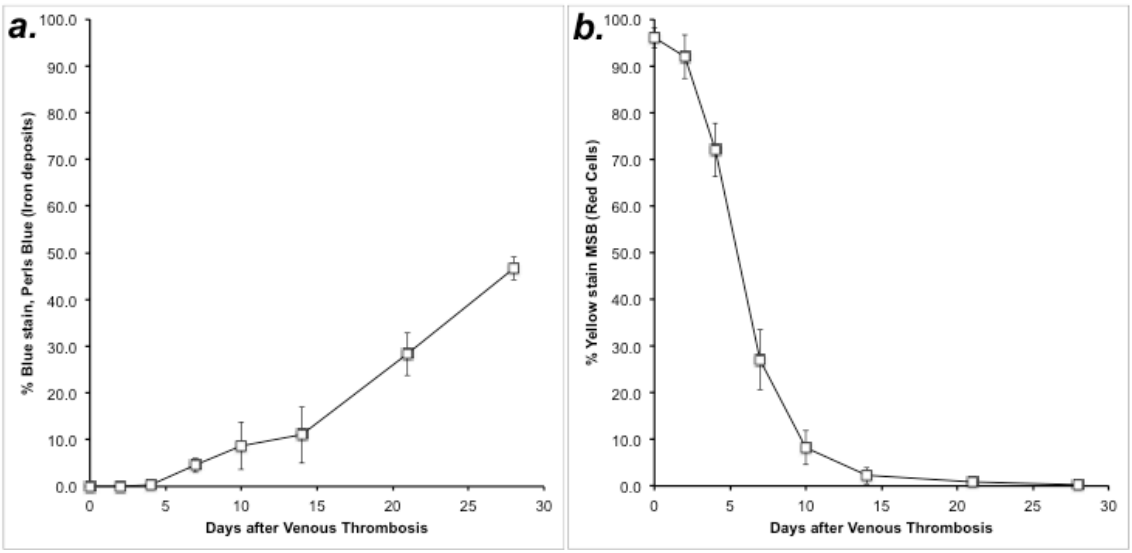

Figure 2.11- % of Perls' (a) and Red Blood Cell (b) stain of venous thrombus at different time points during thrombus organisation

The total thrombus iron content in [µg] was found to be very well correlated with the RBC content of venous thrombus (Figure 2.12a, R^2=0.90, P<0.001), which is in concordance with the hypothesis that the main source of iron in thrombus are fresh RBCs trapped in the young thrombus. In contrast we found an inverse relation between total thrombus iron and the hemosiderin stain (Figure 2.12b). This relation does not have any biological significance, and demonstrates that there is no temporal relationship between the total amount of thrombus iron and the hemosiderin deposition. Hemosiderin deposition is a late event during thrombus organization and occurred in the latest stage when most of the RBCs cells have been cleared from the thrombus.

The highest R2* (lowest T2*) values were observed in the earliest stages of thrombus organisation, when RBCs are the most abundant cells in the thrombus, resulting in a very strong correlation between RBC content and R2* at different time points of thrombus organisation (R^2=0.96, P<0.001, Figure 2.13a). The hemosiderin content has an inverse relation with the R2* values, similar to the previous relation with the total iron [µg] content of the thrombus. This negative relation demonstrates that there is no temporal relationship between the thrombus R2* value and the hemosiderin concentration.

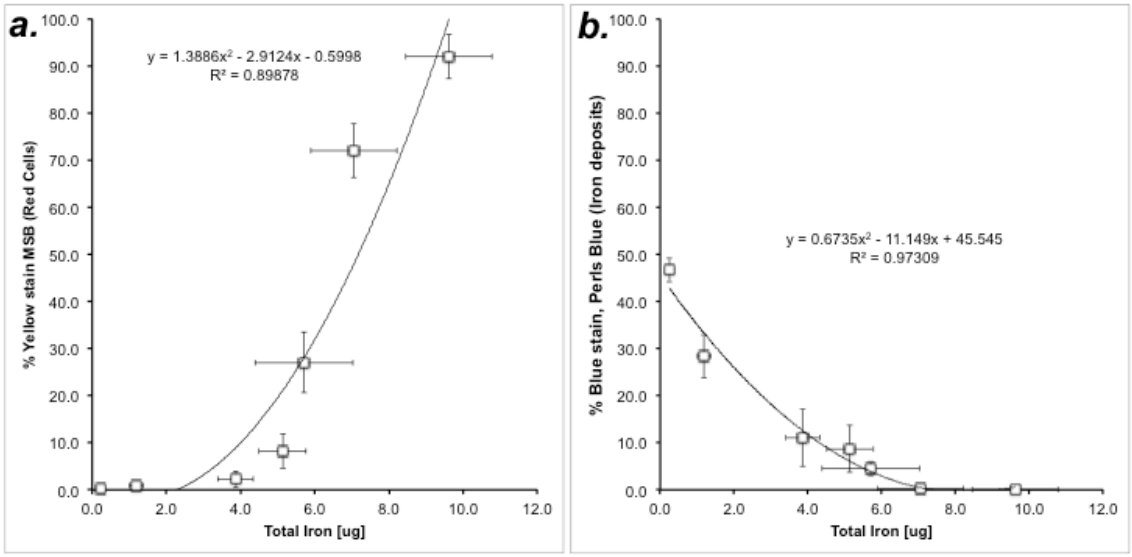

Figure 2.12- Total iron content in [ug] measured by ICP-MS and its relation with the % of Perls' (a) and Red Blood Cell (b) stain of venous thrombus at different time points during thrombus organisation

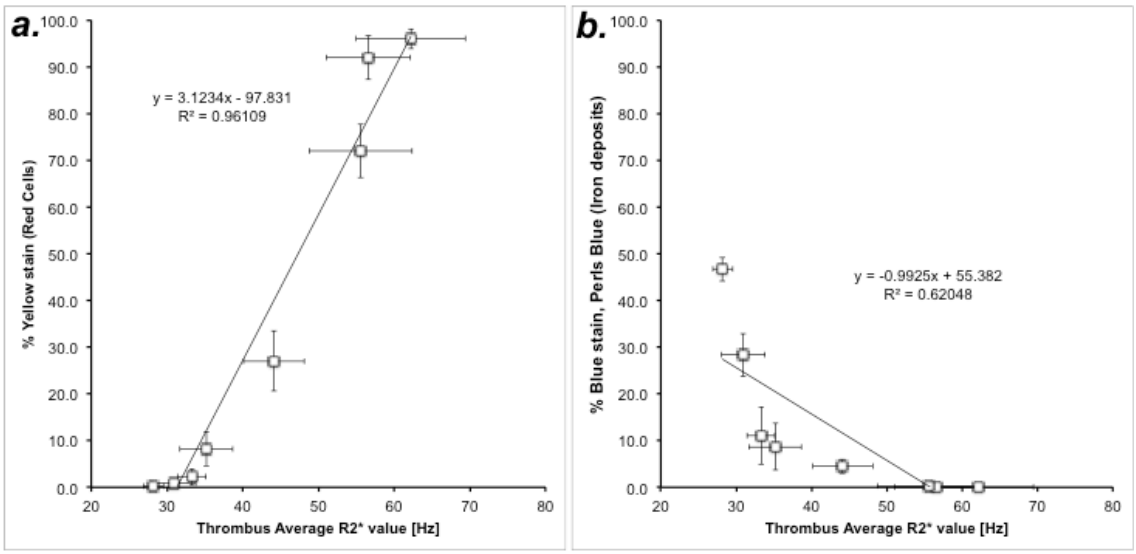

Figure 2.13- Thrombus Average R2* value [Hz] and its relation with the % of Perls' (a) and Red Blood Cell (b) stain of venous thrombus at different time points during thrombus organisation

2.4.4 Conclusion and Discussion

Red blood cells (RBCs) play an important role in the physiopathology of venous thrombosis. The cytoplasm of RBCs is rich in iron, which when released from a lysed RBC is highly inflammatory because of its oxidative effects on the endothelium (46). As trapped RBCs lyse, the iron contained in the cytoplasm is released and induces further RBC lysis. This leads to a positive feedback loop with increased areas of endothelial dysfunction, resulting in thrombus propagation (48). The isolation of this inflammatory injury would be one of the most important objectives of the thrombus formation.

R2* mapping has shown a good correlation with the total iron and red blood cell content in the thrombus, and therefore could be a useful technique to differentiate between young thrombus (rich in RBCs) from old thrombus (rich in collagen but with lower RBC content).

Additionally, it has been shown that the fibrin matrix in venous thrombi that are rich in red cells has a lytic resistance to classic thrombolytic treatments (66,86). Similarly, old thrombus with few RBCs but high collagen content was shown not to be amenable for thrombolysis. Therefore, R2* maps could be a useful tool to identify thrombus amenable for thrombolysis.

2.5 Magnetization Transfer Contrast (MTC)

2.5.1 Introduction

In biological systems, hydrogen nuclei or protons (^{1}H) can be grouped into two pools. The first one is called the *free pool*. This pool consists of relatively mobile protons that have similar precession frequency, which is reflected by its narrow spectral line (10-100 Hz) resulting in a long T2 transverse relaxation time. Furthermore, the *free pool* is “visible” to MRI (Figure 2.14a-b). The second pool is called the *bound pool*, and it includes the restricted protons that are bound to proteins, large macromolecules and cellular membranes. These protons have a very heterogeneous behaviour, which is reflected by their broad spectral line (10-50 kHz) resulting in a very short T2 relaxation time (<0.1 ms). These protons are not “visible” with conventional MRI sequences (Figure 2.14a-b) (77,78,80,87).

Under normal conditions, the magnetization is exchanged between the free pool and the bound-pool, reaching an equilibrium state, which is specific for each tissue. Using a Radio-Frequency

(RF) pulse it is possible to selectively saturate the signal of each pool and then to estimate the relative amount of free and bound protons in a specific tissue. If one selectively nulled the signal of the bound pool (Figure 2.14c), theoretically the signal of the free-pool should not be affected. However it has been observed that there is a decrease in the free pool signal, and this effect was attributed to the magnetization transfer from the bound proton pool to the free pool (87).

Currently there exist two MR methods to selectively saturate the “bound pool” (20,21). The first method employs the differences in widths of the resonance lines (Figure 2.14a). Frequency selective RF pulses are transmitted at a frequency-offset Δf with respect to the central proton Larmor frequency. Using these off-resonance pulses it is possible to substantially saturate the broad resonance of the “bound pool” while hardly affecting the “free pool”. The “off-resonance” RF pulse will not only saturate the spins with the specific off-resonance frequency but due to spin diffusion all macromolecule protons will be affected.

The second method employs the differences in T2 relaxation time between both pools. Binomial RF pulses with a resultant zero degree pulse angle are transmitted on-resonance. The most often used pulse is a 90°x 90°-x 90°-x 90°x pulse, with a pulse length of <0.5 ms per element. Due to the long T2 (much longer than the duration of the RF elements) the magnetization of the “free proton” is returned to the z-axis at the end of the binomial pulse. Mz Magnetization of “bound protons” with a very short T2 time is destroyed, because the dephasing of the transverse magnetisation is much faster than the duration of the RF elements. The net effect of such a pulse-train is that the Mz magnetization of the “free protons” is unchanged while the Mz of “bound protons” is destroyed.

Figures 2.14b-d demonstrates the basic principle underlying the MTC contrast (78,79,87). Here we consider a simplified biological tissue with a “free pool” of four proton spins, and a “bound pool” of one macromolecule with 3 proton spins (Figure 2.14b). Without application of a RF saturation pulse the signal-to-noise ratio of both tissues is 4 (arbitrary units). In the MT experiment a selective saturation pulses only affecting the bound protons is applied (Figure 2.13c). The bound protons are consequently saturated while the unbound protons are not affected. The next step in the MT process is that a portion of the saturated spins exchange their Mz magnetization with the non-affected spins of the “free-pool”. The result of this cross relaxation is that the SNR is decreased to 2 (arbitrary units) (Figure 2.14d). Tissues with a larger

proportion of bound-pool protons should have higher effect on the signal loss of the free-pool. This signal loss can be presented as a % signal loss or magnetization transfer ratio (MTR):

$$MTR = \frac{M_0 - M_{Sat}}{M_0}$$ Eq. 2.4

Table 2.1 shows the MTR (%) values for different tissues measured at 3T (88).

Tissue	MTR(%)
Liver	77 ± 5
Muscle	88 ± 2
Kidney	82 ± 1
Cartilage	85 ± 1
White matter	85 ± 1
Grey matter	84 ± 1
Spinal Cord	83 ± 1
Blood	11 ± 4

Table 2.1- Magnetization transfer ratio (MTR) at 3T (88).

MTC sequences have been successfully used to detect regions of organized proteins, like scar tissue, fibrous cap of atherosclerotic plaque and in tissue fibrosis (79,81,89,90).

As previously described, the two most important macromolecules in venous thrombus are fibrin and collagen, which have different sensitivities for magnetization transfer pulses and consequently result in different MT contrast (81). In this work we sought to optimize the MTC sequence in order to estimate the collagen content of venous thrombi *in-vivo* and thereby to detect the different stages of thrombus organization.

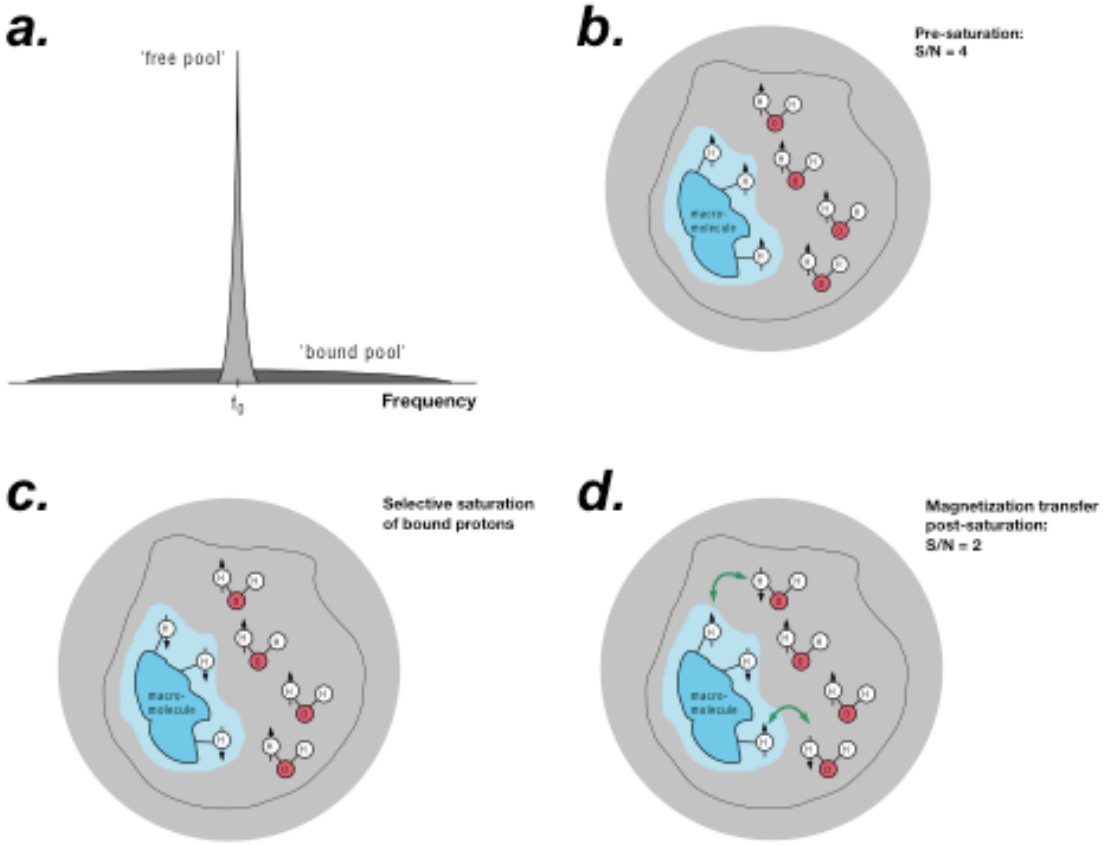

Figure 2.14- Basic principle of MTC contrast. (a) Spectral lines of the 'free pool" and the "bound pool" are both centred at the same Larmor frequency (f_0). The "free pool" has a narrow line (long T2 time) and the "bound pool" has a homogeneous broadened line (T2 < 0.2 ms). (b) Simplified biological tissue with a "free pool" of 4 four proton spins, and a "bound pool" of one macromolecule with 3 proton spins. In the MT experiment a selective saturation pulses for the bound protons is applied (c). The next step in the MT process is that a portion of the saturated spins exchanges magnetization with the non-affected spins "free-pool" spins (d). The result of this cross relaxation is that the S/N is decreased to 2 AU (adapted from (80))

2.5.2 Materials and Methods

Agar phantoms and in vitro thrombus

First, we optimized the acquisition parameters of the MTC sequence with agar samples as a model of organized proteins and using *in vitro* clots formed from freshly drawn blood that was allowed to organize for different time periods.

Blood was collected from healthy volunteers by venepuncture and allowed to form thrombi *in vitro,* which were washed with saline, placed in sealed Eppendorf tubes and imaged at 4 hours (fresh), 11 days (organized) and 17 days (lysed) after preparation. Between collection and imaging thrombi were stored at 4 °C to prevent dehydration. MRI was performed using a 3T Philips Achieva MR scanner (Philips Healthcare, Best, The Netherlands) and a single–loop

surface coil (diameter=47 mm). Three different MTC protocols were tested: 1) on resonance MT pre-pulse, 2) single off-resonance MT pre-pulse, and 3) multiple off-resonant MT pre-pulses.

Dynamic T1 weighted gradient echo 3D images were acquired without an MT prep-pulse and with the 3 MTC protocols. For the on-resonance scan the parameters were: TR=115 s, TE=6.8 ms, flip angle=18º, NEX=1, slice thickness=2.0 mm, acquired matrix=100x100, FOV=50x50 mm, reconstructed resolution=0.4x0.4 mm, scan duration=3 minutes. The on-resonance MT pre-pulse was a binomial block pulse (1:2:1, *90ºx 90º-x 90º-x 90ºx*) with a duration=1.92 ms, repetition=1 and offset=0 Hz. The single off-resonant MT pre-pulse was an adiabatic pulse with a sinc-gauss shape with an angle=620º, duration=17.5 ms, repetition=1, and offset=1100 Hz. For the multiple off-resonant MT pre-pulses four adiabatic pulses with an angle=700º, duration=20 ms, and offset=1, 200, 500, 800, 1000 Hz were used. Finally, off-resonant adiabatic MT pre-pulses with an angle=700º, duration=20 ms, offset=500 Hz, applied 4, 6 and 8 times were used.

In-vivo thrombus

A mouse venous thrombosis model was used as described in Section 2.2.1. The magnetization transfer rate (MTR) of *in vivo* thrombi was measured at days 1, 4, 7, 14, 21 and 28 after thrombus induction. Mice were imaged using a clinical 3T Achieva Gyroscan MR scanner (Philips Healthcare, Best, The Netherlands) equipped with a single–loop surface coil (diameter=47 mm). Arterial and venous time-of-flight (TOF) images were used to locate the thrombus. Dynamic T1GRE 3D images were acquired without and with an on resonance MT pre-pulse. Imaging parameters included: TR=115 s, TE=16 ms, flip angle=18º, NEX=1, slice thickness=0.4 mm, acquired matrix=148x150, reconstructed resolution=0.1x0.1 mm, scan duration=6 minutes. The MT pre-pulse was a binomial block (1:2:1, 90ºx 90º-x 90º-x 90ºx) pulse with a duration=1.92 ms, repetition=1 and offset=0 Hz.

Image Analysis

MTR maps were generated based on the Eq. 2.4 using OsiriX (The Osirix Foundation, Geneva, Switzerland).

2.5.3 Results

We first optimized acquisition parameters with agar samples as a model of organized protein and *in vitro* clots formed from freshly drawn blood that was allowed to organize for different time periods. For MTC three parameters were tested: 1) an on resonance MT pre-pulse, 2) an off-resonance MT pre-pulse, and 3) multiple off-resonant MT pre-pulses. An example of the application of an on-resonant MT pre-pulse is illustrated in Figure 2.15.

Incremental MT effects (increased signal reduction) were observed in samples with a higher concentration of agar. A similarly higher MT effect was observed in organized compared to fresh and lysing thrombus. The corresponding histology shows that fresh thrombus was rich in erythrocytes while organized thrombus contained abundant collagen fibres (blue staining) and the lysing thrombus contained degraded collagen fibres and lysed erythrocytes.

The % MTR revealed a linear correlation with the agar concentration at 3T for both the on-resonant and off-resonant MT pre-pulse (Figure 2.16a). However, the MT effect was more prominent when the MT pre-pulse was applied on-resonance. A significantly higher MTR was observed for the organized compared to the fresh and the lysing thrombus, and this effect was also more pronounced when the MT pre-pulse was on-resonance (Figure 2.16b). The effect of the offset frequency and the number of repetitions (number of pre-pulses) was investigated by applying multiple MT pre-pulses. Figure 2.17a shows that the off-resonance MT pulse should be applied at least 500 Hz away from the resonance frequency of the free water peak to avoid a direct MT saturation effect of the free water protons. Figure 2.17b shows that when the offset frequency is set to 500 Hz the MTR monotonically increased with the number of repetitions in the agar samples.

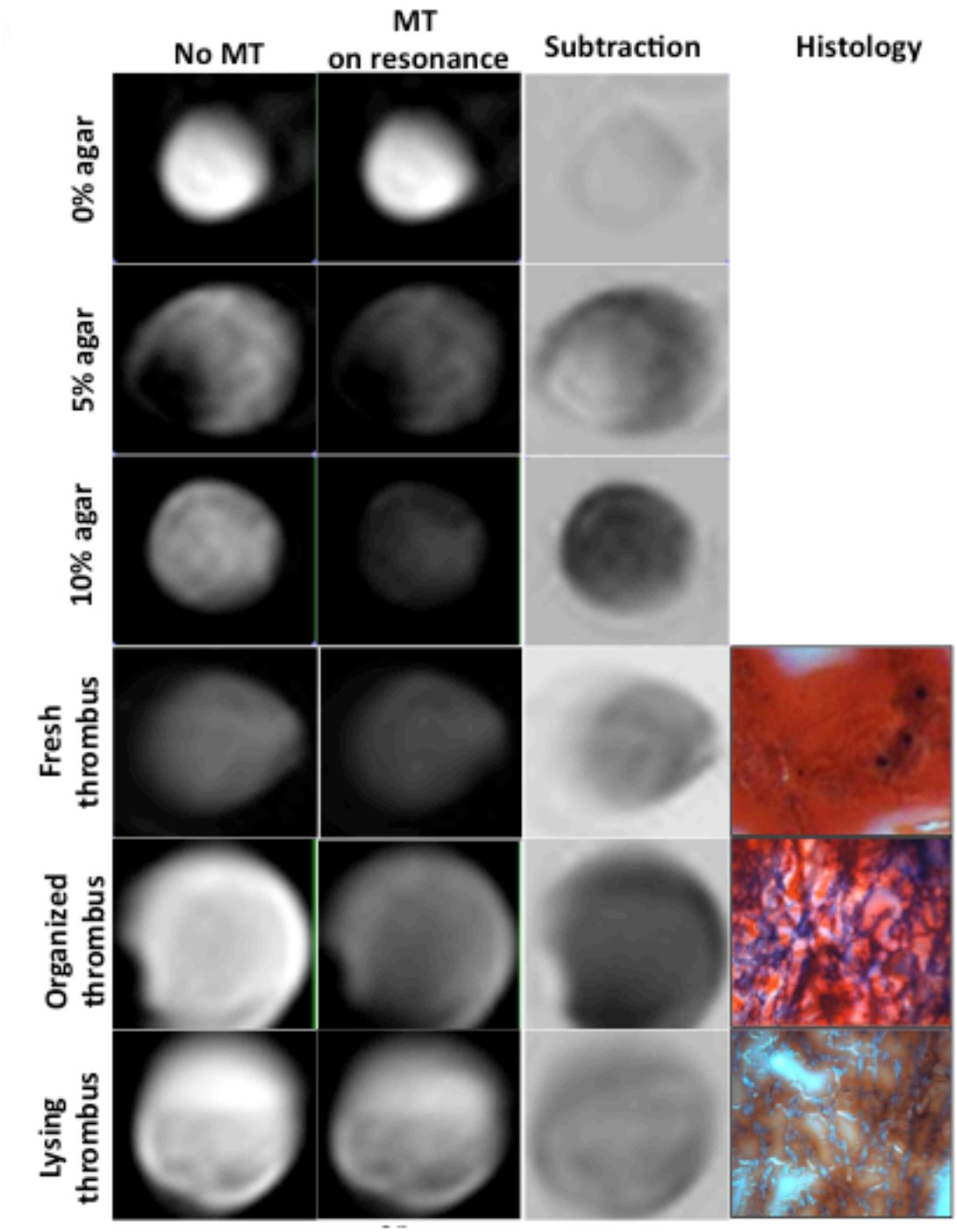

Figure 2.15- Example of on-resonance magnetization transfer. Agar phantoms with increasing concentration of protein showed a gradually higher MTR (more hypointense subtracted images). In vitro thrombi showed the higher MTR in the organized stage (contained abundant collagen fibres (blue staining), followed by fresh thrombus (rich in erythrocytes) and lysed thrombus (contained degraded collagen fibres and lysed erythrocytes).

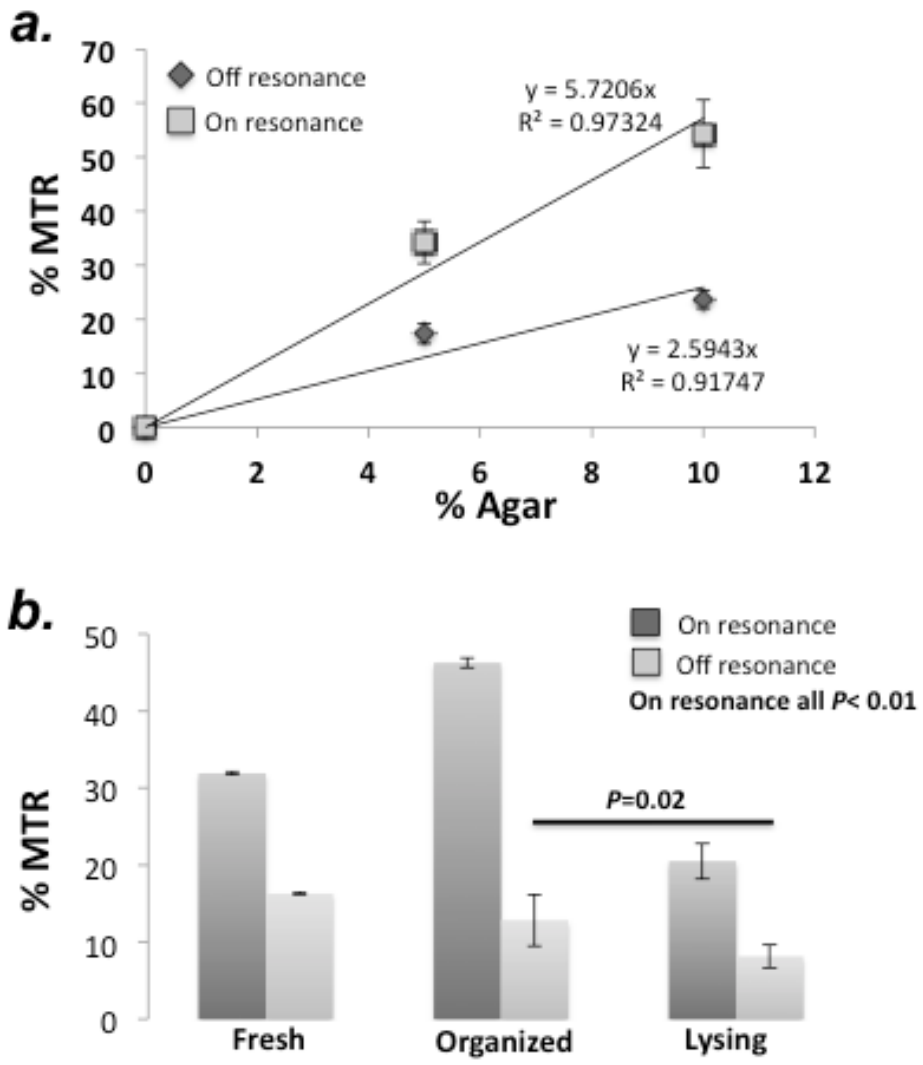

Figure 2.16- Quantification of the magnetization transfer rate in agar samples and in-vitro thrombus at 3T. (a) There was a linear correlation between the protein composition and the % MTR for both the on-resonance and off-resonance MT. However, a higher MTR was achieved for all the samples using on-resonance MT. (b) There was a significantly different %MTR between fresh, organized and lysed thrombi using the on-resonance MT; whereas the %MTR was statistically different only between organized and lysed thrombus using the off-resonance MT.

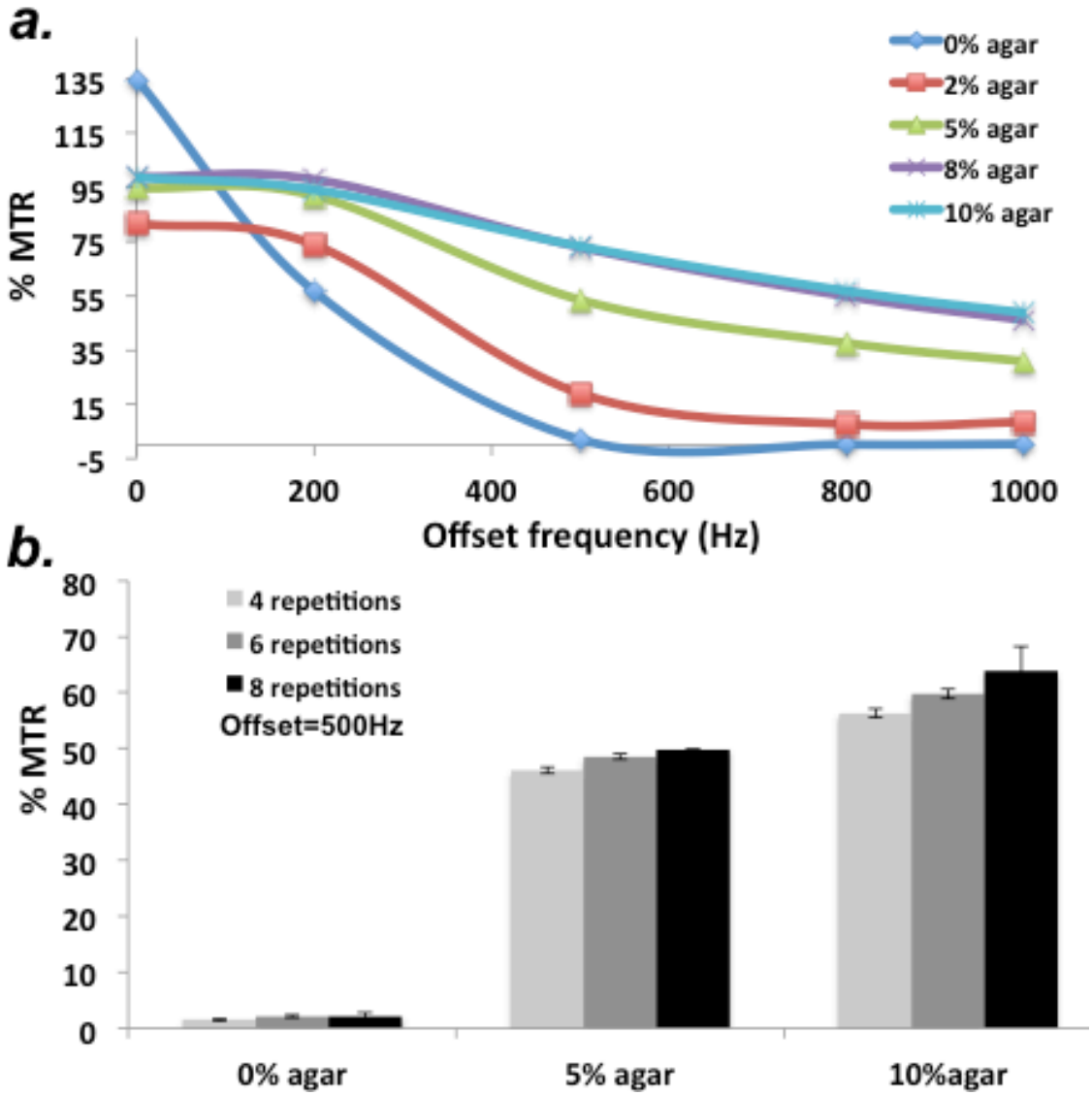

Figure 2.17- Effects of offset frequency and number of pre-pulses for the off-resonance MT. The offset pre-pulse needs to be applied at least 500 Hz away from the resonance frequency of free water to avoid direct magnetization transfer effects. Keeping the offset frequency at 500 Hz there was a small increase in the %MTR with additional pre-pulses.

Because of its higher MTR effect and the significant difference between the MTR effect of fresh and organized thrombus, we decided to use the on-resonance MTR protocol for the *in-vivo* MTR acquisitions.

Figure 2.18 shows representative images of the mice thrombus' MTR maps at different time points of thrombus organization. In the coloured MTR map, the green-red areas represent a high MTR effect , which are in agreement with a higher protein content.

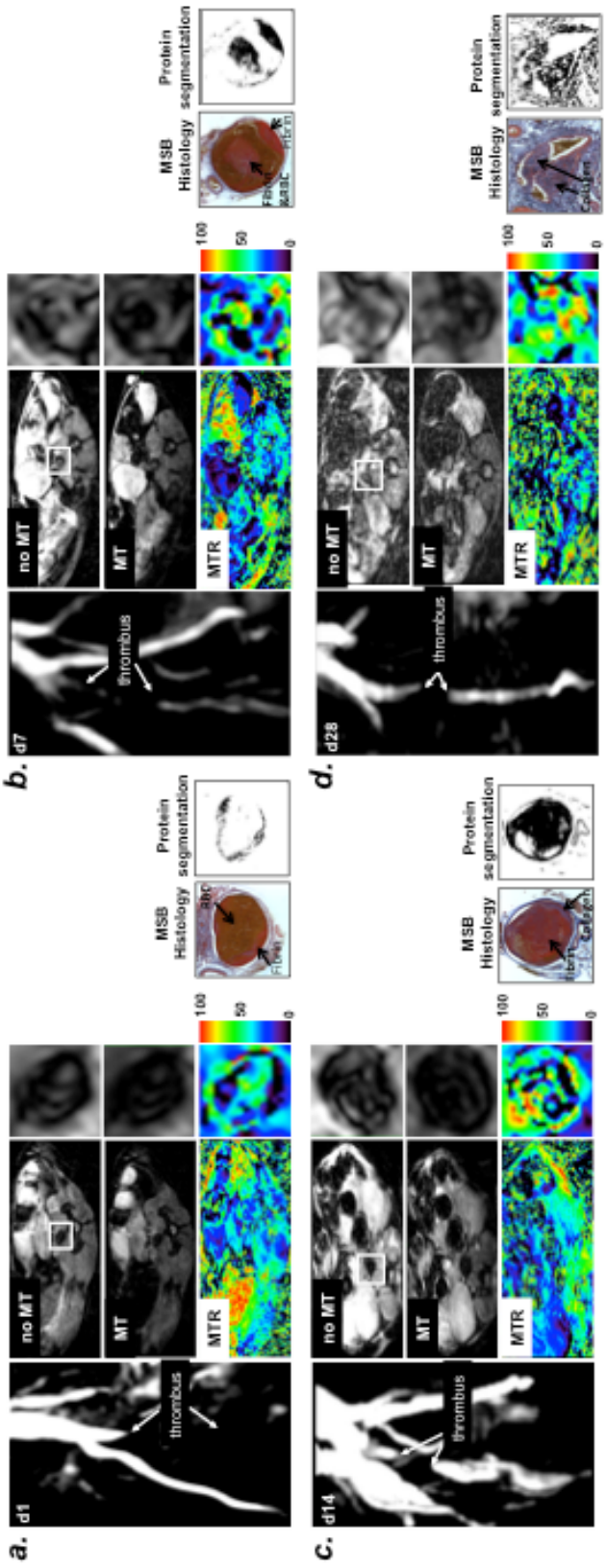

Figure 2.18- Venous thrombus localization on TOF venography. Transverse images acquired with and without magnetization transfer. Magnetization transfer rate maps and MSB histology of venous thrombus at (a) Day 1, (b) Day 7, (c) Day 14 and (d) Day 28, since thrombus induction

Figure 2.19 shows the MTR values at different time points during thrombus resolution and the average (%) protein content (collagen and fibrin) of thrombus. The graphs show 2 sub-populations: the first one with small MTR affect, which correspond to young thrombus mainly formed by RBCs and fibrin (which has a weak MT effect), and a second sub-population with higher MT effect, which correspond to old thrombus, rich in collagen.

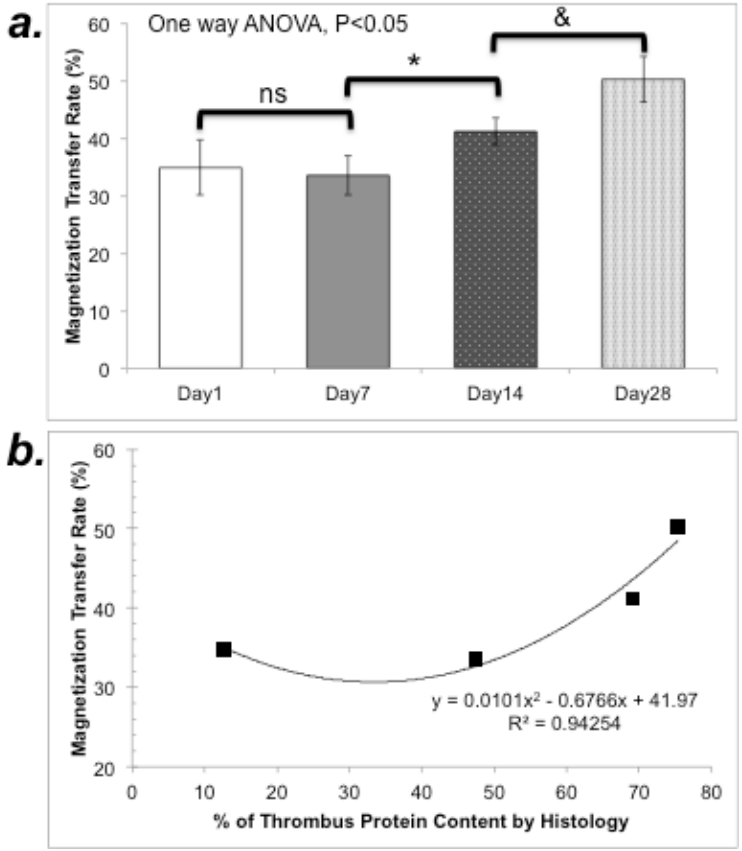

Figure 2.19- MTR (%) in relation with the thrombus stage of resolution (a) and the % of thrombus protein content (collagen and fibrin composition) (*=P<0.05, &=P<0.01)

2.5.4 Conclusion

MTC has been successfully used to suppress the signal from static background tissues to improve MR angiography and also to characterize white matter disease in the brain, mostly multiple sclerosis (80). In this section we demonstrate that the MT contrast also can be used to differentiate between thrombus with different protein content. Because RBCs and fibrin are the main components of young thrombus and collagen is mainly present in old thrombus, this technique is promising for the non-invasive detection of histological changes that occur during thrombus organisation.

2.6 T1 Relaxation Time mapping

2.6.1 Introduction

It has been shown that venous thrombus can be detected using T1-weighted MRI and it has been speculated that this effect is related to Methemoglobin (Hgb(Fe^{+3})) formation in thrombus during its organisation (73,74). However this hypothesis has not been demonstrated yet, and thrombus T1 effects have not been correlated with the stage of thrombus organisation. In this section we sought to correlate thrombus organisation with the T1 relaxation time and the methemoglobin concentration.

2.6.2 Materials and Methods

MRI Protocol

A fast 3D Look-Locker based T1-mapping sequence was used in this study (76). After the acquisition of arterial and venous TOFs, and measurement of flow velocity across the IVC (section 1.6), the venous TOF dataset was used to plan the location of the 3D T1-mapping sequence. A 3D volume covering the whole thrombus in 30 slices with a voxel resolution of 0.2x0.2x0.5 mm^3 was planned to acquire 16 time-points for each pixel. A long relaxation delay of 3s after each acquisition was employed to ensure magnetization recovery. The other sequence parameters were: TR/TE=9.0/4.6 ms and flip angle=10°. Total scan time for this sequence was 28 minutes. T1 maps were calculated for each slice using custom-made software implemented in Matlab (Mathworks, Natick, MA, USA) (Figure 2.20).

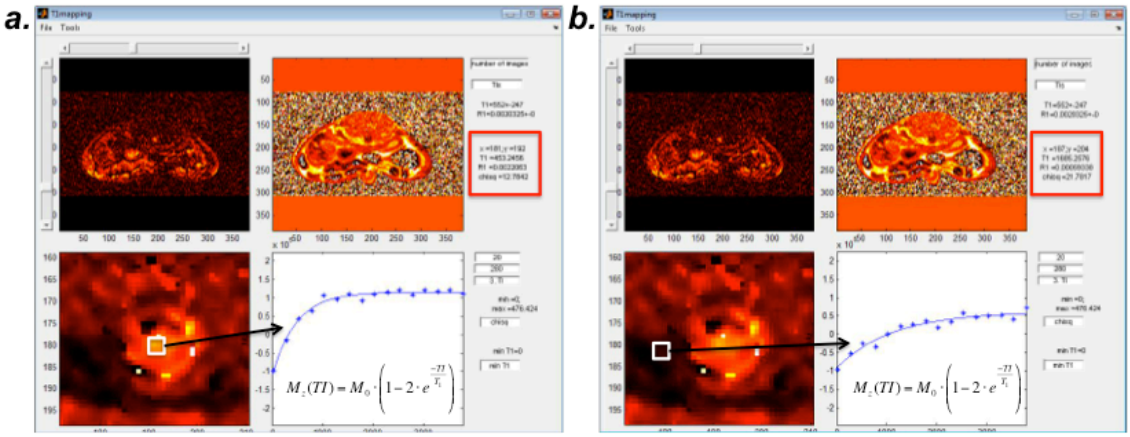

Figure 2.20- T1 Relaxation time calculation methodology. Acquired images were imported into custom-made software implemented in MATLAB and analysed to quantify thrombus T1 relaxation time on a pixel-by-pixel basis. Average T1 relaxation times were calculated in a selected area of interest for each slice. (a) Shows an area of interest with a short T1 relaxation time and (b) and area with long T1 relaxation time.

In order to detect the T1 effect of the Methemoglobin using MRI two requisites are needed: firstly the presence of Methemoglobin and secondly the availability of free water protons in order to obtain a measurable MR signal. One *in vitro* study has shown that ADC maps could be related with the water content in thrombus (91). Very old thrombus, rich in collagen, has very restricted water diffusion and leading to a low content of water.

In order to estimate the water content of the thrombus, a diffusion-weighted image of the thrombus was obtained in order to calculate the Apparent Diffusion Coefficient (ADC). The MR parameters used were: 2D diffusion-weighted spin echo images with: TR=2.8 s, TE=105 ms, flip angle=90º, diffusion echo time=333 mm, FOV=18x30x12 mm^3, acquired matrix=88x150, slice thickness=0.5 mm, acquired resolution=0.2x0.2 mm^2, reconstructed resolution=0.1x0.1 mm^2, slices=24, averages=2, and scan duration of 36 minutes. Diffusion gradients were applied, parallel and perpendicular to the external magnetic field. The apparent diffusion coefficient (ADC) was calculated from 4 b-values = 0, 333, 667, 1000 mm^2/s, based on the equation:

$$ADC = \frac{\ln(S_0 - S_1)}{b_1 - b_0} \qquad \text{Eq. 2.5}$$

Where, S_i is the signal intensity of the area of interest obtained when b-values = b_i.

Iron measurement

Total thrombus iron content was measured using ICP-MS methodology and Methemoglobin (Fe^{3+}) was measured using a commercial kit (Quantichrom Iron Assay Kit, BioAssay Systems, CA, US) as described in section 2.2.2.

2.6.3 Results

The mean T1 relaxation time of normal blood was found to be 1478 ± 86 ms. Thrombus was defined as intraluminal pixels in the IVC with a T1 value lower than the measured blood T1 relaxation time in normal vessel segments minus two standard deviations, i.e. we used a cut off point of 1300 ms.

Mean T1 relaxation time changed during thrombus organisation (One-way ANOVA, $P<0.01$, Figure 2.21). The Average T1 relaxation time showed an “U” shape evolution during thrombus organisation. In the first phase, the T1 relaxation time decreased reaching a minimum plateau between Day 4 and 10 with a T1 of approximately 750 ms. After this plateau, the thrombus T1

relaxation time increased consistently until Day 28. No significant differences were found between the average T1 relaxation time between day 4 and 7, and between day 7 and 10 (Bonferroni post-hoc test). This T1 shape is consistent with the hypothesis that the formation and later degradation of methemoglobin could be the main "source" of the shorter T1 relaxation time.

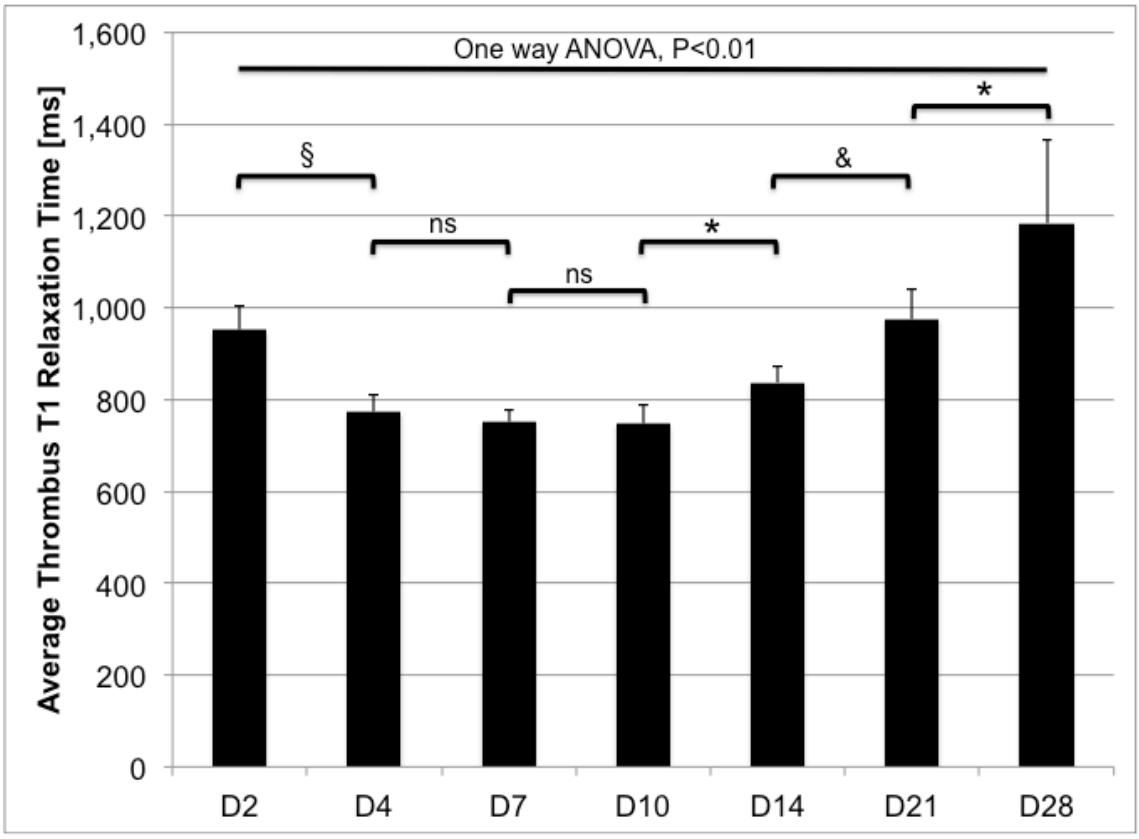

Figure 2.21- Average T1 relaxation time (ms) of thrombus during its resolution. One-way ANOVA with Bonferroni post-hoc test analysis (*=P<0.05, &=P<0.01, §=P<0.001, ns: non significant)

Fe^{3+} content measured in µg/dl per mg of thrombus was found to change during thrombus organisation (P<0.01, One way ANOVA, Figure 2.22). The concentration of Fe^{3+} increases during the first stage of thrombus organization, reaching a maximum of 6.6 mg/dl per mg of thrombi. After this maximum, the Fe^{3+} content decreases in the second stage of thrombus organisation. This behaviour mirrors the T1 relaxation time during thrombus organisation (Figure 2.21 and 2.22). However, both curves are slightly displaced relative to each other, because the maximum Fe^{3+} content does not coincide with the minimum T1 relaxation time. In fact, there is a significant but weak linear relationship between T1 relaxation time and Fe^{3+} content at different time points when each pair of measurements are taken from the same

mouse (Figure 2.23, R^2=0.469, P<0.001). This result suggests that there may be additional variables that affect the T1 relaxation time.

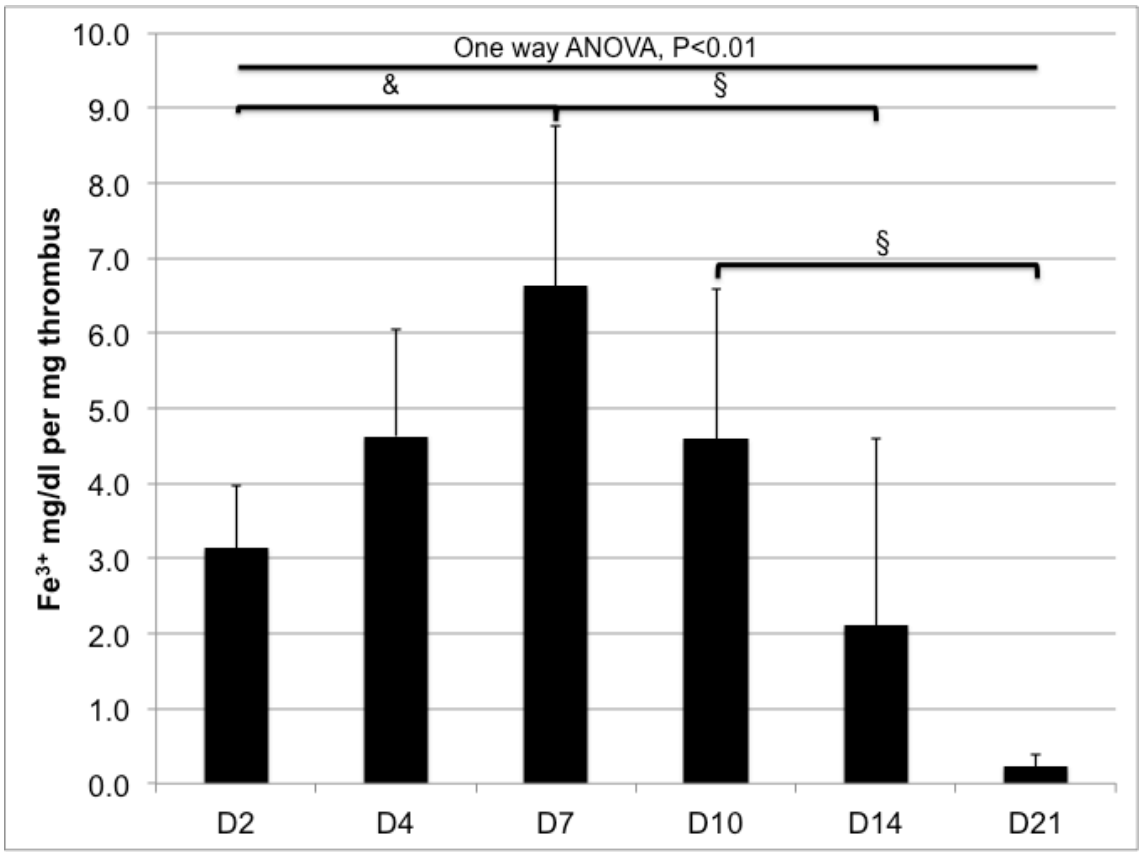

Figure 2.22- Fe^{3+} concentration (µg/dL per mg of thrombus) at different time point during thrombus organisation. One-way ANOVA with Bonferroni post-hoc test (*=P<0.05, &=P<0.01, §=P<0.001, ns: non significant)

We thus calculated ADC maps for all thrombi at different time points. In order to have an internal control, we also estimated the ADC values of muscle and free water (represented by the urine from the bladder) in each mouse. Figure 2.24 shows the relation between S/S_0 and the b-factor (Eq. 2.5). Free water (non restrictive water diffusion tissue) and muscle (more restrictive water diffusion tissue) are the minimum and maximum curves in this graph while the thrombus S/S_0 values are in between both curves, showing a behaviour that could be related to its stage of organisation.

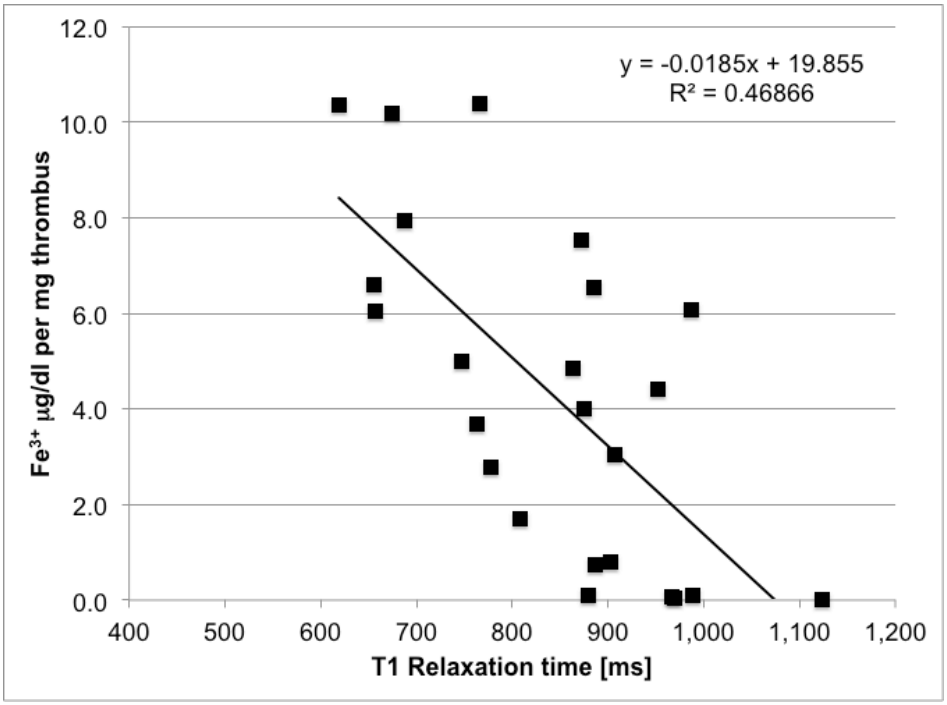

Figure 2.23- Relationship of Fe^{3+} concentration (µg/dL per mg of thrombus) and T1 relaxation time measured in the same group of mice at different time points during thrombus organisation.

Figure 2.25 shows the average ADC values at different time points of thrombus organisation. In the early stages the membranes of dead RBCs act like a barrier for water diffusion and the thrombus shows a restricted diffusion pattern with low ADC values. As soon as thrombus is cleared of dead RBCs and the fibrin matrix becomes its main component, thrombus showed a slight increase in water diffusion, reaching a maximum between day 10 and 14. In the latest stages, when mainly a collagen rich scar forms the thrombus, it showed again a restricted diffusion pattern with low ADC values. To acquire ADC images at 3T with this level of resolution is challenging and results in considerable noise, which could explain the lack of strong statistical differences during thrombus organisation (Figure 2.26)

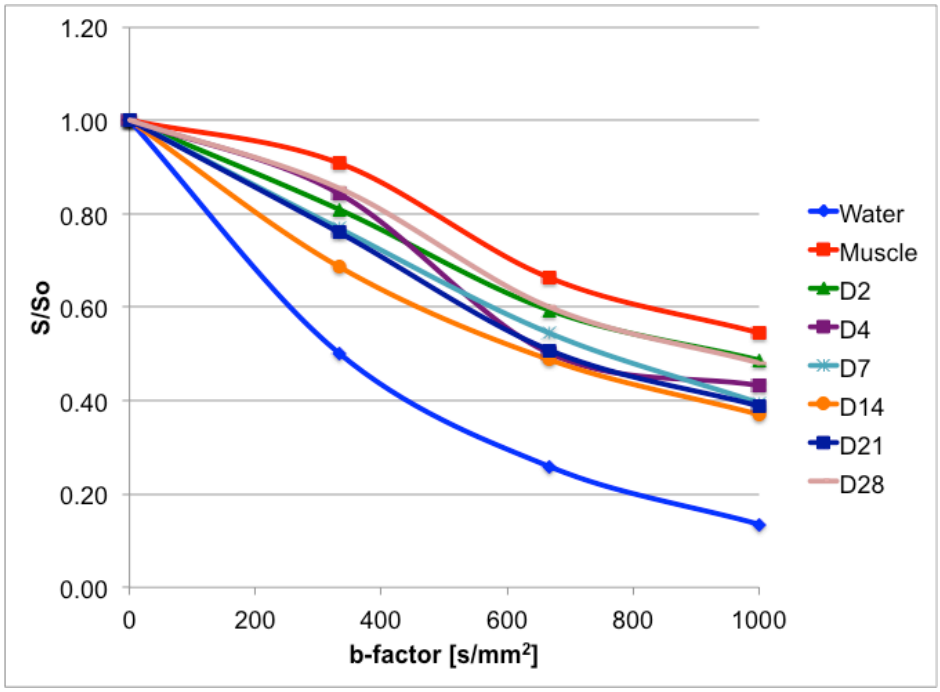

Figure 2.24- Signal intensity measured with b-factor=0 (S_0) and b-factor=333, 667, 1000 mm^2/s (S) for free water (urine in the bladder), high restricted tissue (muscle) and venous thrombus at different organisation time point.

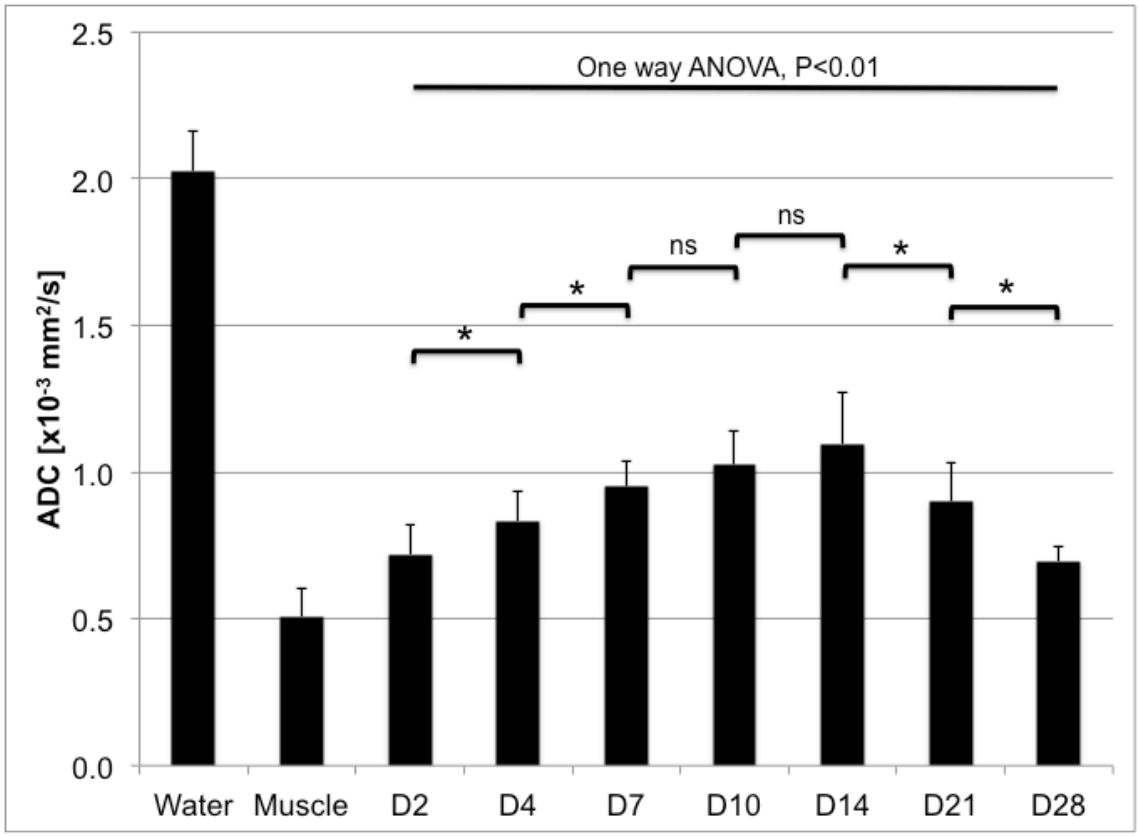

Figure 2.25- Average ADC values [$x10^{-3}$ mm^2/s] of free water (urine in the bladder), high-restricted tissue (muscle) and venous thrombus at different organisation time point (*=P<0.05, &=P<0.01, §=P<0.001, ns: non significant)

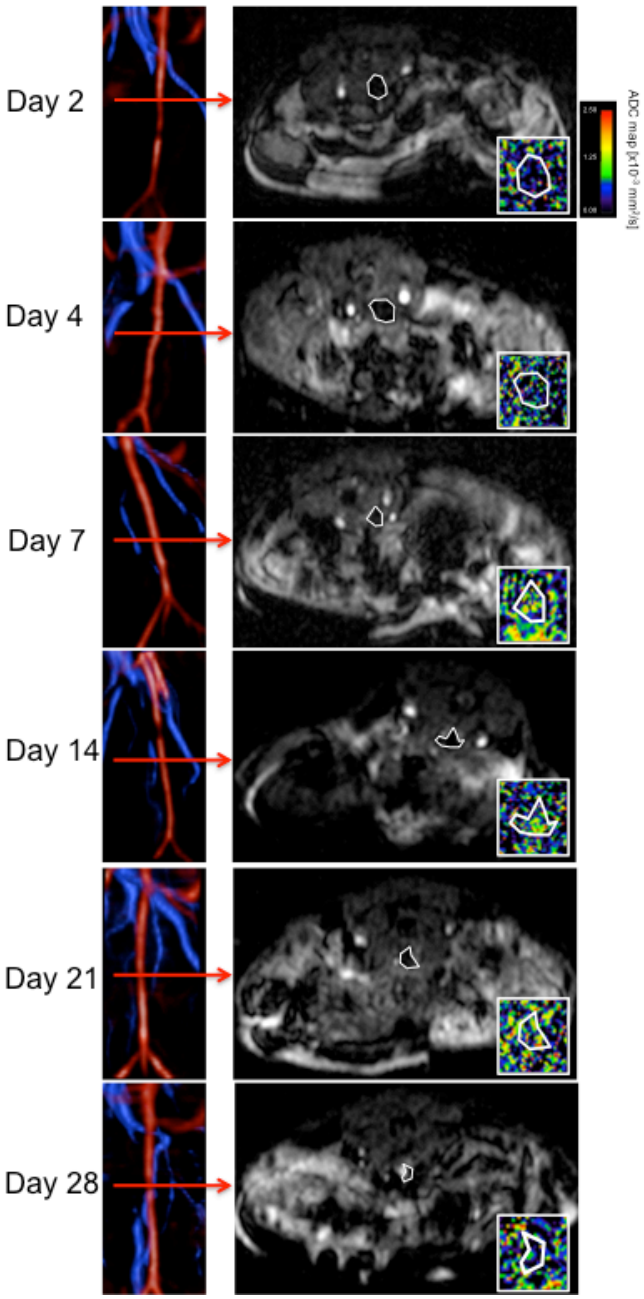

Figure 2.26- ADC maps at different thrombus organisation time point. The segmentation of the thrombus was done using the Phase Contrast and TOF images, and the region of interest was exported to the ADC maps (blue colours represent high restrictive tissues for water diffusion and green-red colours low restrictive tissues for water diffusion).

There was also a weak correlation between ADC values and T1 relaxation times of the thrombus during its resolution (R^2=0.259, P<0.05, Figure 2.27).

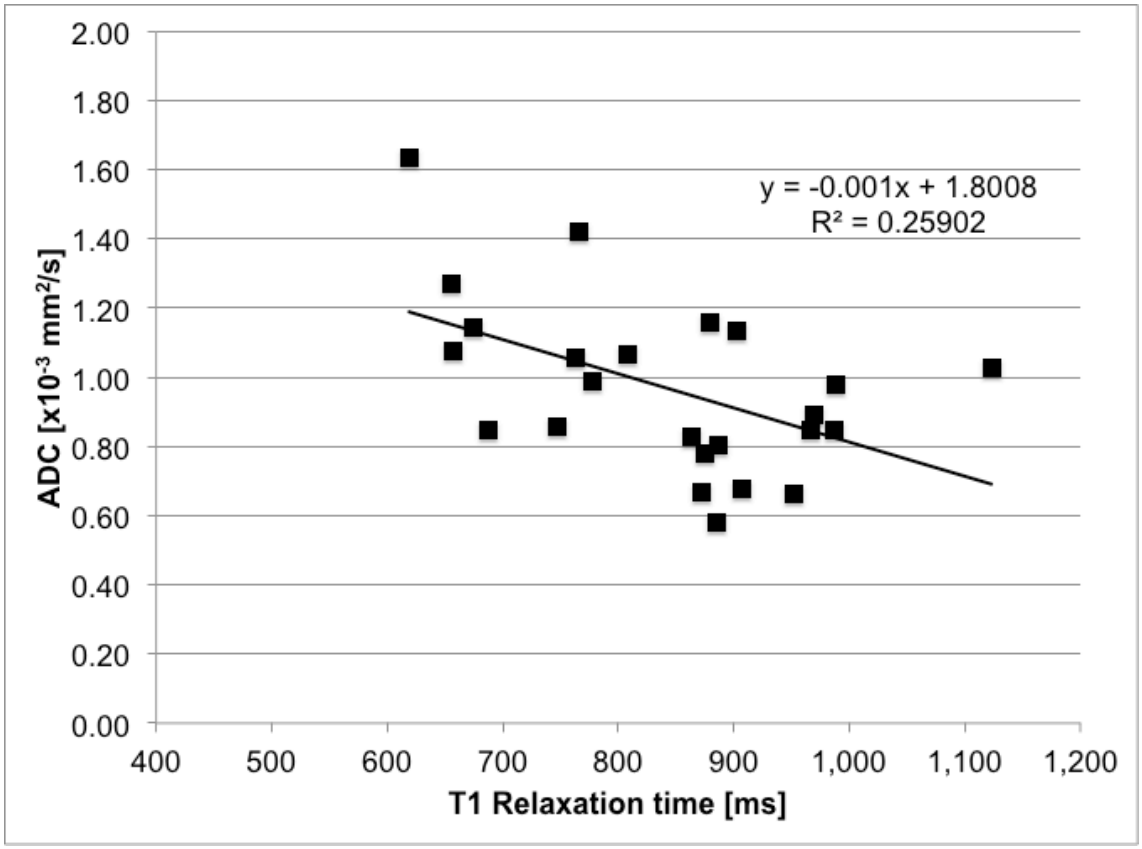

Figure 2.27- Relationship of ADC values ($x10^{-3}$ mm^2/s) and T1 Relaxation time measured in the same group of mice at different time point during thrombus organisation.

When we combined the effect of both parameters: Fe^{3+} concentration and ADC values (as a marker of proton availability), a better correlation was found (Figure 2.28, R^2=0.719, P<0.0001, β_{ADC}=0.31 (CI95%:0.085-0.534) and β_{Fe3+}=0.032 (CI95%:0.016-0.048).

Fe^{3+} and ADC by itself are not good predictors of the T1 relaxation time, however its combination results in an improvement of the model with Fe^{3+} having the strongest effect (Figure 2.28).

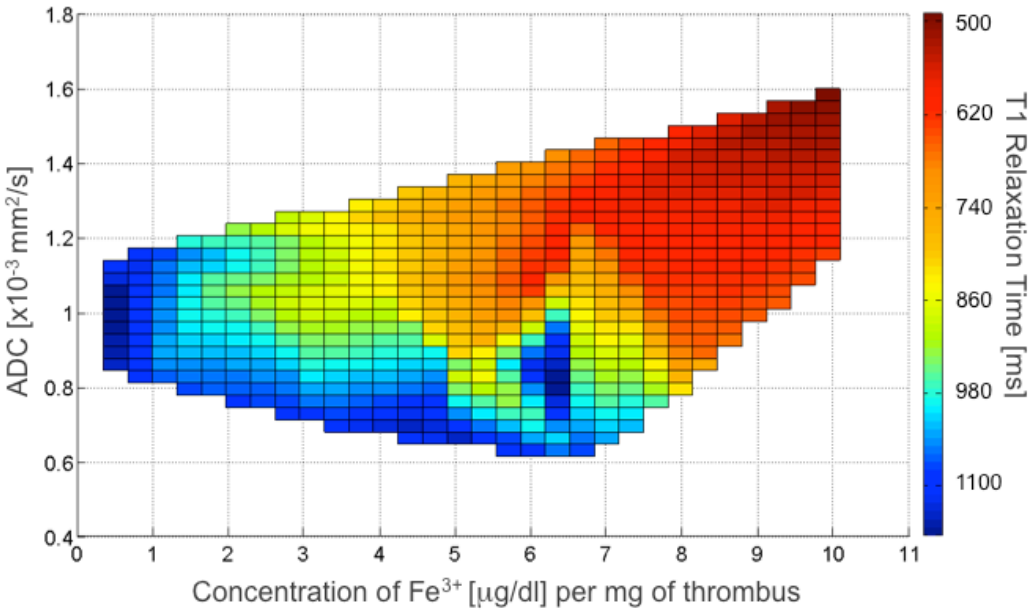

Figure 2.28- Relationship between ADC mapping, Fe^{3+} content and T1 relaxation times of thrombus. The graph shows that presence of Fe^{3+} and water protons (measured by the ADC) are necessary to obtain a T1 effect that can be detected by proton MRI (Multivariate linear regression, R^2=0.719, P<0.0001)

2.6.4 Discussion

Our results confirm that the low T1 relaxation time observed during thrombus organisation is the consequence of the formation and degradation of methemoglobin (Fe^{3+}), but also related with the availability of protons in the surrounding environment of methemoglobin. The different stages of thrombus resolution create favourable conditions for the formation of methemoglobin, mainly in the earliest stages. Additionally restriction of water diffusion during thrombus formation and organization play an important role in the creation of a measurable T1 effect using MRI. All of those biological consequences of thrombus organisation are very well represented in the T1 maps and could be used to better identify the stage of thrombus organisation at the moment of diagnosis.

2.7 Conclusions

In this chapter we have shown that there are several techniques that could help visualizing the dynamic changes during thrombus organisation and resolution.

Very young thrombi are typically very occlusive and therefore create the largest filling defect in the IVC. Histologically they are less organized, without a tight fibrin matrix and full of RBCs. From a MRI point-of-view this stage of organisation showed the lowest T2* value (because of the iron content in the RBCs), low MTR effect because the lack of fibrin and collagen proteins and a moderate T1 relaxation time despite the high methemoglobin content of the thrombus. It has been suggested that young thrombi do not respond well to thrombolytic therapy because of the lack of a cross-linked tight fibrin matrix. In addition RBCs surrounding fibrin provide resistance to classic fibrin targeted thrombolytic therapies (66,86,92).

In contrast, in very old thrombi the fibrin matrix has been replaced by a collagen rich scar tissue with no to little RBCs. These thrombi showed a small T2* effect because of the lack of RBCs while small amounts of hemosiderin was found at this stage. These thrombi also had the highest MTR effect because the high collagen content and a long T1 relaxation time because of the lack of methemoglobin at this time point.

Thrombi in the intermediate organisation stage showed a mixed behaviour. T2* relaxation times increased consistently as a result of decreased RBC content and therefore reduced iron content in these thrombi. The high concentration of methemoglobin and the availability of protons (high ADC values) generated a strong T1 effect leading to a decrease of the T1 relaxation time. Additionally the MTR affect had an intermediate value, which was between the young and old thrombus. At this stage thrombus is primarily composed of a tight fibrin matrix and therefore ideally suited for thrombolytic therapy.

Figure 2.29 shows the average thrombus T2* and T1 relaxation time at different time points. It is possible to visualize the “route of thrombus organization” as very clear “steps” during thrombus organisation, starting from very young thrombi with moderate T1 relaxation time and short T2* time, until very old thrombi with long T1 relaxation time and long T2* values. Using this graph it is possible to estimate which venous thrombus is amenable for thrombolysis and it should be located in the intermediate region (day 4, 7 and 10) characterized by a high fibrin, low collagen and low RBC content. This hypothesis will be further studied in the following chapters.

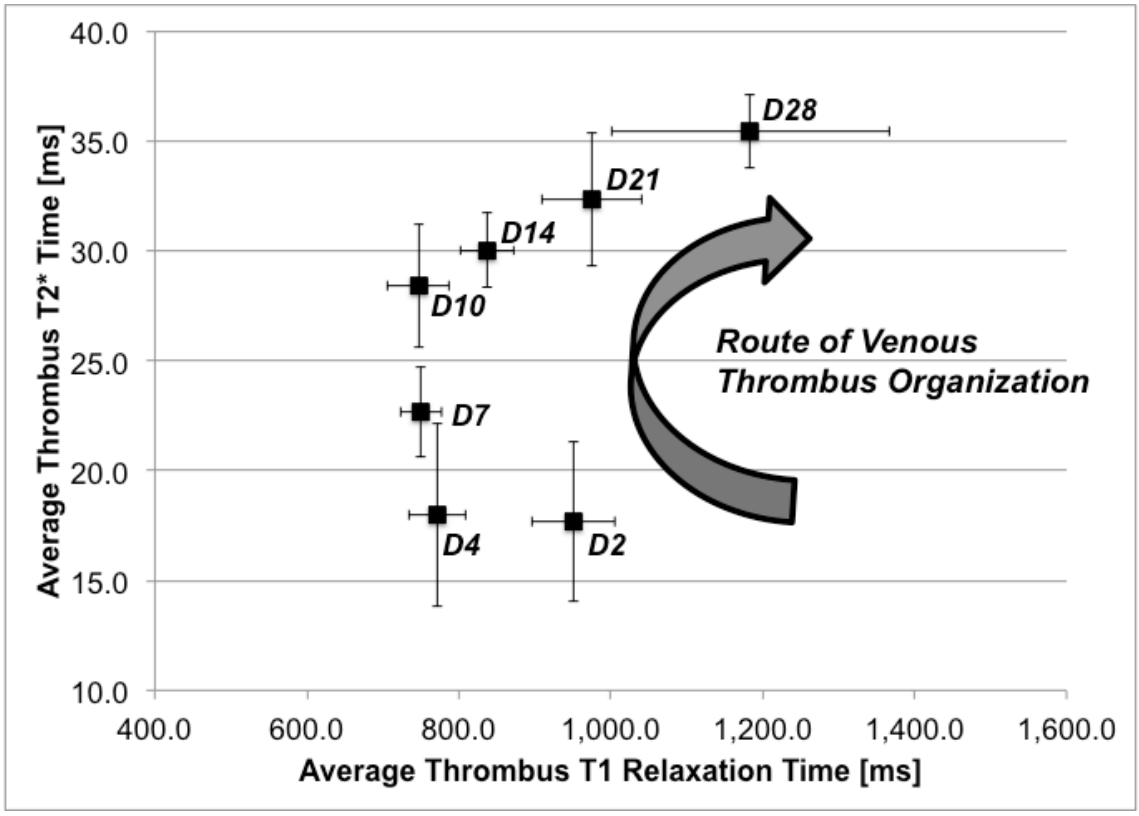

Figure 2.29- Temporal relationship between T2* and T1 relaxation time during thrombus organisation. The graphs shows a very well define steps during thrombus organisation, the “Route of venous thrombus organisation” that reflect the change in the RBC and Methemoglobin content.

In summary, the experiments carried out in this chapter demonstrate that it is feasible to visualise murine thrombus *in vivo*; measure the blood flow across the IVC with phase contrast angiography; and obtain several MRI parameters like: MTC, ADC, T2* and T1 relaxation times of thrombus during its organization and resolution. All of these parameters are correlated with the thrombus histological changes during its organisation.

Chapter 3 Venous thrombus characterization using a Gd-based fibrin specific contrast agent

3.1 Aims and objectives

Venous thrombi resolve by a process of organisation similar to the formation of granulation tissue in healing wounds (43,48). The formation, organisation and degradation of the fibrin matrix is a key event in the natural history of thrombus resolution (43-45,48,49,53). We hypothesised that fibrin targeted MRI would provide information on molecular composition of thrombus and that the accurate quantification of fibrin-specific contrast agent uptake *in-vivo* could therefore serve as a surrogate marker of the stage of thrombus organisation at the time of diagnosis. Additionally, as thrombolytic therapies target fibrin this protein could represent a good imaging target for the guidance of thrombolytic therapy (23,45,54).

MRI is a radiation free imaging modality, which with the development of new protein and cell specific contrast agents, provides the opportunity to diagnose disease not only at a morphologic but also on a molecular level thereby providing new insights into pathophysiology *in-vivo* (54).

EP-2104R is a Gd-based contrast agent that binds strongly and reversibly to fibrin (56,57,93). The use of EP-2104R has been shown to be successful in the detection of arterial and venous thrombi in animal models and man (56-58,93-95). The use of this agent has not, however, been used to characterize venous thrombus composition during its organisation.

In this chapter we therefore sought to investigate whether fibrin specific MRI (FSMRI) would allow accurate staging of venous thrombus organisation.

3.2 Materials and Methods

3.2.1 DVT mouse model

Venous thrombosis was induced in the inferior vena cava (IVC) of 8-10 weeks old male BALB/C mice as was described in section 1.5.1. MRI was performed at day 2, 4, 7, 10, 14 and 21 following thrombus inductions. Eight mice were scanned at each time point pre and 2 hours post injection of a gadolinium based, fibrin-specific MRI contrast agent, EP-2104R (EPIX Pharmaceuticals, Lexington, MA)(56,57,93,94) (Figure 3.1). Two additional mice were scanned at each time point 20 minutes post injection of 0.2 mmol/kg of Gd-DTPA (Magnevist, Bayer

HealthCare AG, Berlin, Germany) and excised thrombi were analysed with ICP-MS to quantify non-specific contrast uptake (Figure 3.1).

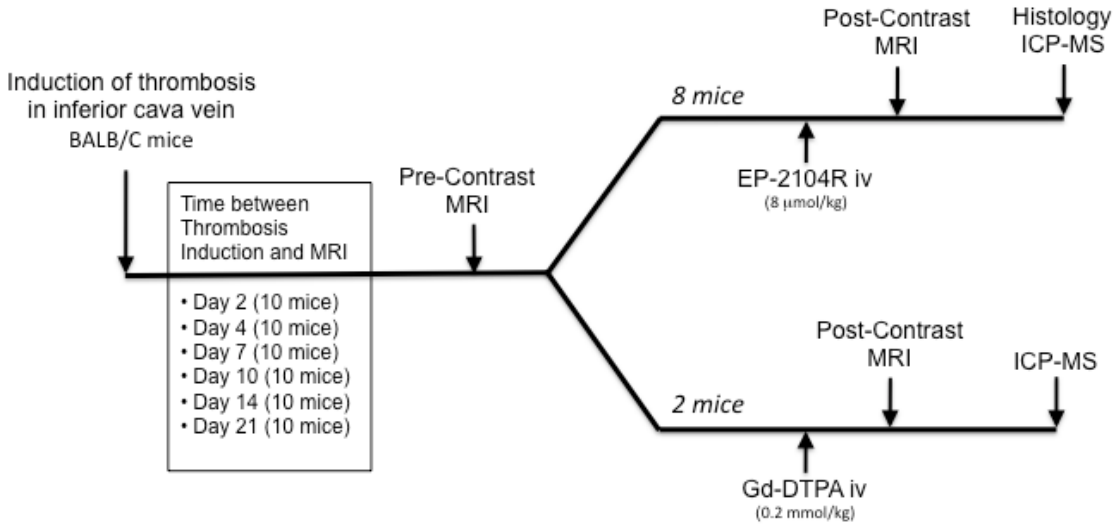

Figure 3.1- Study design. Ten mice were scanned at each time point (day 2, 4, 7, 10, 14 and 21) after IVC thrombosis induction. At each time point, 8 mice were scanned pre and post EP-2104R injection. Additional 2 mice were scanned pre and post Gd-DTPA injection. Subsequently venous thrombi were harvested and analysed using ICP-MS for Gd uptake quantification and histology for biological composition

Fibrin contrast agent

EP-2104R is a Gd-based, fibrin-binding contrast agent with four Gd moieties (56,57,93). EP-2104R binds equally to two sites on human fibrin (Kd=1.7±0.5 μM) and has a similar affinity to mouse, rat, rabbit, pig, and dog fibrin. EP-2104R has excellent specificity for fibrin over fibrinogen (over 100-fold) and for fibrin over serum albumin (over 1000-fold) (56). The relaxivity of EP-2104R bound to fibrin at 37 °C and 1.4 T was 71.4 $mM^{-1}s^{-1}$ per molecule of EP-2104R (17.4 per Gd), about 25 times higher than that of Gd-DOTA measured under the same conditions. In this study a dose of 8 μmol/kg of EP-2104R was used. The fibrin scans were performed 2 hours post EP-2104R injection to allow for contrast agent blood clearance and to minimize background signal (57,58,93).

MRI Protocol

Mice were anesthetized with 1.5-2% isofluorane and 100% oxygen delivered through a nose cone and scanned in prone position on a 3T Philips Achieva Gyroscan MR scanner (Philips Healthcare, Best, The Netherlands) equipped with a dedicated 47 mm small animal surface coil. A late gadolinium enhancement inversion recovery (LGE-IR) 3D segmented gradient echo

(TFE) sequence was performed to selectively visualise thrombus pre and post contrast. 30 slices were acquired starting above the renal veins and extending down to the union of the two common iliac veins (Figure 1.9). Imaging parameters included matrix size=448x448, acquired spatial resolution=100x100x500 μm, TR/TE=27.4/8.2 ms, flip angle=30°, TI=450 ms, and 2 signal averages. In addition, T1 mapping of thrombus and blood before and after contrast injection were performed using a Look-Locker based sequence (76). T1 maps from 30 slices were calculated using custom-made software implemented in Matlab (Mathworks, Natick, MA, USA). T1 mapping imaging parameters included: acquired spatial resolution 200x200 μm, slice thickness of 500 μm, TR/TE=9.0/4.6 ms and flip angle=10°.

Image Analysis

We calculated the visualised thrombus volume enhancement in the pre and post contrast images. On LGE-IR images, thrombus was defined as intravascular pixels with signal intensities greater than 2 standard deviations of the mean blood signal measured in normal vessel segments. On T1 maps thrombus size was estimated as intraluminal pixels with a T1 value lower than the measured blood T1 relaxation time in normal vessel segments minus two standard deviations.

Histology and ICP analysis

All thrombi were harvested immediately after the post contrast imaging session. Abdominal laparotomy was performed to allow visualisation of the whole abdominal IVC and to measure the distance from the renal branches until the union of the two common iliac veins. The IVC was harvested en-bloc, including the thrombus and the IVC extending from the renal branches down to the union of the two iliac veins. The harvested IVC was then pinned onto cork mats and stretched to the same length as measured *in-situ* prior to harvest. The tissue was stored in 10% formalin for 24 hours before being embedded in wax. Paraffin sections (5 μm) of the entire IVC were taken at 500 μm intervals to allow comparison with the corresponding MRI slices. Sections were stained with haematoxylin and eosin (H&E) for anatomical detail and Martius Scarlet Blue (MSB) trichrome stain for visualisation and quantification of fibrin and collagen.

Digital images of MSB-stained sections were captured using a light microscope (Leitz, Leica, UK) and a microscope-mounted camera (EXi Blue, QImaging) and processed using image analysis software ImageJ (National Institutes of Health, Bethesda, MD, USA) and the colour-

threshold tool to estimate the percentage of fibrin and collagen content in the intravascular region of the IVC in each histological slice.

Inductively coupled mass spectroscopy (ICP-MS) for gadolinium concentration quantification was performed on a subset of thrombi (N=). Thrombus was digested in 70% nitric acid at 37°C overnight followed by dilution with deionized water for ICP-MS analysis. A standard curve was run with each sample set for Gd concentration determination.

Statistical Analysis

Continuous data are expressed as mean ± 1 SD and the paired t-test was used to compare pre and post contrast parameters in the same group of mice. Measures of agreement were calculated using linear regression analysis and Bland-Altman plots. All statistical analysis was done using SPSS Statistics software package release 19.0 (IBM Corporation, Somers, NY, USA). A P-value of <0.05 was considered statistically significant.

3.3 Results

Thrombi were successfully induced in all mice. High signal intensity on pre contrast IR images and short T1 relaxation times on T1 maps were observed in the central (core), but not in the outer parts (distal) of thrombus at days 4, 7 and 10 (Figure 3.2). This is presumably related to the formation of methemoglobin in the core of the thrombus as was shown in Section 2.6.

Following injection of EP-2104R, higher signal intensity and shorter T1 relaxation times were observed both in the thrombus core and in the distal portion of the thrombus compared with pre contrast images. This was most evident at days 2, 4, 7 and 10 following thrombus induction (Figures 3.2 and 3.3).

The mean T1 relaxation time in the thrombus core shortened both on pre and post EP-2104R images during the course of thrombus organisation up to day 10, reaching 734 and 489 ms respectively (Figure 3.2). In the distal segment, the T1 relaxation time pre contrast did not show a significant change during thrombus organisation, while the post EP-2104R T1 relaxation times showed a similar trend as the thrombus core, with a minimum T1 relaxation time of 498 ms between day 7 and 10. In the pre contrast images the average T1 relaxation time of blood was 1478 ± 86 ms, while in post EP-2104R images the average T1 relaxation time two hours after

contrast injection was 1280 ± 58 ms suggesting almost complete contrast agent clearance. No T1 relaxation time shortening of thrombus was observed in post Gadolinium-DTPA injection images (Figure 3.3).

Average whole thrombus T1 relaxation time pre and post EP-2104R injection showed significant shortening at day 2, 4, 7, 10 and 14, but not significant difference at day 21 (Figure 3.4). These results are consistent with the visualized fibrin by histology at day 2, 4, 7, 10 and 14, and the no fibrin content at day 21 (Figure 3.3). These new areas of contrast uptake lead to a larger visualised thrombus volume in the post EP-2104R images compared with the non-contrast images (Figure 3.5). No significant difference in the thrombus volume estimated by T1 maps was found at day 2 and 21 in the pre and post contrast images. However, significant differences were found at day 4, 7, 10 and 14, consistent with the large fibrin thrombus content at those time points of thrombus organisation.

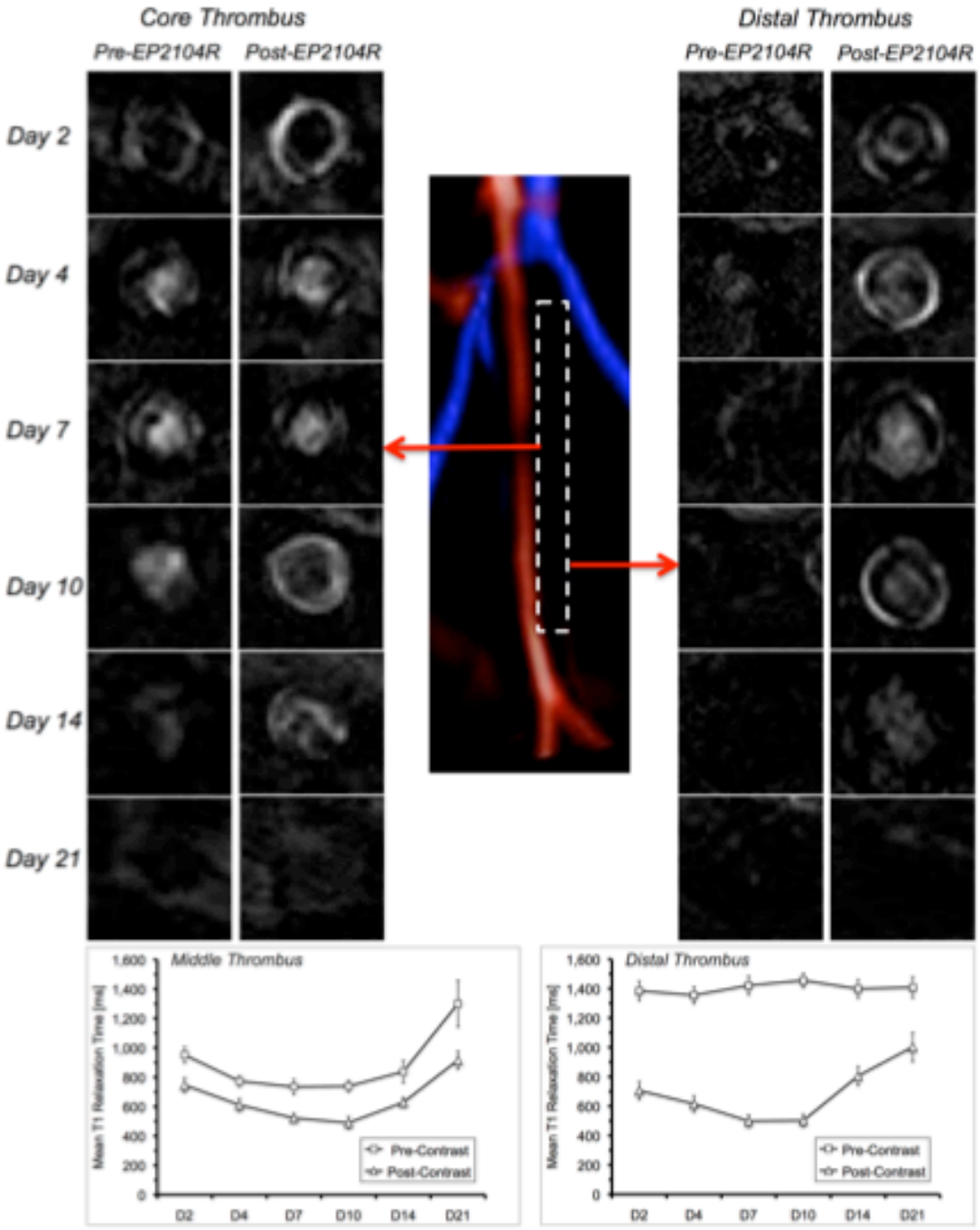

Figure 3.2- Late gadolinium enhancement inversion recovery (LGE-FSMRI) images pre- and 2 hours post-injection of EP-2104R of the middle and distal segments of thrombus at different time points post thrombus induction. High signal intensity in the LGE-IR images and low T1 relaxation times on T1 maps can be observed in the pre-contrast images of the thrombus at the middle segment between day 4 and 10 while no such effect was observed in the distal segments of the thrombus. This is due to the formation of methemoglobin in the core of the thrombus as was shown in Section 2.6. Post EP-2104R injection, contrast agent accumulation can be observed in the periphery of thrombus at day 2 both in mid and distal segments. From day 4 until day 10 increasing contrast uptake can be observed both in the mid and distal segments of thrombus and decrease of contrast uptake between day 14 to 21. The graphs show the thrombus T1 relaxation time pre and post contrast at different time points in the mid and distal segments of the thrombus. FSMRI: fibrin specific MRI.

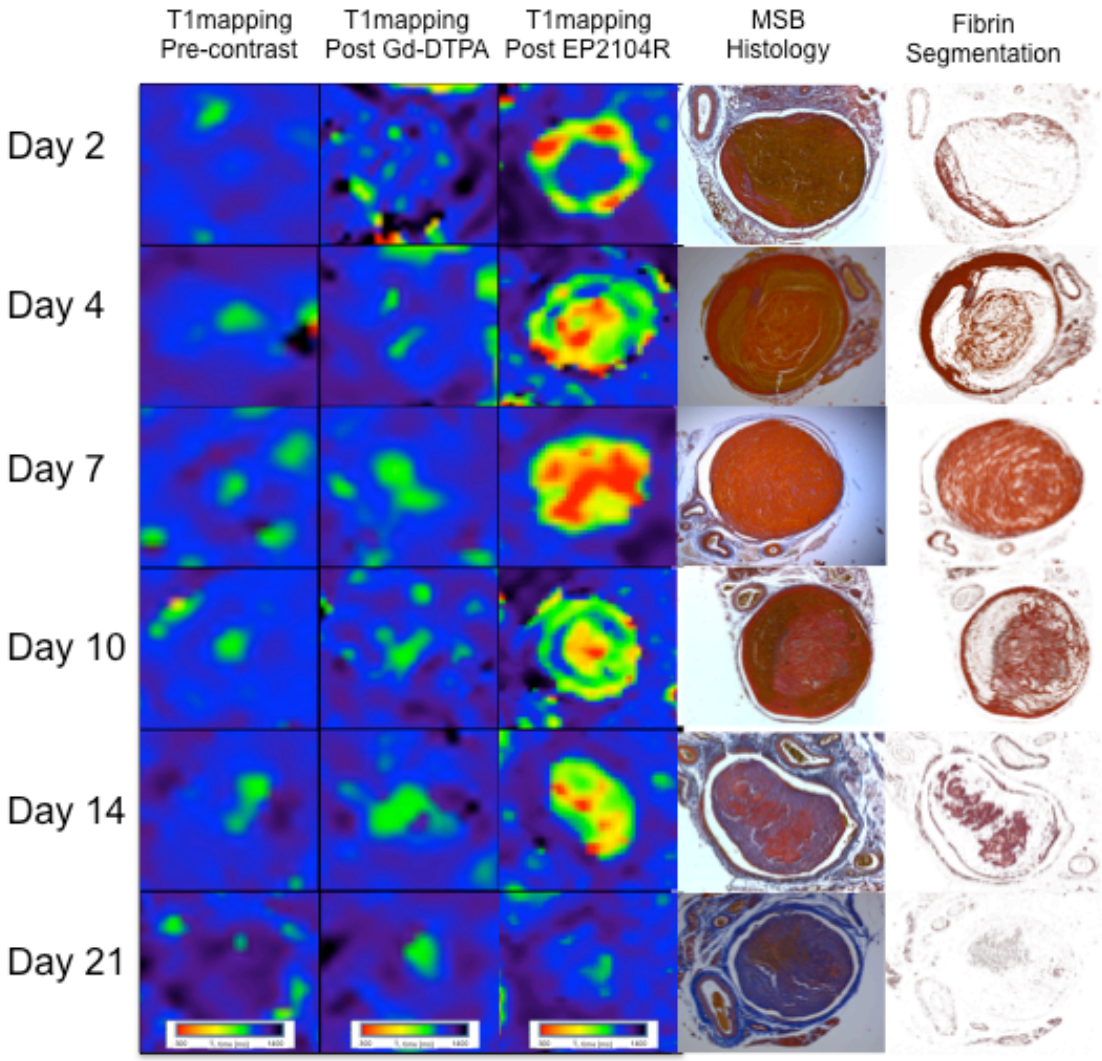

Figure 3.3- T1maps images pre contrast and post injection of Gd-DTPA and EP-2104R at the distal segment of the thrombus (brighter signal represents lower T1 relaxation times). MSB histology sections and fibrin segmentation using ImageJ software (NIH, Bethesda, USA) at the corresponding levels.

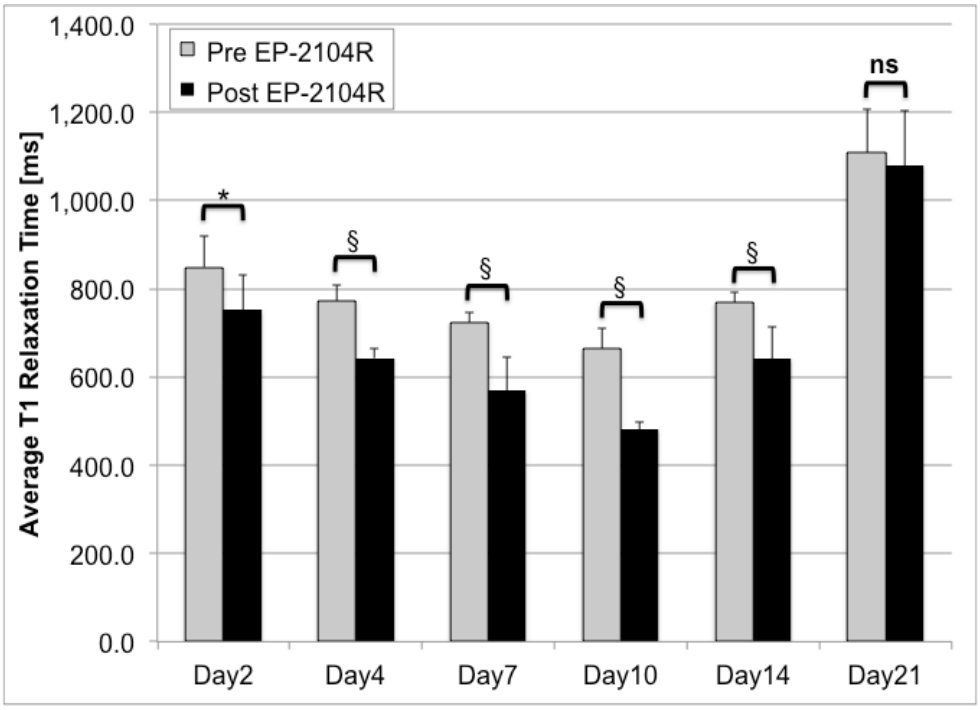

Figure 3.4- Average Thrombus T1 relaxation times at different time point pre and post EP-2104R injection. The maximum differences were reached at Day 4, 7 and 10 (Paired t-test, *=P<0.05, &=P<0.01, §=P<0.001, ns: non significant)

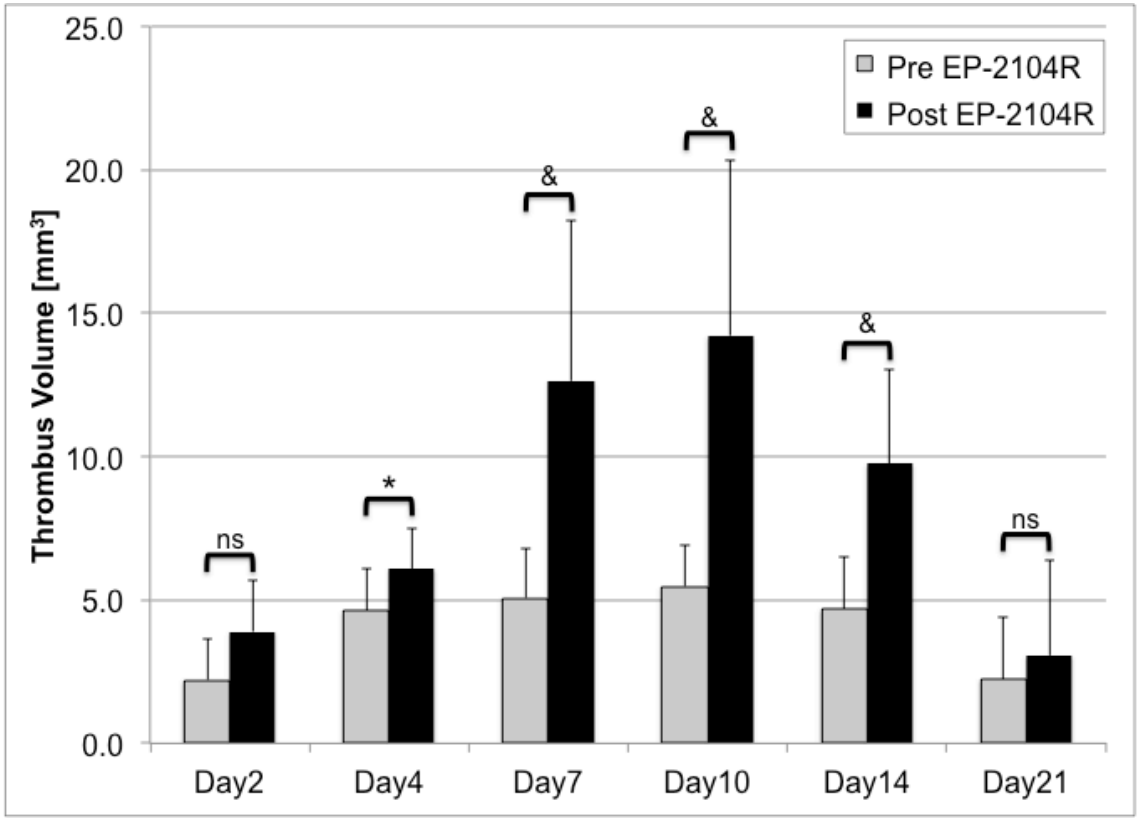

Figure 3.5- Average Thrombus volume estimate by the T1maps, at different time point pre and post EP-2104R injection. The maximum differences were reached at Day 7 and 10 (Paired t-test, *=P<0.05, &=P<0.01, §=P<0.001, ns: non significant)

Good spatial correspondence between T1 mapping images of EP-2104R uptake and fibrin distribution on MSB stained sections was observed (Figure 3.3). Fibrin rich areas in the thrombus were detected between 2 and 14 days following thrombus induction, reaching a maximum content of 79% of the cross sectional area of thrombus at day 10 (Figure 3.6a). After this time point, a decrease in fibrin content and an increase in collagen content were observed (Figure 3.6a).

The mean gadolinium concentration in thrombus of mice injected with EP-2104R showed a strong correlation with the T1 relaxation time (R^2=0.944, P<0.01, Figure 3.6b) measured by T1 mapping. This relationship was similar with the percentage of fibrin content in thrombus estimated by histology (R^2=0.912, P<0.01, Figure 3.6c). Good agreement (R^2=0.978 and 0.966, P<0.01) and no significant bias was found in the Bland-Altman analysis between the percentage of thrombus fibrin content estimated from post EP-2104R T1 mapping and LGE-FSMRI images compared with histology (figures 3.6e-f). Traces of gadolinium (less than 10 μM) were detected in the thrombus post injection of Gd-DTPA, but with no correlation with the average T1 relaxation time at any time point (Figure 3.6b).

Following thrombus induction different patterns of EP-2104R uptake were observed. At day 2, when thrombus is histologically less organized, and consisting largely of trapped red cells, EP-2104R enhancement was observed in the periphery of the thrombus (Figure 3.2 and 3.3). Between day 4 and 10 as fibrin content increased histologically and gadolinium concentration increased accordingly in the thrombus resulting in high signal intensity on LGE-FSMRI images and short T1 relaxation times (Figure 3.2 and 3.3). Between day 10 and 14, thrombus was more organised with processes of vein recanalization and deposition of collagen replacing the fibrin matrix (Figure 3.3 and 3.6a). These changes were associated with decreased EP-2104R uptake as observed as low signal intensity areas on LGE-FSMRI images and an increase in the T1 relaxation time on T1maps of the thrombus (Figures 3.2 and 3.3). By day 21, thrombus was primarily composed of collagen, with a variable rate of IVC lumen occlusion. Thrombi were difficult to visualise with or without injection of EP-2104R (Figure 3.2 and 3.3).

Representative T1mapping images pre and post EP-2104R injection are shown for thrombus with low (Figure 3.7a) and high (Figure 3.7b) contrast uptake at the proximal, mid and distal thrombus level. Both thrombi appear similar on pre contrast images showing low T1 relaxation

time in their core section and no clear thrombus delineation in the proximal and distal sections. However the area of contrast uptake post EP-2104R injection was significantly different, showing that they were at different stages of thrombus organisation. This figure shows the great potential of EP-2104R in the venous thrombosis diseases.

Figure 3.8a shows the relation between the thrombus T1 relaxation time pre contrast and the absolute decrease in the thrombus T1 value post contrast. In a very narrow range of pre-contrast T1 values there is a different uptake of EP-2104R, showing that the contrast uptake could be a better discriminator of thrombus stage of organisation.

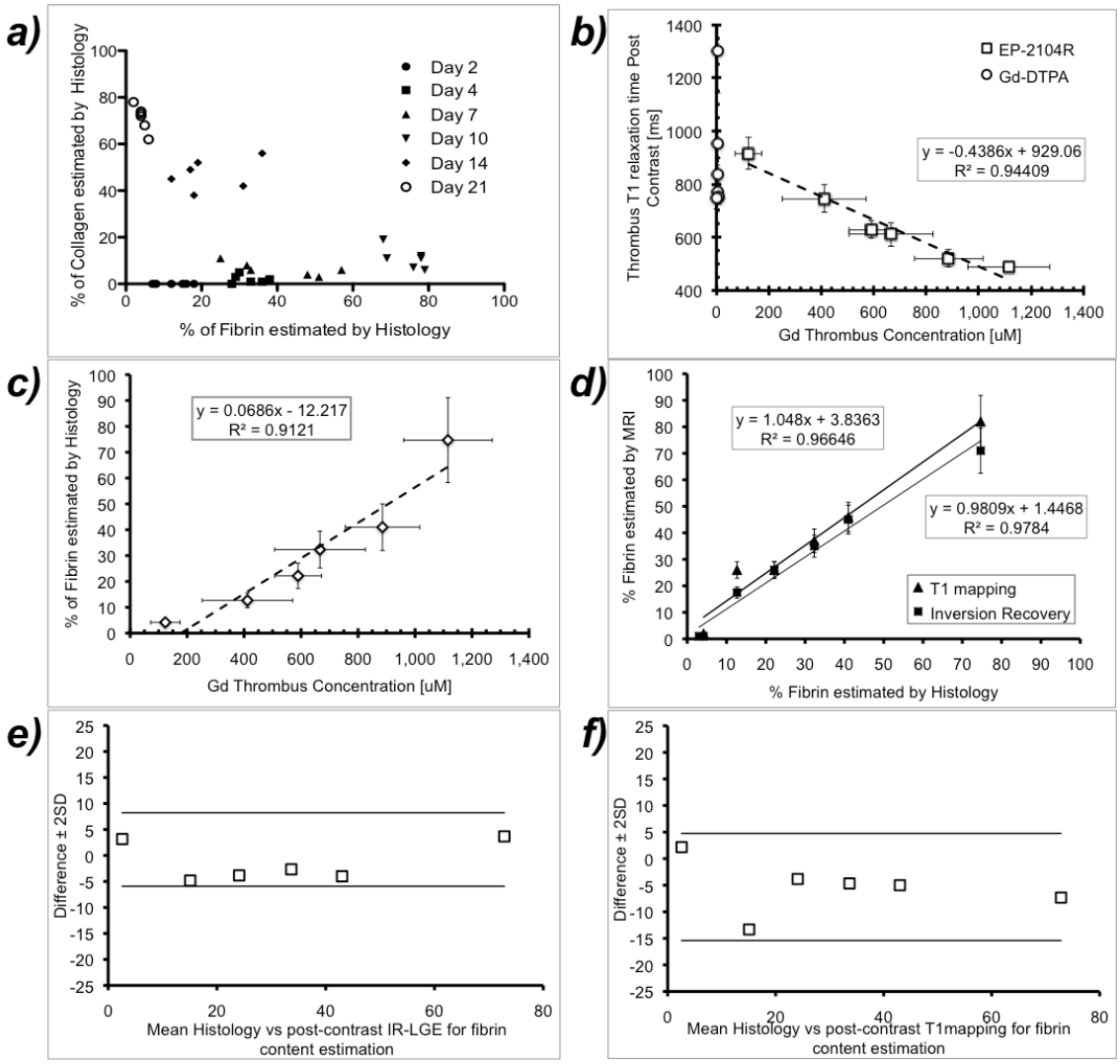

Figure 3.6- a) Fibrin and collagen thrombus content (%) at different time points estimated from the MSB histology sections. (b-c) Average gadolinium thrombus concentration estimated by ICP-MS at each time point showing a good correlation between the average thrombus T1 relaxation time and the thrombus fibrin content. d) Correlation between percentage of fibrin content in thrombus estimated by post-contrast T1mapping and LGE-FSMRI images compared to histological estimation. (e-f) Bland Altman analysis showing no significant bias in the estimation of the thrombus fibrin content at different time points using post contrast T1 mapping and LGE-FSMRI images compared to histology. FSMRI: fibrin specific MRI.

The relation between the absolute decrease in the thrombus T1 relaxation time post contrast and the increase in the enhanced thrombus volume in the T1mapping due of the contrast uptake define two thrombi subpopulation (Figure 3.8b). The first one are thrombi with a small decrease in the T1 relaxation time post contrast and a small increase of the thrombus enhanced volume (Day 2, 4 and 21); and a second sub-population with a larger decrease in the T1 relaxation time and a large increase in the thrombus enhanced volume (Day 7, 10 and 14) indicating a high fibrin content.

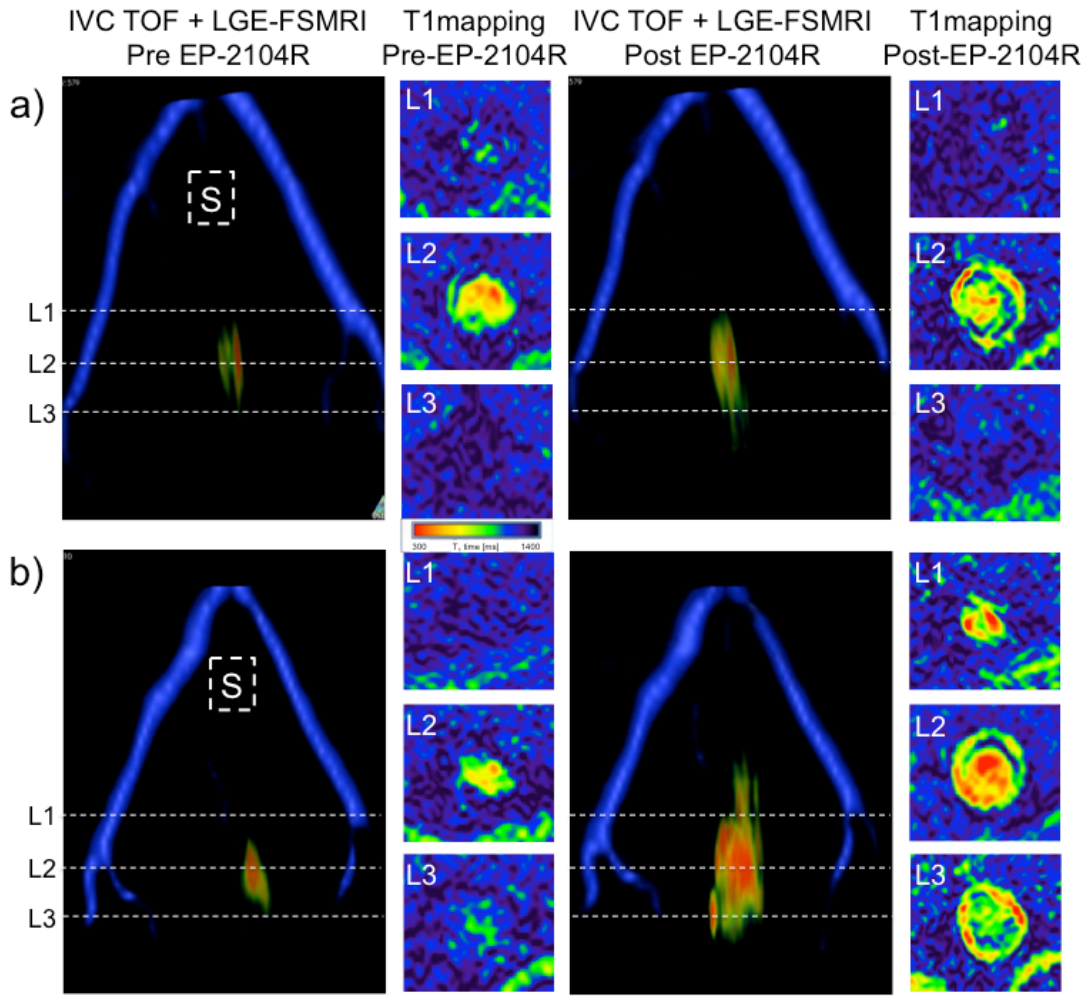

Figure 3.7- Representative reconstruction of the Inversion Recovery images pre and post EP-2104R injection for thrombus with (a) low and (b) high EP-2104R contrast uptake. T1 maps at three levels area also shown. Pre-contrast images looks similar, however post-contrast images show different stages of thrombus organisation

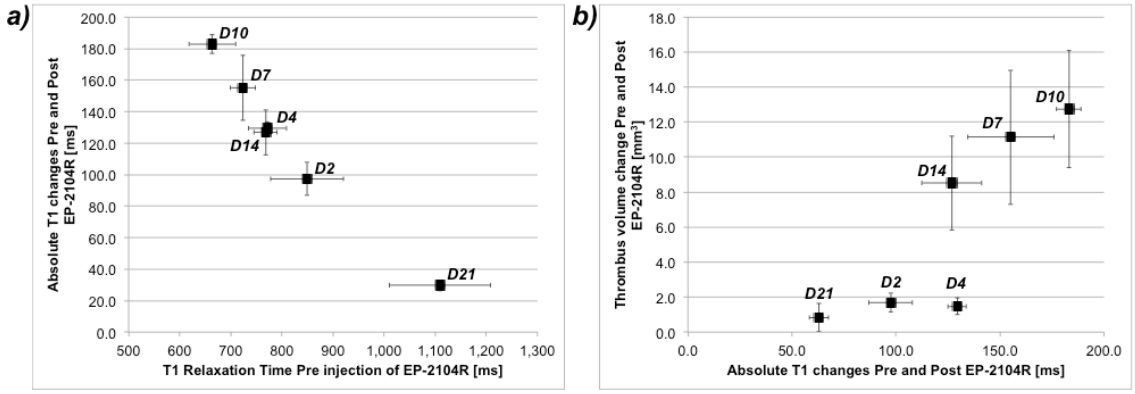

Figure 3.8- (a) Average thrombus T1 relaxation time and absolute T1 decrease post EP-2104R injection at each time point of thrombus organisation. (b) Average thrombus T1 relaxation time and increase in thrombus visualisation volume pre and post contrast at each time point of thrombus organisation.

3.4 Discussion

We have demonstrated that quantification of fibrin in a mouse model of DVT using a fibrin binding MRI contrast agent, EP-2104R, provides accurate information on the fibrin content in venous thrombus. The absolute decrease in thrombus T1 relaxation time post contrast and the change in the visualized thrombus enhanced volume pre and post contrast were very well correlated with the histologically measured fibrin content and could provide useful information on the stage of thrombus organisation.

The information given by EP-2104R contrast uptake provides useful information at the molecular level and could be used to identify thrombi suitable for thrombolysis as later shown in Chapter 5.

Chapter 4 Venous thrombus characterization using a super-paramagnetic very small citrate-coated iron oxide particle (VSOP)

4.1 Aims and objectives

Venous thrombus resolves by a process of organization and recanalization that is similar to the formation of granulation tissue in healing wounds. The recruitment of inflammatory cells is an important component of both processes. An initial neutrophil infiltrate is replaced by monocyte-derived macrophages that have the capacity to express a host of chemotactic agents, proteases, and growth factors that orchestrate tissue remodelling and thrombus organisation (43,47,48,50,52). Several studies have shown that lack of infiltration of these cells impairs or delays normal thrombus organisation (47,51). Therefore, monocyte and macrophage accumulation within the thrombus is a hallmark of thrombus organisation in both man and experimental models (55,96,97).

The use of ultrasmall superparamagnetic iron oxide nanoparticles (USPIO) as a molecular marker for inflammation is well known due to its rapid uptake by the mononuclear phagocyte system (98). Such imaging agents, mostly sterically stabilized by dextran coating, have been used for more than a decade to study inflammatory changes in atherosclerotic vessels in animal models (99) and humans (100,101) as well as in inflammation and cancer (102). More recently, very small iron oxide particles (VSOP) have been introduced with a hydrodynamic diameter much smaller (~7 nm) than of USPIOs (~30 nm). These particles are stabilized electrostatically by complex binding of citrate to the iron particle surface. This technique allows obtaining a monocrystalline iron oxide particle with a diameter of 7 nm, which is smaller than the currently available dextran coated iron oxide nanoparticles (60,103). VSOP is mainly cleared via the phagocytic system, and for this reason, is an excellent contrast agent for targeting macrophages (59).

In this chapter sought to study the uptake of VSOP by macrophages during thrombus organisation. Our objective was to study if there is a correlation between thrombus VSOP uptake and the stage of thrombus organisation.

4.2 Materials and Methods

4.2.1 DVT mouse model

Venous thrombosis was induced in the inferior vena cava (IVC) of 8-10 weeks old male BALB/C mice as was described in section 1.5.1. MRI was performed at day 2, 4, 7, 10, 14 and 21 following thrombus inductions. Eight mice were scanned at each time point pre and 48 hours post injection of a VSOP-C184 (Figure 4.1).

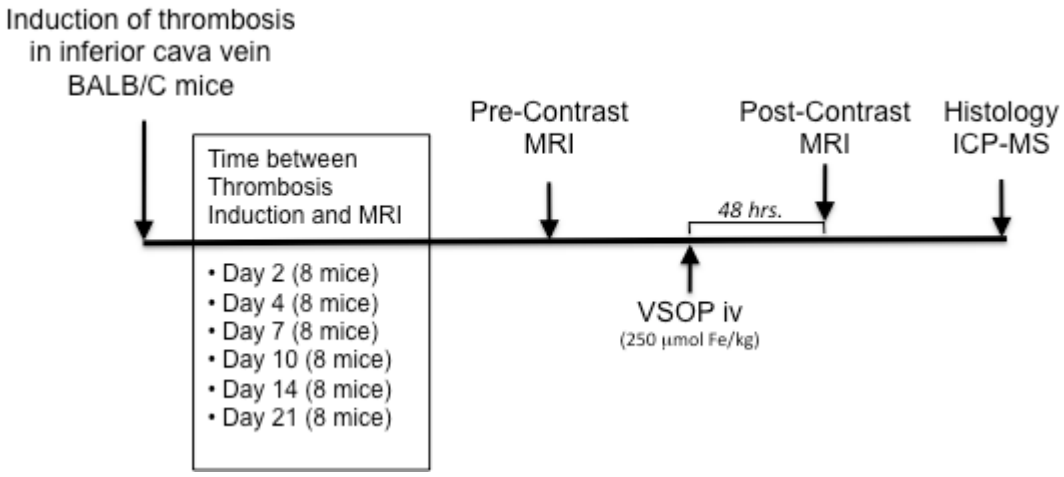

Figure 4.1- Study design. Eight mice were scanned at each time point (day 2, 4, 7, 10, 14 and 21) after IVC thrombosis induction. Mice were scanned pre and post VSOP injection. Each venous thrombus was harvested and analysed using ICP-MS for Fe uptake quantification and histology

Iron oxide nanoparticle

For macrophage detection, VSOP-C184 (Charité, Berlin, Germany) was used (59,101-103). The contrast agent consists of an aqueous solution of super-paramagnetic iron oxide particles coated with a citrate layer. The concentration of the active substance is 27.9 gFe/L, corresponding to 0.5 molFe/L. The particles have a core diameter of 4 nm and a hydrodynamic diameter of 7 nm. The relaxivities of VSOP-C184 are R1=20.1 $(mmol*s)^{-1}$ and R2=37.1 $(mmol*s)^{-1}$ (59). The contrast agent was administered by tail vein injection and a dose of 250 μmol of iron per kg was administered 48 hours before the scan (99).

MRI Protocol

Mice were anesthetized with 1.5-2% isofluorane and 100% oxygen delivered through a nose cone and scanned in prone position on a 3T Philips Achieva Gyroscan MR scanner (Philips Healthcare, Best, The Netherlands) equipped with a dedicated 47 mm small animal surface coil.

A 3D T2* multi-echo gradient echo sequence was used to reconstruct T2* maps from 30 slices pre and 48 hours post VSOP injection, as was previously described in section 2.4.2.

Image Analysis

T2* maps from 30 slices were obtained using a custom-made software application written in Matlab (Mathworks, Natick, MA, USA) which fit pixel-by-pixel the T2* equation decay (Eq. 2.1) and calculated the average T2* value in a region of interest (Section 2.4.2) pre and post injection of VSOP.

Circulating monocytes, histology and ICP analysis

All thrombi were harvested immediately after the post contrast imaging session. Abdominal laparotomy was performed to allow visualisation of the whole abdominal IVC and to measure the distance from the renal branches until the union of the two common iliac veins. 1 ml of blood was obtained using a cardiac puncture technique. Blood was then put through an automated cell counter (Sysmex, Japan) for quantification if circulating monocytes. The IVC was harvested en-bloc, including the thrombus and the IVC extending from the renal branches down to the union of the two iliac veins. The harvested IVC was then pinned onto cork mats and stretched to the same length as measured *in-situ* prior to harvest. The tissue was stored in 10% formalin for 24 hours before being embedded in wax. Paraffin sections (5 μm) of the entire IVC were taken at 500 μm intervals to allow comparison with the corresponding MRI slices. Thrombus sections were stained with haematoxylin and eosin (H&E) for anatomical detail, Perls' Blue to identify hemosiderin and iron particle deposition (section 2.2.2) and MAC-2 (Accurate Chemical, NY, US) for macrophage visualization.

Sham operations were carried out in another group of mice, in which all steps of the thrombosis procedure were carried out except tying of the suture across the IVC. Blood samples were obtained in 3 mice at day 2, 7, 14 and 21 days after sham procedure for quantification of circulating blood monocytes.

Inductively coupled mass spectroscopy (ICP-MS) for iron concentration quantification was performed on a subset of thrombi (N=4 at each time point). Thrombus was digested in 70% nitric acid at 37 °C overnight followed by dilution with deionized water for ICP-MS analysis. A standard curve was run with each sample set for Fe concentration determination.

Statistical Analysis

Continuous data are expressed as mean ± 1 SD and the paired t-test was used to compare pre and post contrast parameters in the same group of mice. Measures of agreement were calculated using linear regression analysis and Bland-Altman plots. All statistical analysis was done using SPSS Statistics software package release 19.0 (IBM Corporation, Somers, NY, USA). A P-value of < 0.05 was considered statistically significant.

4.3 Results

Circulating monocyte numbers increased following induction of venous thrombosis compared to sham controls, showing no statistical difference at day 2, but significant differences at day 7, 14 and 21 (Figure 4.2). This result is consistent with monocytosis described in patients with DVT (104).

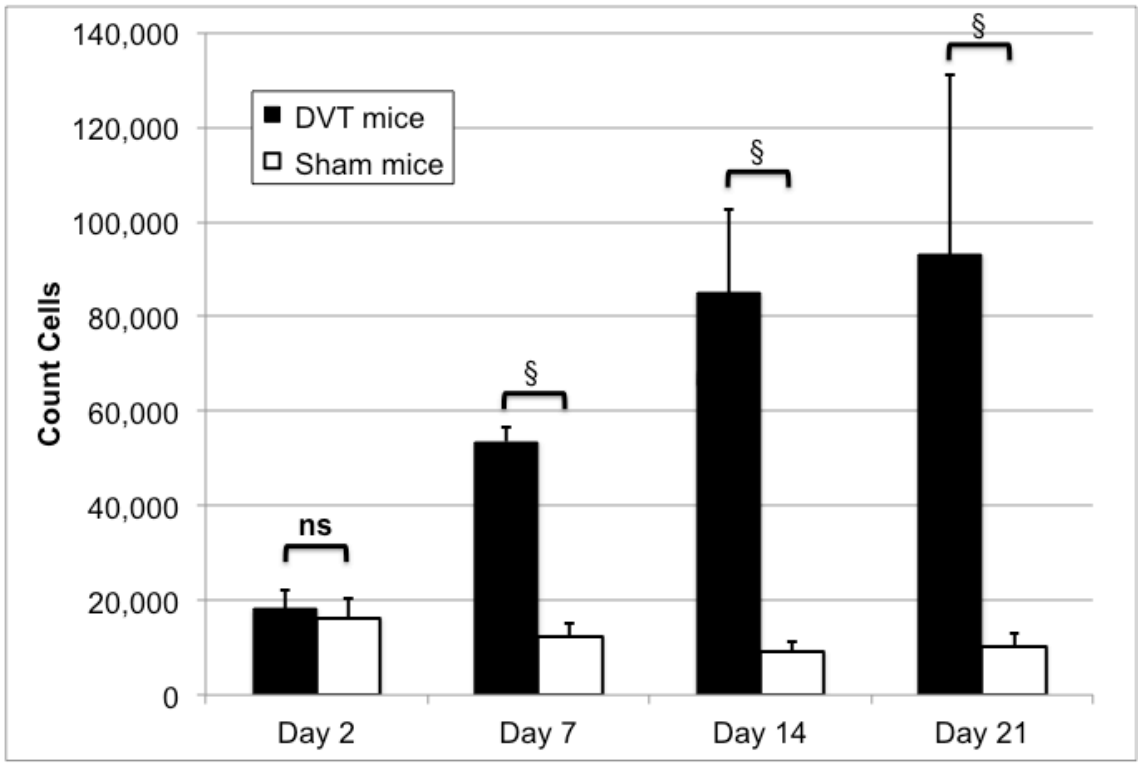

Figure 4.2- Circulating numbers of monocytes following venous thrombosis. (*=P<0.05, &=P<0.01, §=P<0.001, ns: non significant)

Iron-oxide nanoparticles shorten the T2* relaxation time of tissues in their vicinity and appear as a signal void on gradient echo MR images. This contrast is often referred to as “negative contrast”. Figure 4.3 shows the T2* maps of a thrombus pre and post VSOP contrast injection at different time points. As thrombus typically contains red cells and thus there is a physiological iron concentration in thrombus, which produces a baseline T2* effect, as was discussed in section 2.4. Differences in the T2* effect between pre and post contrast images thus should result from VSOP uptake by macrophages, which infiltrate the thrombus during organisation and resolution (Figure 4.3).

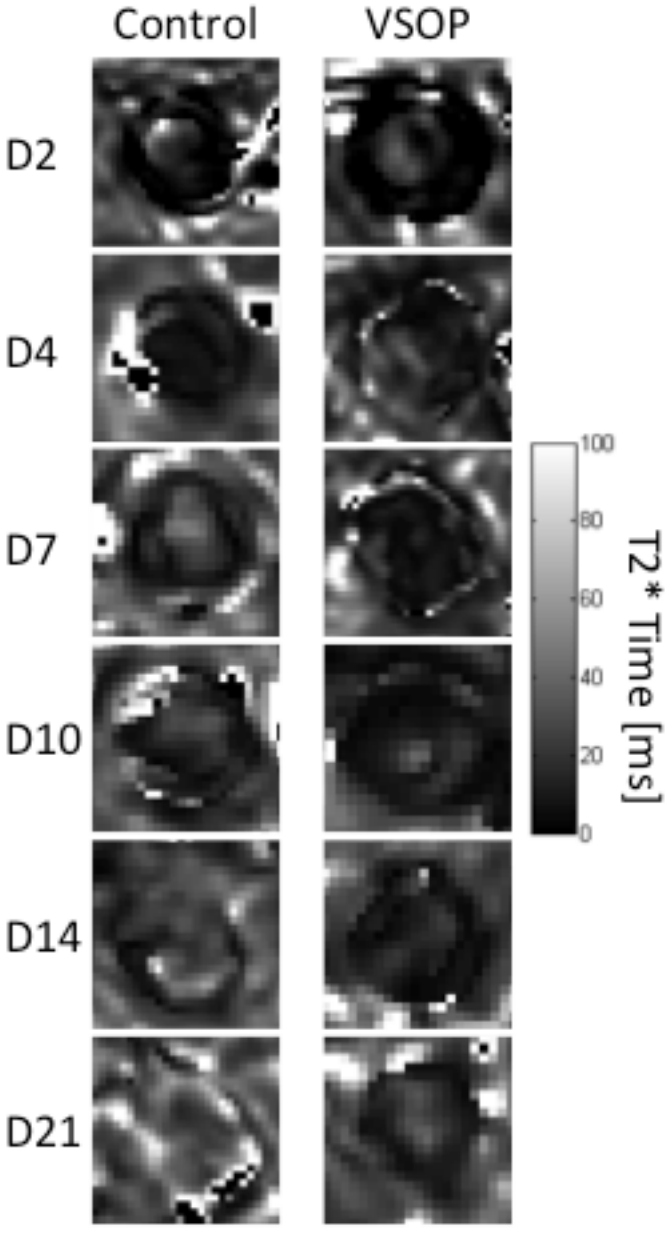

Figure 4.3- T2* mapping of venous thrombus at different time points during thrombus organisation. Darker areas represent shorter T2* times. The T2* differences pre and post VSOP were associated with macrophage infiltration and subsequent VSOP uptake

Figure 4.4 shows the average T2* value of the thrombus pre and post VSOP injection. There was no statistical difference in the T2* relaxation time pre and post VSOP injection at days 2 and 4. From day 7 on the T2* value was significantly lower in the post contrast images. In young thrombi, the T2* effect mainly originates from haemoglobin of trapped RBCs. At this stage macrophage infiltration is small and therefore the contribution of VSOP uptake to T2* shortening is minimal, which is in concordance with the lack of significant differences in the total iron content in very young thrombus pre and post VSOP injection (Figure 4.5a).

From day 7 on the concentration of trapped RBCs decreases and therefore the total iron concentration in thrombus pre VSOP injection is reduced and the T2* value increased (Figures 4.4 and 4.5a). On the other hand, infiltration of macrophages increases rapidly starting at day 7, which is consistent with the significant decrease of the T2* value and the increased difference in the average iron content between pre (section 2.4.3, Figure 2.9) and post VSOP injection at each time point (Figure 4.4, 4.5a and 4.6). The T2* relaxation times in thrombus post VSOP injection showed a good correlation with the total iron content, which includes the endogenous (trapped RBCs) and the exogenous iron (phagocytised VSOP by macrophages) (Figure 4.5b). There was good co-localization between the macrophage distribution on MAC2 stained images and the iron distribution on the Perls' stained histological slices (Figure 4.6b).

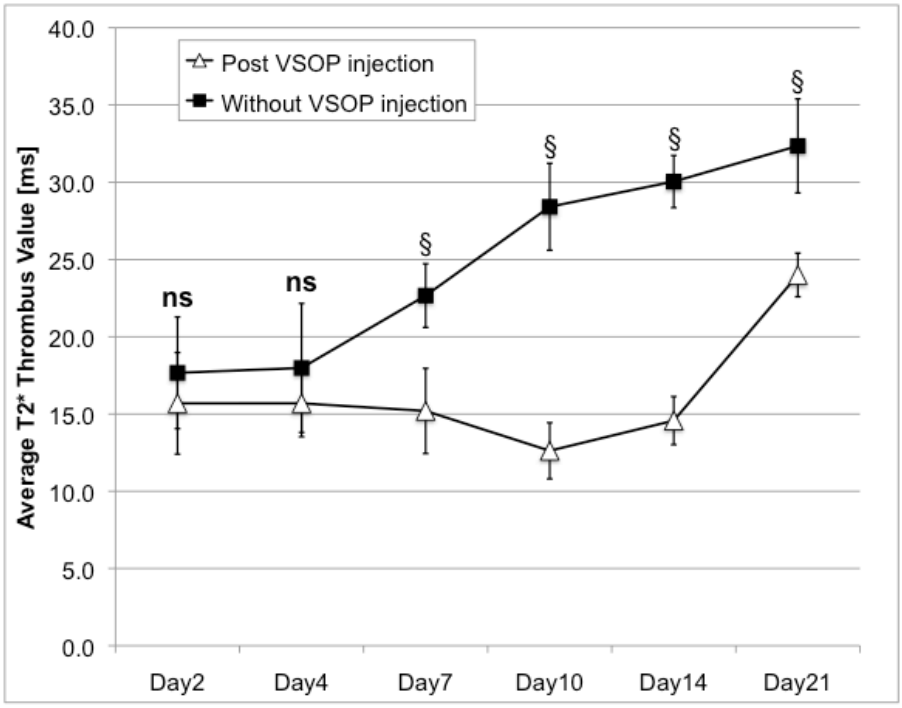

Figure 4.4- Average thrombus T2* times [ms] at different time points of thrombus organisation pre and post VSOP injection.

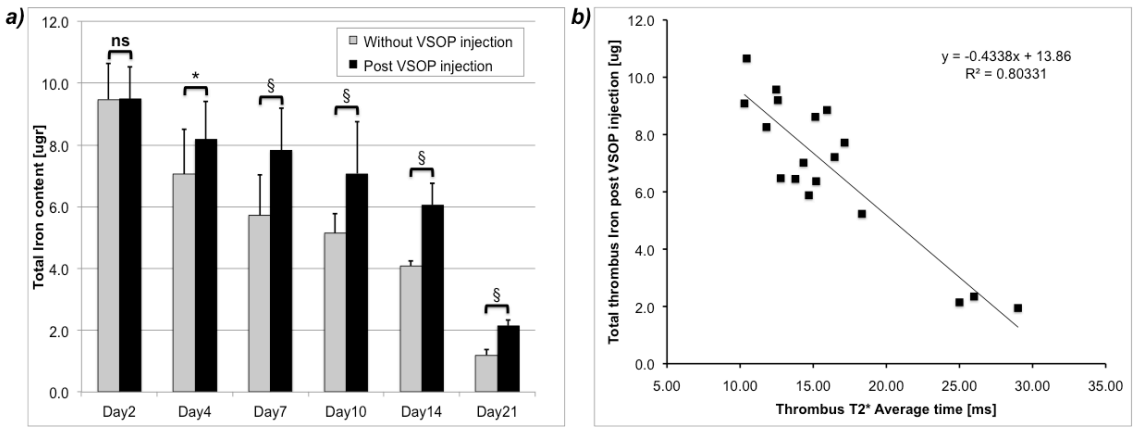

Figure 4.5- Average total iron thrombus content [μgr] pre and post VSOP injection. An almost linear relationship between the total iron content [μg] and average T2* relaxation time was found at different time points of thrombus organization

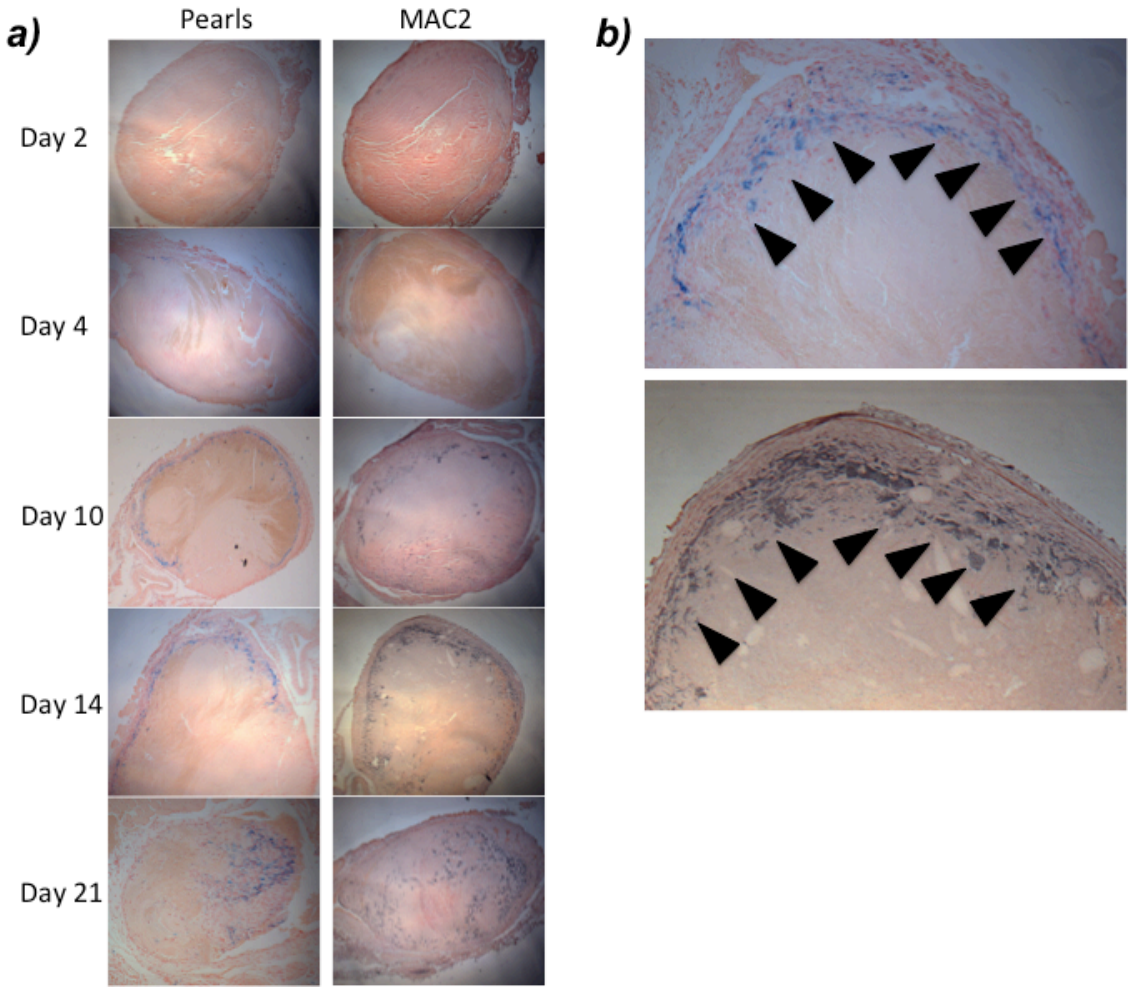

Figure 4.6- (a) Pearl's and MAC2 stained histological sections of thrombus at different time points post thrombus induction showing an increase in macrophage infiltration and VSOP uptake during thrombus organisation. (b) Excellent co-localization between the macrophage distributions on MAC2 stained sections and the iron distribution on the Perls' stained histological slices.

Figure 4.7 shows the absolute difference in the T2* values [ms] (a) and the total iron content [μg] (b) in the thrombus pre and post VSOP injection at different time points during thrombus organisation. In very young thrombus there was neither a significant difference in delta T2* nor in delta total iron content. In older thrombus we observed a decrease in RBC content and an increase of macrophage infiltration resulting in a higher difference in T2* relaxation time values and iron concentration pre and post VSOP injection.

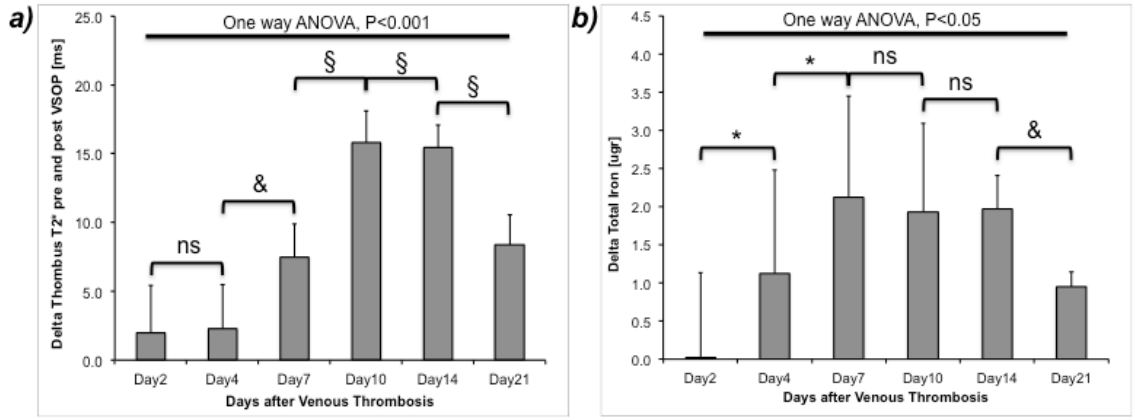

Figure 4.7- Absolute difference in average (a) T2* values [ms] and (b) total iron content [mg] in the thrombus pre and post VSOP injection at different time point during thrombus organisation. (*=P<0.05, &=P<0.01, §=P<0.001, ns: non significant)

There was no clear relationship between the T2* value pre contrast and post VSOP injection (Figure 4.8a). However, thrombi at different time points are clearly clustered. Thrombi with higher fibrin content and therefore higher chance of successful outcome post thrombolytic therapy are highlighted in figures 4.8a and 4.8b.

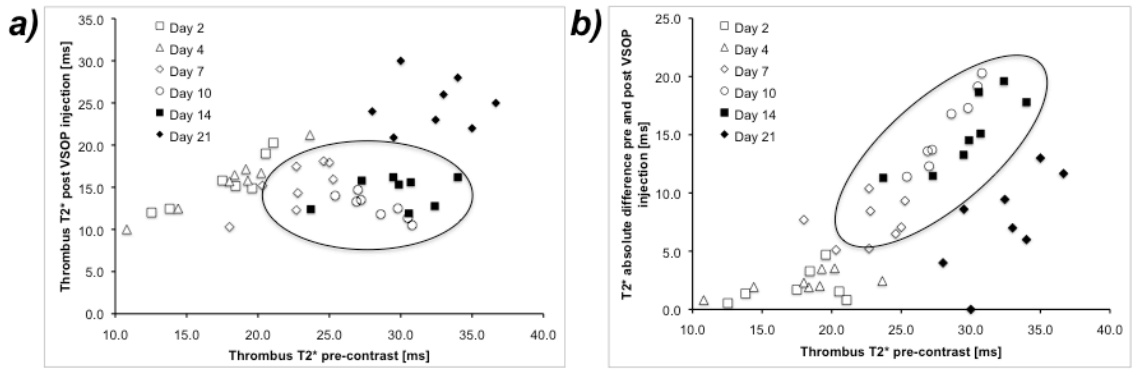

Figure 4.8- Relationship between Thrombus T2* time pre-contrast [ms] and (a) its T2* time [ms] post VSOP injection and (b) the absolute difference between pre and post T2* times [ms]. Highlighted points show thrombus with higher fibrin content, and therefore higher chance of successful thrombolysis.

The relationship between the T2* relaxation time [ms] pre contrast and the absolute decrease in the T2* value post VSOP injection and the difference in the thrombus iron content pre (section 2.4.3, Figure 2.9) and post contrast show a parabolic behaviour (Figure 4.9). In younger thrombus we observed short T2* relaxation times pre VSOP, low VSOP uptake and small differences in T2* relaxation time post injection. Those findings are due to the high thrombus RBC content and the lack of macrophage infiltration. In contrast, older thrombus showed the longer T2* relaxation times pre VSOP injection (because of the lack of RBCs) and moderate VSOP uptake. Thrombus at the intermediate organisation stage showed the highest uptake of VSOP and therefore the highest difference between T2* and iron content pre and post VSOP injection (Figure 4.9).

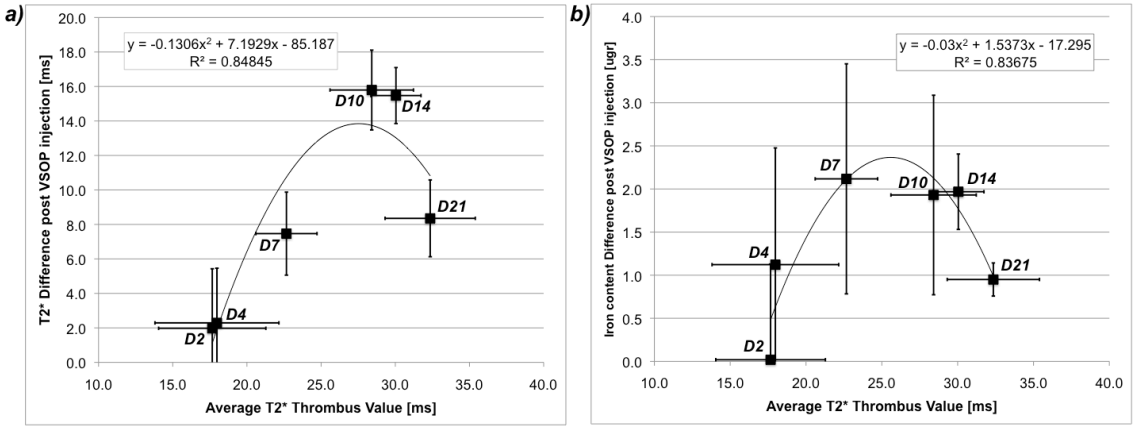

Figure 4.9- Average thrombus T2* times [ms] before contrast and absolute difference in average (a) T2* values [ms] and (b) total iron content [mg] in the thrombus pre and post VSOP injection at different time point during thrombus organisation. (*=P<0.05, &=P<0.01, §=P<0.001, ns: non significant)

4.4 Discussion

Iron nanoparticles have a great potential to detect tissues with macrophage infiltration (102,105,106). Macrophage infiltration plays a major role during thrombus organisation and therefore its detection and quantification could improve the diagnosis of DVT and help to identify the stage of thrombus organisation (43,51,54). In this section we have shown that iron uptake is related with stage of thrombus organisation, however due to the presence of endogenous iron in RBCs it was difficult to differentiate between iron related to RBCs and VSOP.

Even though iron nanoparticles have shown good potential to identify inflamed tissue (107,108) its use in venous thrombosis was found to be more challenging. Iron quantification using T2*

mapping only shows the total amount of iron (endogenous and exogenous) and does not allow to differentiate between these two iron populations. More studies are thus needed to identify the best protocol to differentiate between both pools of iron, and therefore to obtain accurate measures of macrophage infiltration in venous thrombus.

Chapter 5 Use of MRI for the identification of thrombus amenable for thrombolysis

5.1 Aims and objectives

In the previous Chapters we have shown that several MRI sequences can successful identify thrombus composition and allow differentiation between young and old thrombus. Additionally the use of a fibrin specific contrast agent can accurately quantify the total fibrin content of venous thrombus and therefore it is a very promising methodology to identify thrombi amenable for thrombolysis.

In this Chapter we therefore sought to investigate whether of the previous studied sequences would allow identify thrombi that are susceptible for thrombolysis.

The most promising sequences studied were: T2* mapping, T1 mapping, MTC, and fibrin specific MRI (FSMRI). In this chapter we used the mouse model of DVT and mice were scanned pre and post systemic thrombolytic treatment, which allowed identifying those parameters that allowed successful prediction of outcome.

5.2 Materials and Methods

DVT mouse model

Venous thrombosis was induced in the inferior vena cava (IVC) of 8-10 weeks old male BALB/C mice as was described in section 1.5.1. MRI and thrombolytic treatment were performed at day 2, 4, 7, 10, 14 and 21 following thrombus inductions. Six mice were scanned at each time point pre and 2 hours post injection of a gadolinium based, fibrin-specific MRI contrast agent, EP-2104R (EPIX Pharmaceuticals, Lexington, MA) (56,57,93,94). Immediately after the last scanning session, systemic thrombolysis was carried out by a 5 minutes tail vein infusion of 10 mg/kg of tissue plasminogen activator (Actilyse, Boehringer Ingelheim, Germany). 24 hours after thrombolysis, mice were scanned again 2 hours post EP-2104R injection (Figure 5.1).

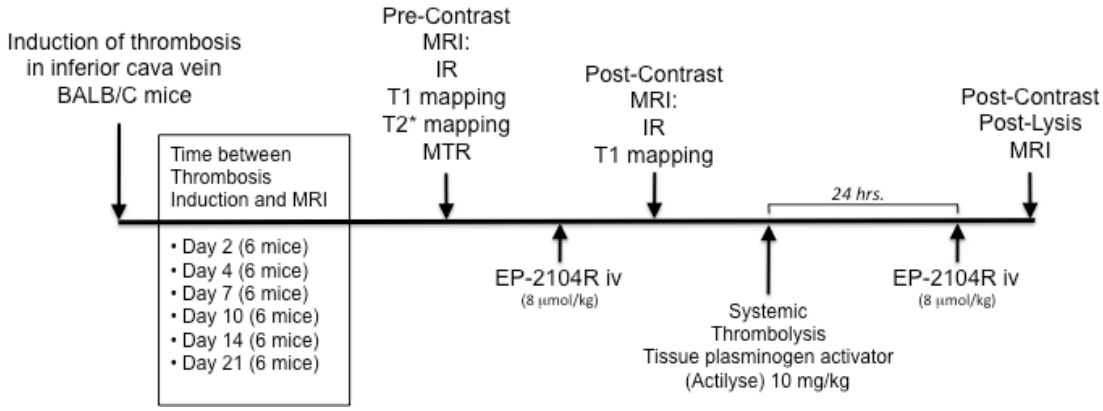

Figure 5.1- Study design. Six mice were scanned at each time point (day 2, 4, 7, 10, 14 and 21) after IVC thrombosis induction Pre and Post EP-2104R injection, and post systemic thrombolysis.

MRI Protocol

Mice were anesthetized with 1.5-2% isofluorane and 100% oxygen delivered through a nose cone and scanned in prone position on a 3T Philips Achieva Gyroscan MR scanner (Philips Healthcare, Best, The Netherlands) equipped with a dedicated 47 mm small animal surface coil. A late gadolinium enhancement inversion recovery (LGE-IR) 3D segmented gradient echo (TFE) sequence was performed to selectively visualise thrombus pre and post contrast. 30 slices were acquired starting above the renal veins and extending down to the union of the two common iliac veins (Figure 1.9). Imaging parameters included matrix size=448x448, acquired spatial resolution=100x100x500 μm, TR/TE=27.4/8.2 ms, flip angle=30°, TI=450 ms, and 2 signal averages. In addition, T1 mapping of thrombus and blood before and after contrast injection were performed using the same protocol described in section 2.6.2.

A 3D T2* multi-echo gradient echo sequence was used to calculate T2* maps from 30 slices as was previously described in section 2.4.2.

The magnetization transfer rate (MTR) was obtained from dynamic T1FFE 3D images acquired without and with an on-resonance MT pre-pulse as described in section 2.5.2.

A phase contrast sequence was performed to measure blood flow in the infrarenal IVC pre and post thrombolysis in order to evaluate the success of the thrombolytic therapy as described in section 1.6.

Image Analysis

We calculated the average T2* relaxation time and MTR in each thrombus as well as the average T1 relaxation time pre and post EP-2104R injection, using the same methodology described in section 2.4, 2.5 and 2.6 respectively.

We also calculated the visualised thrombus volume enhancement in the pre and post contrast images. On LGE-IR images, thrombus was defined as intravascular pixels with signal intensities greater than 2 standard deviations of the mean blood signal measured in normal vessel segments. On T1 maps thrombus size was estimated as intraluminal pixels with a T1 value lower than the measured blood T1 relaxation time in normal vessel segments minus two standard deviations.

Phase contrast images were used to estimate blood flow in the IVC pre and 24 hours post thrombolytic therapy. Thrombolysis was considered successful if an increase in IVC blood flow greater than 50% was observed on 24 hours post lysis scans.

5.3 Results

Three mice died during thrombolytic therapy because of haemorrhage. The mean IVC flow in normal mice measured by MRI was: 0.55 ± 0.05 [ml/min]. There was a mean increase of IVC blood flow of 0.174 ± 0.06 [ml/min] (158% ± 86% with respect to pre-lysis IVC flow) following successful thrombolysis. In the unsuccessful thrombolysis group the mean increase in IVC flow was 0.002 ± 0.006 [ml/min] (1% ± 7% with respect to pre-lysis IVC flow) (Figure 5.2).

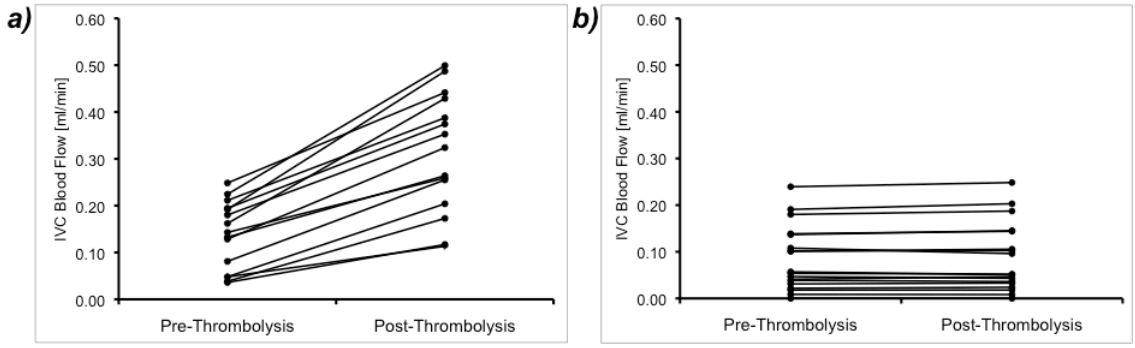

Figure 5.2- IVC blood flows measured by phase contrast MRI pre and post thrombolytic treatment in the (a) successful thrombolysis group and (b) the unsuccessfully treated group.

Non-contrast MRI

Figure 5.3 shows the thrombus average T1 relaxation time, T2* relaxation time and MTR for successfully and unsuccessfully lysed thrombi. T1 relaxation time was found to be a good predictor of thrombolysis outcome and a T1 of 750–800 ms was found to be a good threshold to differentiate between the successful and unsuccessful lysis (Figure 5.3a).

As discussed in section 2.4.4, most of the unsuccessfully lysed thrombi had a short T2* relaxation time (less than 20 ms) or long T2* relaxation time (longer than 32 ms) (Figure 5.3b). In the first case the thrombi were found to be very young and full of RBCs, which is in agreement with the lytic resistance of the fibrin matrix surrounded by RBCs (66,86). In the second case, very old thrombus was identified which has no to little RBCs and therefore a long T2* value. The main component of these thrombi was collagen, which is not suitable for classic thrombolytic therapy.

MTR values showed a less obvious trend. However, thrombi with higher MTR values were more resistant to lytic therapy (Figure 5.3c).

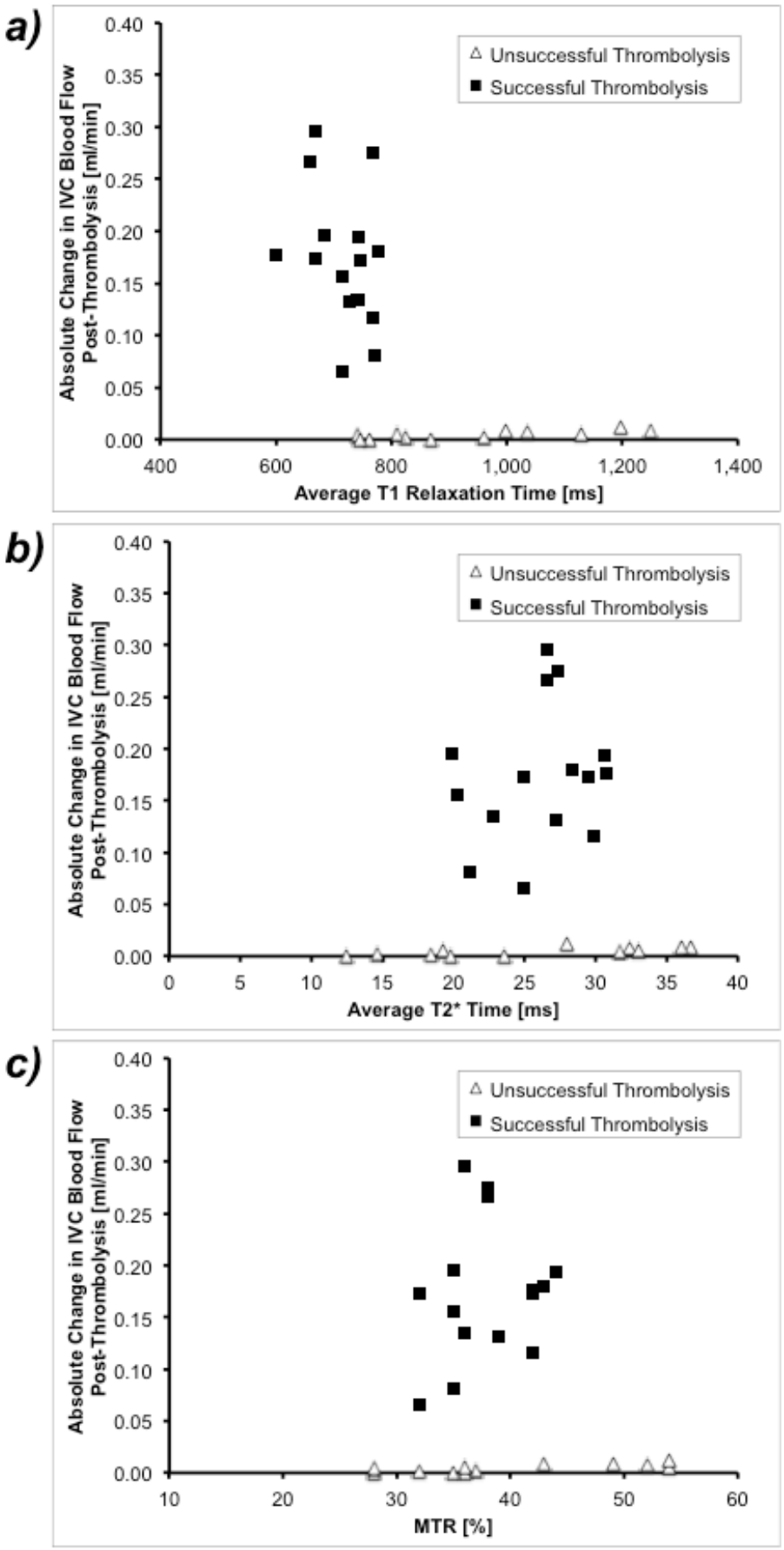

Figure 5.3-. Average T1 relaxation time (a), T2* relaxation time (b) and MTR (c) for successfully (black squares) and unsuccessfully (white triangles) lysed thrombi.

Figure 5.4 shows the relationship between T1 and T2* relaxation time as well as MTR for the successfully and unsuccessfully treated groups. The clustering of successfully lysed thrombi at lower T1 relaxation times shows that the average thrombus T1 relaxation time would be the best non-contrast enhanced predictor for thrombolytic outcome.

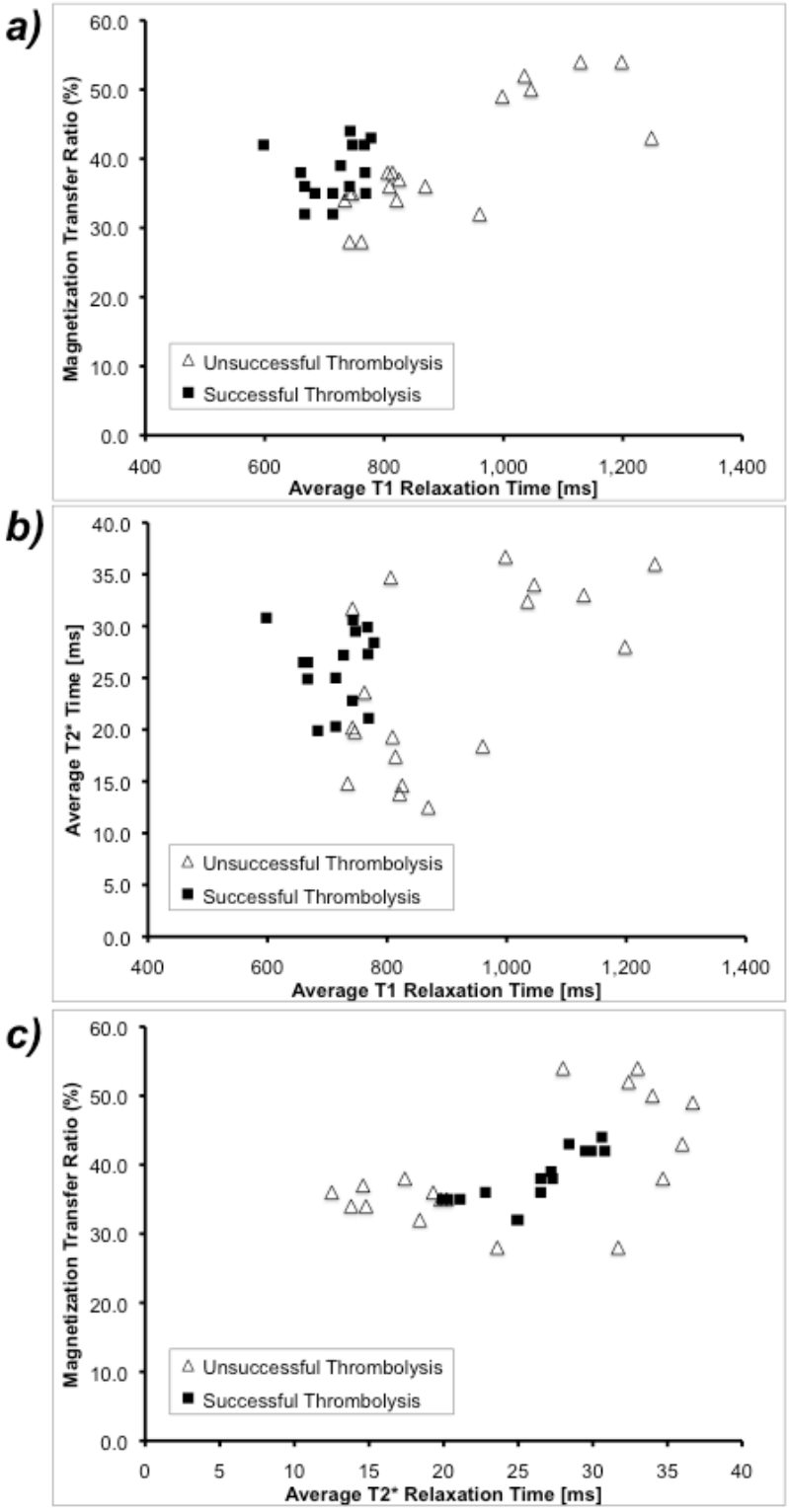

Figure 5.4- Relationship between T1 relaxation time, T2* relaxation time, and MTR for successfully (black squares) and unsuccessfully (white triangles) lysed thrombi

Fibrin contrast agent

Figure 5.5 shows the enhanced thrombus volume estimated from the T1 mapping images from the 33 treated mice at three stages of treatment: pre thrombolysis pre contrast agent injection, pre thrombolysis post EP-2104R injection, and post thrombolysis post EP-2104R injection. In the successful thrombolysis group the mean increase in the visualised thrombus volume pre and post EP-2104R before treatment was higher than in the unsuccessful thrombolysis group (11.75 ± 5.3 mm^3 (239% ± 124%) vs. 1.46 ± 1.21 mm^3 (41% ± 31%), P<0.001)). Twenty-four hours after thrombolytic therapy a decrease in the visualised enhanced thrombus volume was observed. The mean difference in the visualised enhanced thrombus volume pre and post thrombolysis was larger in the successful group (6.35 ± 2.8 mm^3 (-38% ± 15%) compared to unsuccessful group (0.65 ± 1.20 mm^3 (-12% ± 18%), P<0.001) (Figure 5.5).

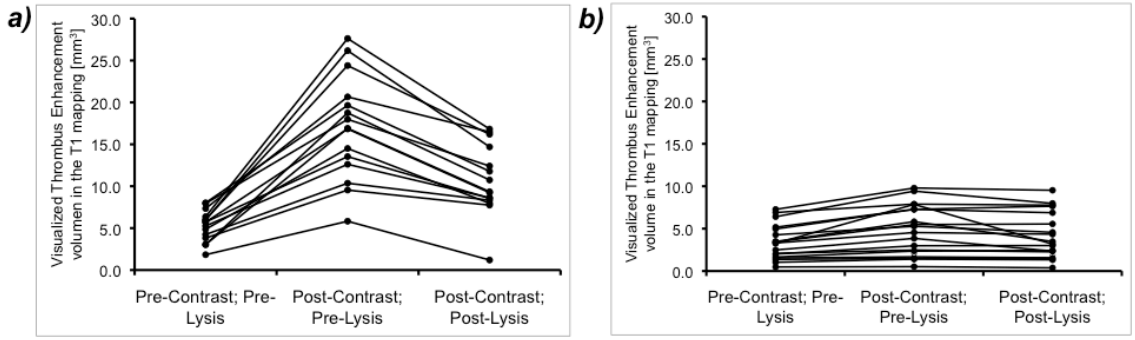

Figure 5.5- Visualized thrombus enhanced volume [mm^3] estimated from pre and post contrast T1 mapping images. Visualized enhanced thrombus volume before thrombolytic therapy increased significantly after EP-2104R injection in the successfully lysed animals (a) while there was little change in the unsuccessfully treated animals (b). After treatment a significant decrease in the visualized enhanced thrombus volume was observed in the successfully lysed groups but not in the unsuccessful group.

Representative T1mapping images pre and post EP-2104R injection before thrombolytic treatment are shown for successfully and unsuccessfully lysed thrombus at the proximal, mid and distal thrombus level (Figure 5.6). Successfully and unsuccessfully lysed thrombus appears similar on pre contrast images showing low T1 relaxation time in the middle section of the thrombus and no clear thrombus delineation in the proximal and distal sections. However the area of contrast uptake post EP-2104R injection was significantly larger for successfully lysed thrombi compared to unsuccessfully lysed thrombus (Figure 5.6).

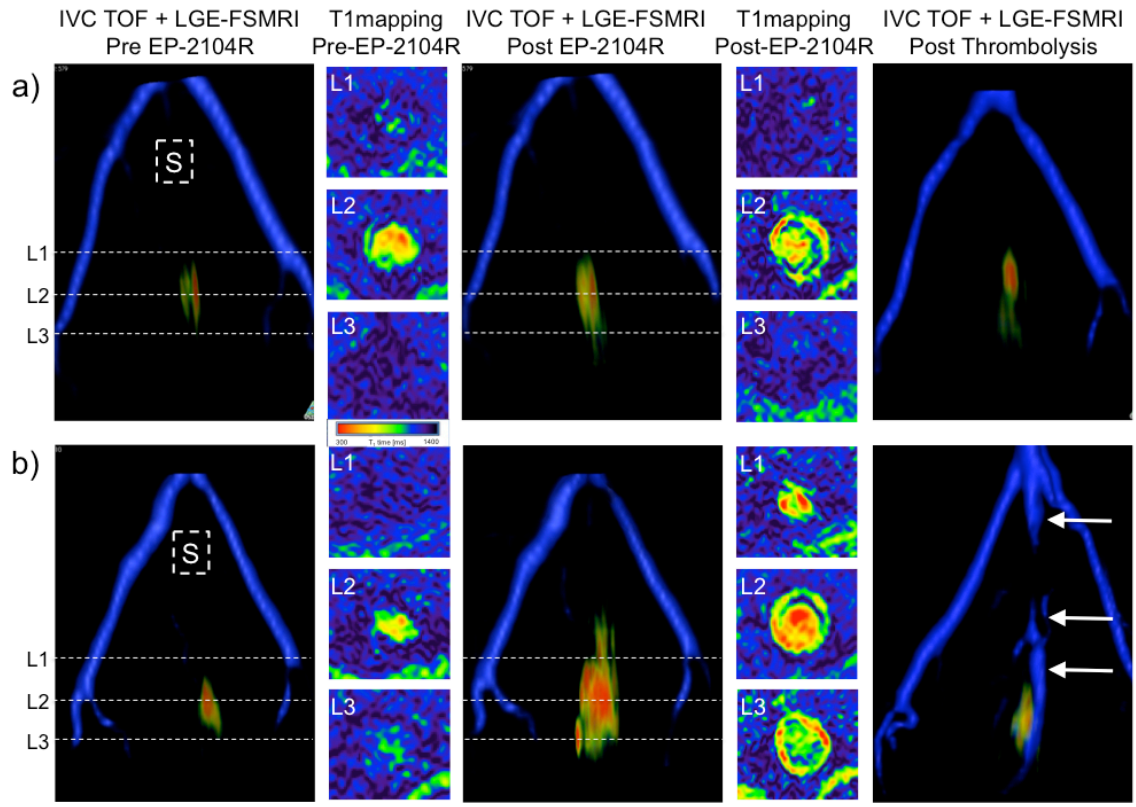

Figure 5.6- Representative images pre and post EP-2104R contrast agent injection for (a) unsuccessfully and (b) successfully lysed thrombus at three levels. Successful thrombolysis was associated with a larger visualized enhanced thrombus post EP-2104R and lower T1 relaxation time on T1mapping, which corresponded to a higher content of fibrin matrix and increased susceptibility to thrombolytic treatment (right). Unsuccessful thrombolysis was associated with little enhancement post EP-210R injection and small fibrin content in the thrombus. Recovery of IVC flow was observed in the successfully lysed cases (arrows). S: stenosis level in the IVC for thrombus formation.

Average T1 relaxation times pre and post EP-2104R, and the change in the visualised enhanced thrombus volume before the treatment are shown in Figure 5.7 for a successfully and unsuccessfully lysed thrombus. Thrombi with larger contrast uptake, represented by a larger decrease in the T1 relaxation time and larger increase of the visualised enhanced thrombus volume on pre and post EP-2104R images before treatment were found to have better lysis results. The larger change in the T1 values and in the visualised enhanced thrombus volume between pre and post EP-2104R is related with a higher fibrin content of the thrombus. Thus, those thrombi contain more “available” targets for the thrombolytic therapy.

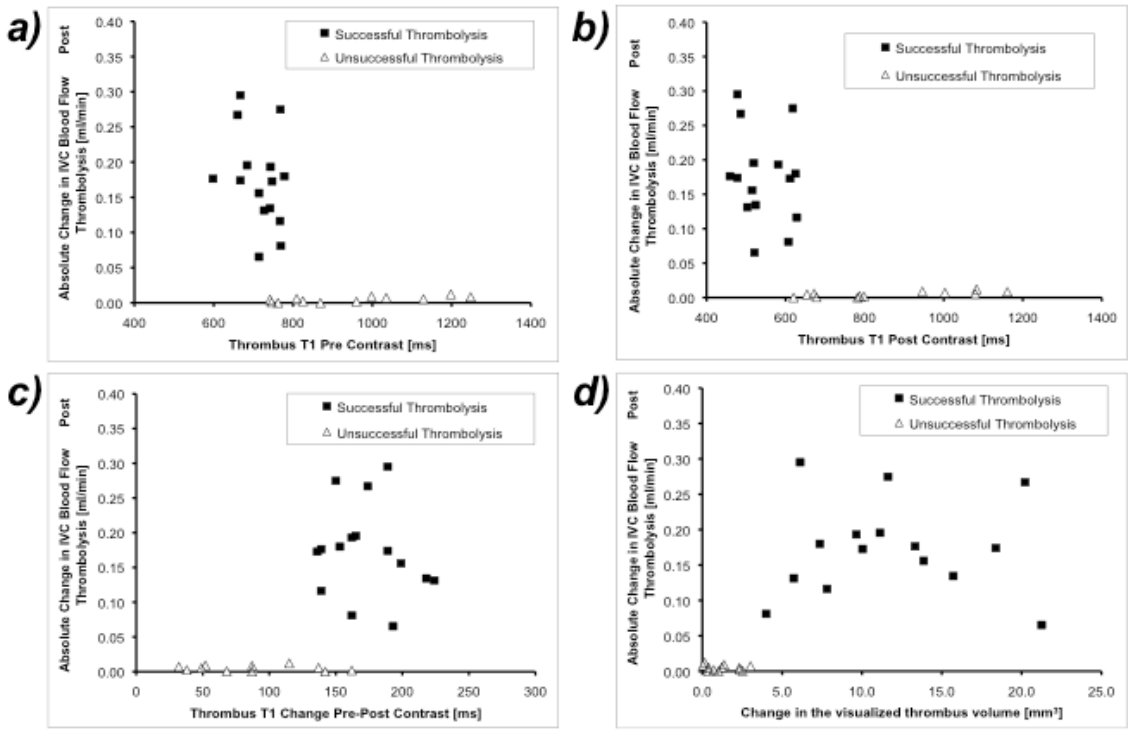

Figure 5.7- Average T1 relaxation time pre and post EP-2104R injection and the change in visualized enhanced thrombus volume pre and post contrast for successfully (black squares) and unsuccessfully (white triangles) lysed thrombi.

ROC analysis

Receiver operator curve (ROC) curve analysis (Figure 5.8) demonstrated that visualised thrombus volume on pre contrast IR MR images was not a good predictor for successful thrombolysis (AUC of 0.748; CI95%: 0.58–0.92) similar to the IVC flow pre lysis (AUC of 0.717; CI95%: 0.54–0.89). Mean T2* thrombus value also did not result in a good predictive value (AUC of 0.556; CI95%: 0.34–0.78). This poor result is mainly because the T2* relaxation time does not have a single cut-off point. Better results were obtained for the mean pre contrast thrombus T1 relaxation time resulting in an AUC of 0.893 (CI95% 0.79–0.99). From the ROC analysis, the optimal cut-off point of pre contrast T1 relaxation time is 774 ms, resulting in a sensitivity of 72% and specificity of 97% to predict successful thrombolysis. If we want to avoid the false positive patients, i.e. patients selected for thrombolysis but with thrombus that will not response to thrombolytic therapy, we should choose a cut-off point that maximizes specificity, and in this case the cut-off point will be 730 ms, resulting in a sensitivity of 53% and specificity of 100% to predict successful thrombolysis. On the other hand, we could choose a cut off point that discards the chance of successful thrombolytic treatment; this cut-off point would be 823

ms, resulting in a sensitivity of 67% and specificity of 100% to predict unsuccessful thrombolysis.

If a cut-off point of T1<774 ms was selected, the probability to identify successful thrombolysis outcome was 82% (CI95%: 68%–95%). If we used a single cut-off point for T2*, like the value suggest by ROC analysis, T2*>19.9 ms, the probability to successfully predict thrombolysis outcome was 55% (CI95%: 37%–72%). However, if we defined two thresholds, 19.9 ms<T2*<32 ms (Figure 5.4b), the probability to predict successful thrombolysis outcome was 79% (CI95%: 65%–93%). If we combined T2* and T1 criteria, the probability to successfully predict thrombolysis outcome increased to 85% (CI95%: 72%–97%). However, the combination of T2* and T1 did not reach statistical difference compared to the use of the T1 relaxation time alone.

Post EP-2104R injection, thrombus images showed much improved sensitivity and specificity for prediction of successful thrombolysis. The visualised enhanced thrombus volume post EP-2104R had an AUC of 0.972 (CI95%: 0.95–1.00) and the difference between the pre and post EP-2104R visualised thrombus enhanced volume before treatment had an AUC of 0.992 (CI95%: 0.98–1.00) (Figure 5.8). The thrombus T1 relaxation time post EP-2104R injection was found to have an AUC of 0.993 (CI95%: 0.98–1.00). A thrombus T1 relaxation time of less than 630 ms on post EP-2104R images had a sensitivity of 94% and specificity of 99% to predict successful thrombolysis. If the increase in the visualised enhanced thrombus volume between pre and post EP-2104R was larger than 3.5 mm^3, the sensitivity and specificity to predict successful lysis was 99% and 95%, respectively.

5.4 Discussion

In spite of the enormous disease burden associated with DVT there is still no consensus on the appropriate management of patients with this condition (1). A lack of “objective” criteria has resulted in most patients who are diagnosed with DVT being treated conservatively, often leading to re-thrombosis and chronic side effects such as PTS (7,10,24). The development of new thrombolytic drugs have stimulated the need for better diagnostic tools that allow identification of patients that are likely to benefit from these therapies while minimizing procedure related complications such as bleeding and intracerebral haemorrhage (13,17).

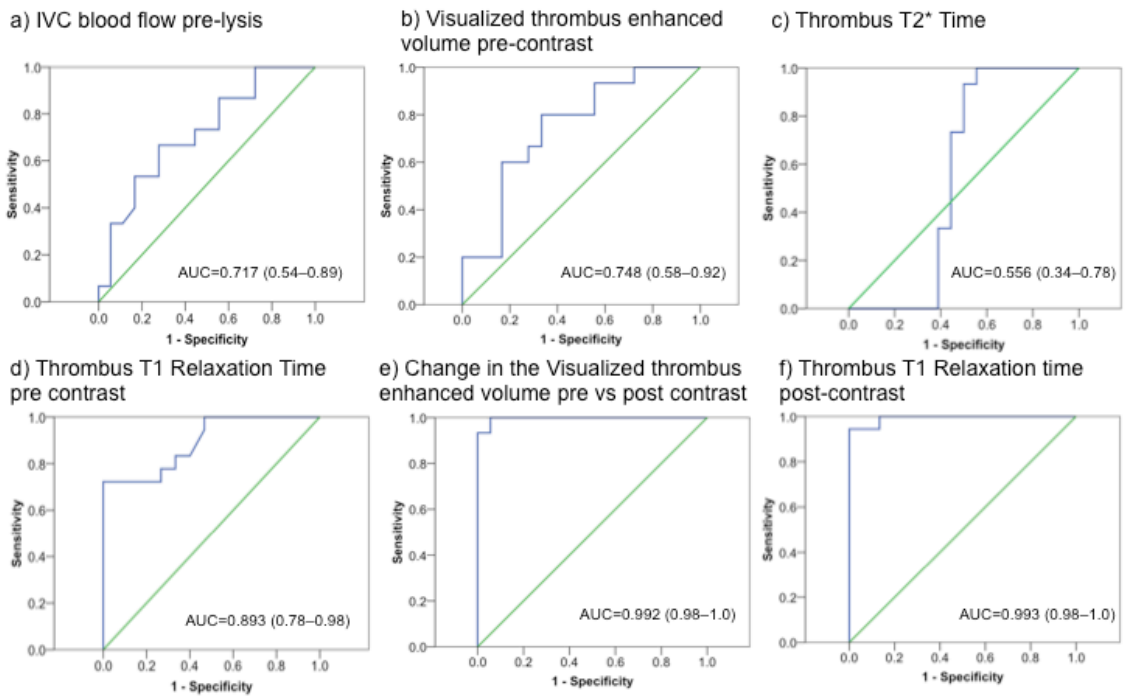

Figure 5.8- ROC curve analysis for the prediction of successful thrombolysis. The best predictors are the change in visualized enhanced thrombus volume pre and post EP-2104R injection and T1 relaxation time post contrast with AUC of 0.992 and 0.993 respectively.

Here we demonstrate that the quantification of fibrin in a mouse model of DVT using a fibrin binding MRI contrast agent, EP-2104R, provides accurate information on the stage of venous thrombus organisation. In addition, it can be used to facilitate the identification of thrombi that are amenable to lysis. The results of this study confirm that EP-2104R not only improves diagnosis of VT by increasing the contrast-to-noise ratio between thrombus and surrounding tissues, as previously shown (58,93,109), but also shows that the molecular information provided could be used to identify thrombi suitable for lysis. The use of this approach may have potential to change current clinical management of patients suffering from DVT by improving the selection criteria of patients scheduled for thrombolytic therapy.

In our model, very acute thrombi (day 2) showed low contrast uptake and this was associated with unsuccessful thrombolysis. Histological analysis showed that these thrombi had a less organized fibrin matrix located in the periphery of the thrombus and thrombus was mainly formed by platelets and red cells (Figure 3.3), which is agreement with the lytic resistance of the fibrin matrix containing red blood cells previously described by Wohner et al (66). Similarly, old thrombus showed little contrast uptake and a low fibrin but high collagen content on histology (Figure 3.3), and those thrombi were not amenable for thrombolysis either.

Furthermore, in this study we have used a constant dose of thrombolytic drugs expressed in mg per kg of mice. However, with the accurate estimation of the thrombus fibrin content, it may allow estimation of a patient specific thrombolytic dose in mg per mm^3 of thrombus' fibrin content. Such patient-specific treatment could further improve the likelihood of successful thrombolysis, and reduce the potentially fatal side effects of an unnecessarily high dose of thrombolytic agent.

Conclusion

We demonstrate that venous thrombus with an evolution time between 7 and 10 days showed the highest rate of successful thrombolysis in an experimental model of DVT while subacute (day 2) and older thrombus (day 21) responded poorly to thrombolytic therapy. As subacute thrombi were typically occlusive, platelet and red cell rich they provided limited access and suitable targets (i.e. fibrin) for current thrombolytic therapy (23,45,48,49,110). Older thrombus was primarily collagen rich and thus not amenable for thrombolytic therapy (45,48,49). This small "window of treatment" was accurately identified on the post EP-2104R images and provides an opportunity to improve staging and treatment of DVT. If these results were confirmed in humans, the use of a fibrin binding contrast agent would have great potential to change clinical assessment and treatment of DVT.

Because EP-2104R has not been yet approved for use in humans, we also showed that the T1 relaxation time of native thrombus could help identifying thrombus amenable for lysis. This methodology can be used on any MRI system used in clinical practice.

Chapter 6 Magnetic Resonance Angiography and Venography without the need of contrast agents

6.1 Introduction

Visualization of the vessel lumen of arteries and veins has proved clinically useful for the diagnosis of many vascular diseases like myocardial ischemia and infarction, stroke, peripheral artery disease, venous thrombosis, and pulmonary embolism, among others.

Traditional angiography techniques require the administration of an iodinated intravascular contrast agent and provide excellent visualization of the vessel lumen either by X-ray or computed tomography (CT). The exposure to radiation and potentially nephrotoxic contrast agents limits their application. Most guidelines suggest avoiding the use of these techniques in children, pregnant women, elderly and patients with renal dysfunction (33-35,111). In addition, the risk of radiation related later complications preclude their use as a screening tool in the general population (112,113).

Non-invasive contrast-enhanced Magnetic Resonance Angiography (CE-MRA) has been shown to be safe and effective and has a very low risk of renal failure after intravenous contrast agent injection (114-118). However there are some concerns of its use in pregnant women and people with renal dysfunction (119). Recent reports on Nephrogenic Systemic Fibrosis (NSF) after gadolinium administration (120) have increased the interest in non-enhanced MR angiography (121,122).

In this work we propose two new techniques for the visualization of arteries and veins without the use of a contrast agent. The first technique is based on the ASL methodology and it is flow dependent, and the second is based on the use of a T2 preparation prepulse and is flow independent.

6.2 Arterial Spin Labelling Angiography using a Triple Inversion Recovery Prepulse (TIR4ASL)

6.2.1 Introduction

Arterial Spin Labelling (ASL) is a well-known angiography technique that does not require the use of contrast agents (61,123). ASL labels the upstream blood using a spatially selective inversion pulse (L) to generate image contrast in a downstream vessel or organ. During a given time delay the tagged blood flows into the area of interest and then can be imaged with an arbitrary imaging sequence. If this process is repeated with enabled (L) and disabled labelling pulses, subtraction of the two datasets will result in a bright-blood angiogram with minimal background signal (Figure 6.1).

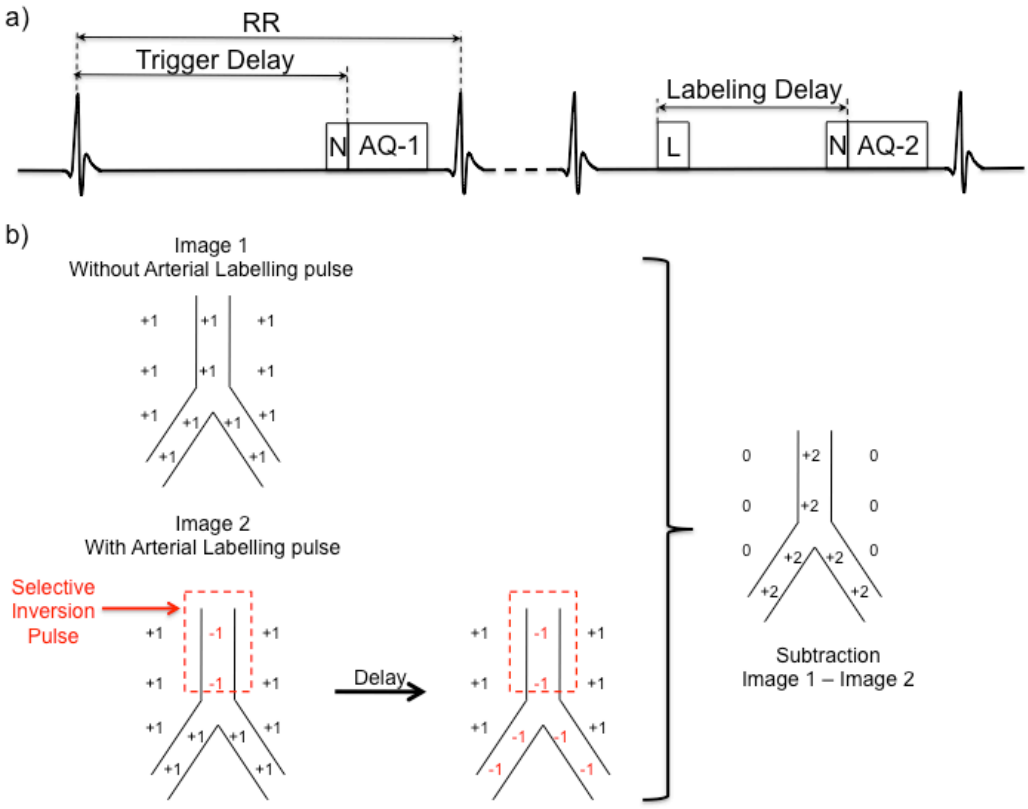

Figure 6.1- (a) Arterial spin labelling (ASL) sequence (16). In the first acquisition no selective inversion pulse is used. In the second acquisition a selective inversion labelling pulse (L) is applied. After a time delay (Labelling Delay) the labelled blood flows into the area of interest and the images are acquired with AQ-1 or AQ-2. (b) Schematic representation of the ASL principle including and the subtraction step to obtain the angiogram with minimal background signal. AQ-1: acquisition 1, AQ-2: acquisition 2

Although ASL has been developed in the 80s (61), it is still clinically underused because of several challenges (121): 1) ASL typically requires two acquisitions (labelled and non-labelled

datasets) leading to an increased scan time, 2) secondly, the need of image subtraction increases the sensitivity for spatial misregistration and 3) thirdly the need of precise planning of the labelling slab and the choice of an optimal time delay for maximum blood to background contrast introduces some “operator dependence”.

A new ASL approach, which partially solves some of these problems, has recently been proposed (124) (Figure 6.2). This method is based on a spatially selective dual-inversion (DIR) prepulse, which labels e.g. aortic blood-pool. The non-selective inversion pulse (nsIR, Figure 6.2a) inverts the magnetization in the entire field-of-view while the spatially selective inversion pulse (sIR, Figure 6.2a) re-inverts the spins of upstream blood. An inversion time delay is used to allow the labelled blood to reach the imaging region and to null the magnetization of static tissue (Figure 6.2b). This approach has been shown to be efficient if the surrounding tissues have similar T1 relaxation times. In regions in which background tissues have a wide range of T1 values, the application of a single inversion time may be insufficient for simultaneous nulling of all tissues (Figure 6.2c). In these cases, the use of a subtraction technique may be necessary. In addition, as this technique has only one “optimal” inversion time delay, there exists a trade-off between background suppression and visualized vessel extent.

Our goal was therefore to develop an ASL technique with good background suppression over a wide T1 range and with a more flexible time delay to individually adjust the visible vessel length and visualize vessels with slower blood flow, like the venous system.

In this work we propose a new ASL sequence, which exploits the ability of two non-selective Inversion Recovery (IR) pulses and a set of optimum delays (TI1 and TI2) to null background signal over a wide range of T1 values (125) while maintaining signal in labelled blood using a third pencil beam or slab selective inversion pulse (TIR4ASL, Figure 6.3a) (62). This allows the acquisition of an angiogram with improved background suppression and without the need of subtraction. Because of the flexible delay time, this technique allows fitting the labelling pulse and the acquisition in 2 or 3 heartbeats; so that even venous vessels with slow flowing blood can be imaged with this technique.

6.2.2 Theoretical Considerations

The concept of two non-selective inversion pulses separated by two optimal delays (TI1 and TI2) allows signal suppression almost independent of T1 and was first demonstrated by

Yarnykh et al (125) for black-blood imaging pre and post contrast administration. The original implementation, quadruple inversion (QIR), consists of two double-inversion RF pulse pairs followed by two inversion delays TI1 and TI2. With a particular combination of parameters TI1 and TI2, this technique allows to null the magnetization (Mz) of the inflowing blood over a wide range of T1 values.

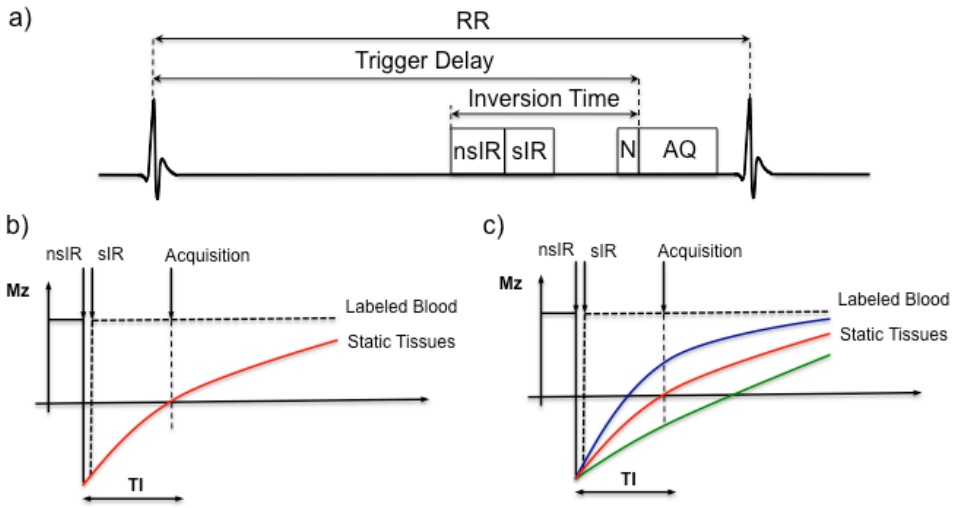

Figure 6.2- (a) DIR sequence (124). (b) A non-selective inversion pulse (nsIR) inverts the magnetization of the whole body and subsequently a spatially selective tagging pulse (sIR) reverts the magnetization of the protons in an upstream artery or vein. The images are acquired after a delay (inversion time) when the magnetization of surrounding tissues crosses the zero-point magnetization. (c) For anatomic regions in which the background tissues have a wide range of T1 relaxation times, the application of a single inversion time may be insufficient for cancelling the background tissue signal.

In our implementation (TIR4ASL), we take advantage of the property of two non-selective inversion pulses to null the signal of background tissue independent of their T1 value while maintaining high blood signal using a third slab selective inversion pulse.

The TIR4ASL prepulse is composed of two pairs of RF pulses (Figure 6.3a). The first pair consists of a non-selective inversion (+180x°) RF pulse followed by a slab selective re-inversion pulse (+180x°). The second pair of RF pulses consists of a non-selective inversion pulse (+180x°) followed by a navigator-restore pulse (+180x°) to restore the magnetization at the right hemi-diaphragm to facilitate navigator gating. With this configuration, the background tissue (tissue in imaging FOV) ‘experiences’ both non-selective inversion pulses and for optimized values of TI1 and TI2, the signal of background tissue can be suppressed over a wide T1 range (Figure 6.3b). In contrast, the upstream labelled blood effectively only ‘experiences’ the second non-selective inversion pulse because of the additional selective IR pulse, and with the right

choice of TI2 the Mz magnetization of the labelled blood should be restored at the time of imaging (Figure 6.3b-d). With the DIR sequence (Figure 6.3c) only one specific tissue with the "optimal" T1 value is crossing the null point of Mz at the moment of the image acquisition while the Mz of the other background tissues has either positive or negative magnetization. This behaviour explains why DIR cannot successfully suppress the entire background signal when the surrounding tissues have a wide range of T1 values.

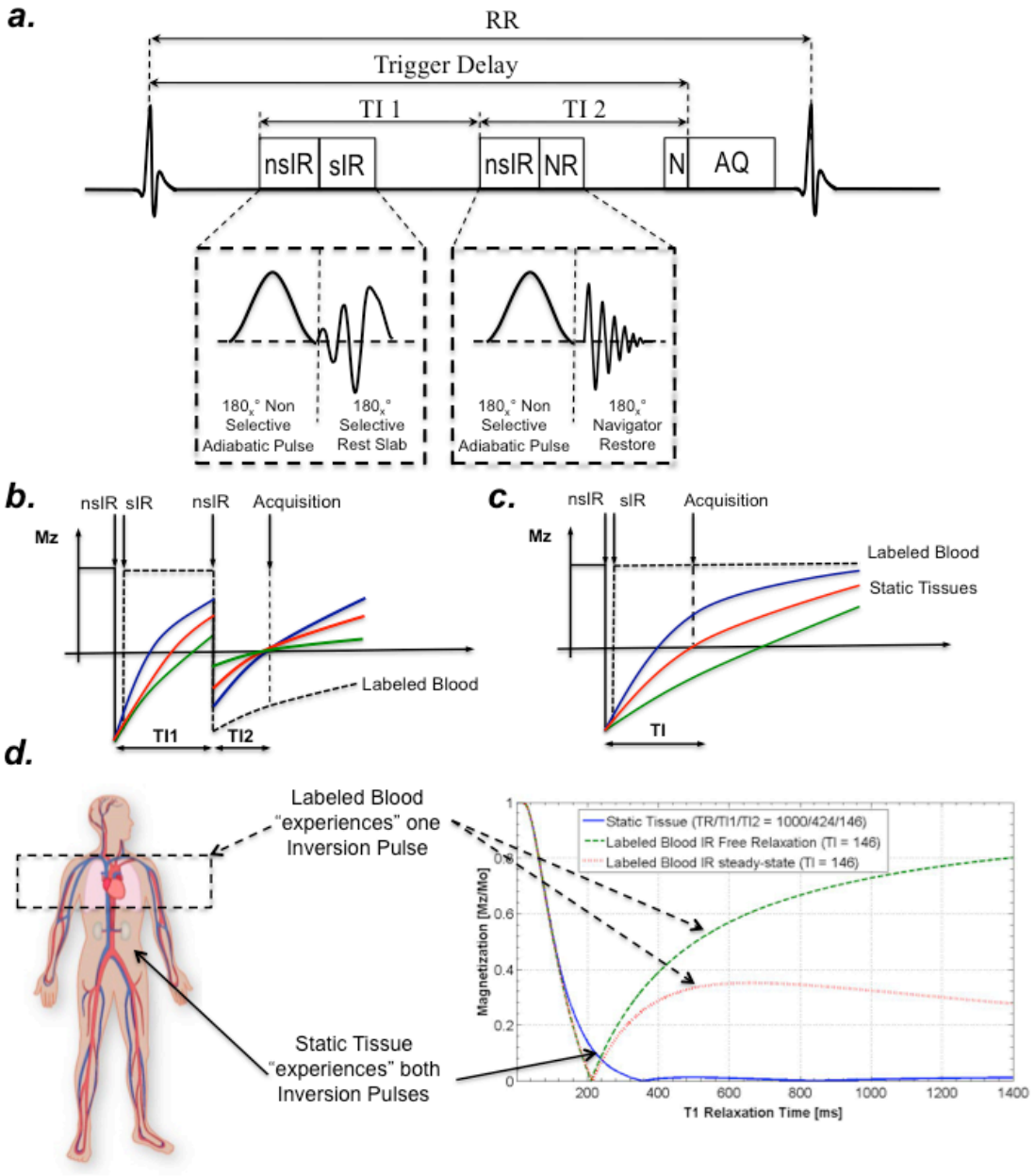

Figure 6.3- (a) TIR4ASL sequence. nsIR: Adiabatic non-selective inversion pulse. sIR: Selective inversion pulse, NR: Navigator restore pulse. N: Navigator, AQ: Image acquisition. (b-c) Diagrams of the Mz magnetization of static tissues with different T1 relaxation times and labelled blood with: (b) TIR4ASL and (c) Double Inversion (DIR-ASL) (23). (d) The graph shows the expected magnetization of static tissues and labelled blood according to Eq. 6.1-6.3. Parameters used were: RR/TI1/TI2=1000/424/146 ms. TIR4ASL: Triple inversion recovery for arterial spin labelling.

The steady state Mz magnetization of background tissue immediately before the imaging sequence and with a single echo acquisition (flip angle=α) is shown in Eq. 6.1 (modified from (125)). The labelled blood only experiences the second non-selective IR pulse. Since blood experiencing the labelling pulse is a mix of "fresh blood" and blood that has already experienced an inversion pulse in the previous cardiac cycle, the Mz magnetization of blood will be between the steady state (Eq. 6.2) and the free relaxation magnetization (fresh blood) solution of an inversion recovery prepulse (Eq. 6.3). With the right choice of TI1 and TI2, signal from static tissue can be suppressed over a wide T1 range while maintaining the signal of labelled blood (Figure 6.3b-d).

$$M_z^{background\ tissue} = \frac{1 - \exp(-RR/T_1) - 2 \cdot \exp(-TI_2/T_1) \cdot [1 - \exp(-TI_1/T_1)]}{1 - \exp(-RR/T_1) \cdot \cos(\alpha)} \quad \text{Eq. [6.1]}$$

$$M_z^{labeled\ blood} = \frac{1 - \exp(-RR/T_1) - 2 \cdot \exp(-TI_2/T_1)}{1 + \exp(-RR/T_1) \cdot \cos(\alpha)} \quad \text{Eq. [6.2]}$$

$$M_z^{labeled\ blood} = 1 - 2 \cdot \exp(-TI_2/T_1) \quad \text{Eq. [6.3]}$$

To find the optimal inversion times we solved an optimization model, which maximizes the area between the magnetization of labelled blood and background tissue (Eq. 6.4) for T1 values between 400 ms and 1500 ms. To correct for data acquisition on signal behaviour, we simulated the prepulse together with a fast gradient echo acquisition with 20 RF excitations per RR interval with a flip angle of 30º. In this optimization model, the restriction [i] allows nulling the background signal. ξ (arbitrary units) provides an additional degree-of-freedom in order to select the strength of background signal suppression. Restriction [ii] restricts the prepulse to one RR interval (Figure 6.3a), however it could be restricted to 2 or 3 RR if longer labelling times (TI1+TI2) are needed. In the optimization model, we modelled the magnetization of labelled blood according to the free relaxation equation (Eq. 6.3). In this work we selected the $T_{1minimum}$ and $T_{1maximum}$ in the physiological range of T1 values between 400ms and 1500 ms (88).

$$MAX\left[\int_{T_{1\,minimum}}^{T_{1\,maximum}}\left(M_z^{labeled\ blood}-M_z^{background\ tissue}\right)\right]$$

$$s.t.$$

$$[i]\quad \int_{T_{1\,minimum}}^{T_{1\,maximum}} M_z^{background\ tissue} \le \xi$$

$$[ii]\quad TI_1+TI_2 \le RR-Acquisition\ window\ duration \qquad \text{Eq. [6.4]}$$

In order to use TIR4ASL for visualization of the venous system, we also developed a modification of this technique in which the pre-pulse and the image acquisition were fitted into two or three RR intervals (restriction ii, Eq. 6.4), which increase the labelling time (TI1 + TI2) and provide more time for the slower venous blood to flow into the area of interest (Figure 6.4).

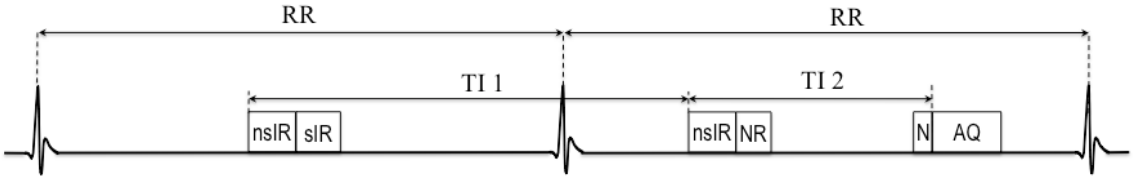

Figure 6.4- TIR4ASL sequence in 2 RR intervals, which increases the labelling time (TI1+TI2) and allows for venography. nsIR: Adiabatic non-selective inversion pulse. sIR: Selective inversion pulse, NR: Navigator restore pulse. N: Navigator, AQ: Image acquisition.

6.2.3 Materials and Methods

TIR4ASL prepulse: The TIR4ASL pre-pulse was implemented on a 1.5T Achieva Gyroscan MR scanner (Philips Healthcare, Best, NL). The non-selective pulses are adiabatic hyperbolic-secant phase-modulated pulses of 10 ms duration. The slab selective RF pulse was an adiabatic pulse of hyperbolic-secant shape, with two-side lobes, bandwidth of 1,670 Hz, angle of +180x° and a duration of 5 ms for a slab thickness of 25 mm. The inversion delays TI1 and TI2 were chosen to maximize blood to background contrast, and the solution of the minimization problem (Eq. 6.4) was found numerically using Matlab (Mathworks, Natick, MA).

Imaging sequence: TIR4ASL can be combined with any imaging readout. In this work we combined it with an ECG triggered 3D segmented k-space gradient echo readout and with a balance steady-state free precession (b-SSFP) readout. The imaging parameters included: FOV=350 mm and acquisition matrix=320x320 resulting in 1 mm in-plane spatial resolution and slice thickness=2 mm. For the gradient echo acquisition the following parameter were used: 20 RF excitations per RR interval, TR/TE=5.5/1.68 ms and flip angle=30°. For the b-SSFP

acquisition the following parameters where used: acquisition window: 120 ms, 7 start-up echoes, TR/TE=4.8/2.4 and flip angle=70°. A respiratory navigator and a fat suppression prepulse preceded the imaging sequence. All images were obtained using a 32-element cardiac coil.

Experimental setup:

Phantom validation: First we investigated the signal behaviour of the TIR4ASL sequence in a T1-phantom with samples ranging from 100 ms to 1600 ms. The labelling pulse was positioned over the bottles with T1 values similar to arterial blood, i.e. 1100 to 1500 ms to validate our simulations (Figure 6.5a).

Arterial angiograms: To test TIR4ASL *in vivo*, renal angiograms were obtained in ten healthy adult subjects (8 men, mean age: 31 years old; range 26–40 years). The rest slab for blood labelling was positioned above the diaphragm extending to the aortic arch, and the imaging volume covered both kidneys (Figure 6.6). The respiratory navigator was positioned over the right hemi-diaphragm and a gating window of 7 mm was used. For comparison, we acquired three Double Inversion Recovery (DIR) renal angiograms using inversion times (TI) of 300, 450 and 600 ms while maintaining all other imaging parameters.

Venograms: To test the feasibility to use TIR4ASL to obtain venograms, we used this sequence to image three major venous systems susceptible of thrombosis: Portal, Renal and Iliac veins (6,126). We also tested the feasibility of obtaining pulmonary artery angiograms, which could be useful for the diagnosis of pulmonary embolism, the most common DVT complication. The planning of those protocols are shown in figure 6.7 for (a) Portal, (b) iliac, (c) Renal veins, and (d) pulmonary arteries. The location of the rest-slab for blood labelling defines the targeted vessels; for portal vein venography (Figure 6.7a) the rest slab was positioned over the abdominal cavity in order to label blood of the superior mesenteric and splenic veins; for the iliac venogram (Figure 6.7b), the rest slab was positioned over the pelvis to label the blood in the femoral and internal iliac veins. For renal venography (Figure 6.7c) the rest slab was positioned over the kidneys to label the inflowing blood of the renal arteries and the blood in the kidneys. For the pulmonary artery angiogram (Figure 6.7d), the rest slab was positioned in sagittal orientation over the heart, in order to label blood in the right and left ventricle that

subsequently will move into the pulmonary artery and aorta. In all cases the acquisition was oriented in the transverse plane with phase encoding in left-right direction.

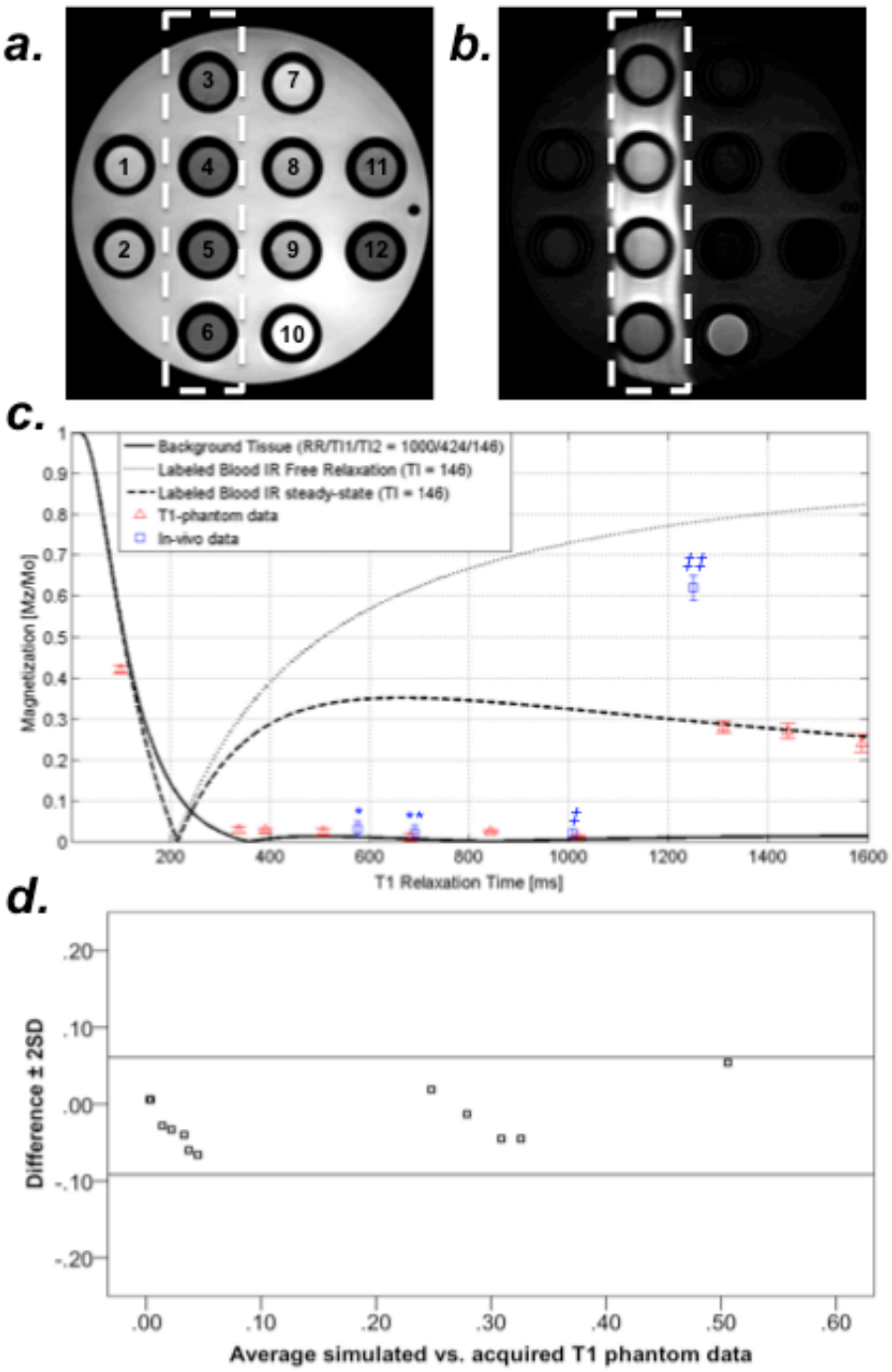

Figure 6.5- Validation of TIR4ASL in T1 phantom (RR/TI1/TI2=1000/424/146 ms). (a) Bottles with T1 values ranging from 100 ms to 1650 ms. (1=340 ms, 2=505 ms, 3=1170 ms, 4=1310 ms, 5=1440 ms, 6=1580 ms, 7=320 ms, 8=680 ms, 9=845 ms, 10=100 ms, 11=1020 ms, 12=1650 ms) acquired with T1weighted Gradient-Echo Imaging (b) Image obtained with TIR4ASL. The labelled bottles had a T1 value between 1100ms and 1600 ms. (c) Phantom and in vivo data for liver (*), kidneys (**), muscle (‡) and arterial blood (‡‡) (T1 values=580, 690, 1000 and 1250 ms, respectively) compared with the expected magnetization curves according to simulations. (d) Bland-Altman plot showing good agreement and no significant bias between simulations and acquired data in a T1 phantom.

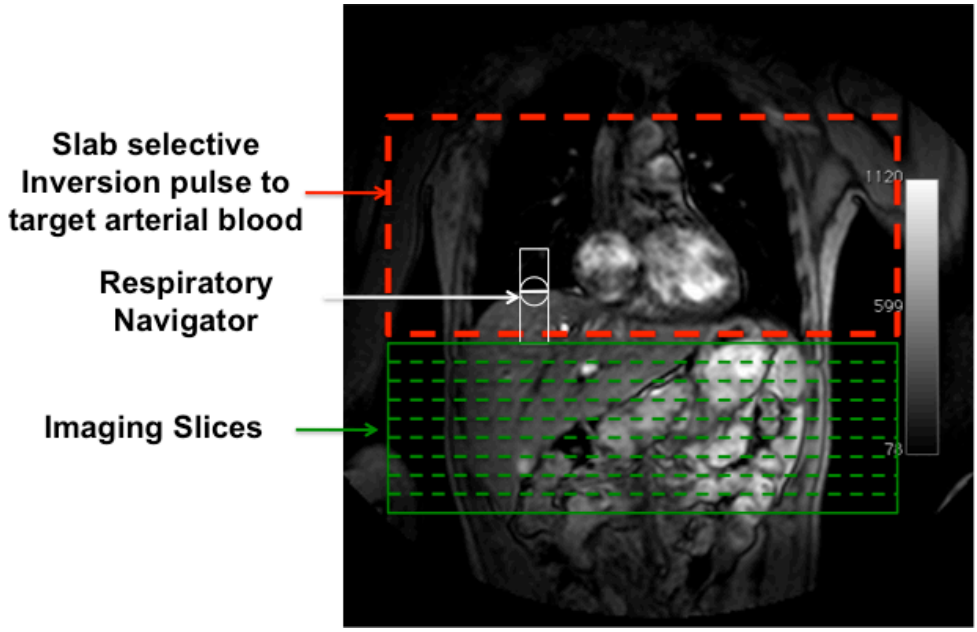

Figure 6.6- TIR4ASL scan planning for renal artery acquisition. Segmented red box shows the position of the selective inversion pulse (rest slab) Green lines show the location of the Field of View (FOV) of the image acquisition. The respiratory navigator was located over the right hemi-diaphragm.

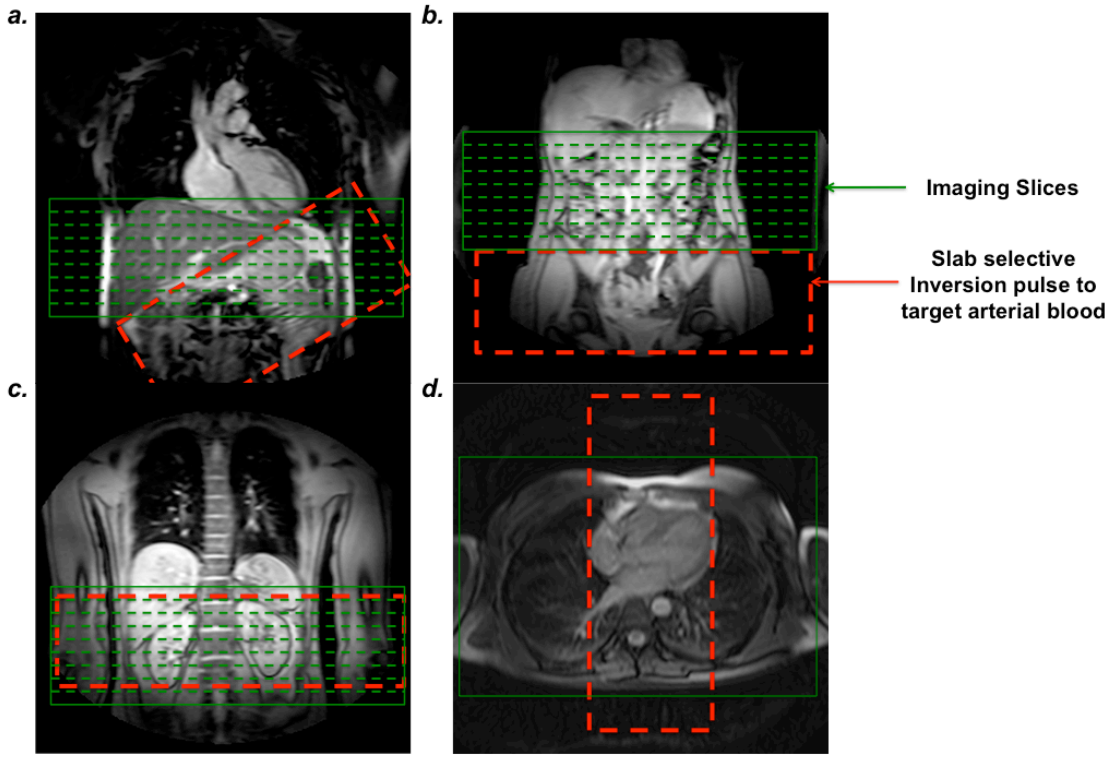

Figure 6.7- TIR4ASL scan planning for (a) Portal vein, (b) iliac vein, (c) Renal vein, and (d) pulmonary arteries. Segmented red box shows the position of the selective inversion pulse (rest slab). Green lines show the location of the Field of View (FOV) of the image acquisition.

Image analysis: For comparison of the renal artery angiogram using TIR4ASL and DIR-ASL sequence, we evaluated the signal-to-noise ratio (SNR) of labelled blood and the contrast-to-noise ratio (CNR) between blood and surrounding tissues: muscle, liver and kidneys (renal cortex). To evaluate the visualized vessel length we identified the renal artery branches in each protocol. The identified segments from proximal to distal were: Level A: abdominal aorta; Level B: proximal renal artery; Level C: renal artery before its main branches; Level D: main renal artery branches (anterior and posterior branches); Level E: segmental arteries; and Level F: Inter-lobar arteries.

Statistics: Continuous data are expressed as the mean ± 1 SD. Data from different techniques were compared using a one-way ANOVA test. The measures of agreement between simulated and real data were measured using linear regression analysis and Bland-Altman method. All statistical analysis was done using SPSS Statistics software package release 19.0 (IBM Corporation, Somers, NY, USA).

6.2.4 Results

We identified a set of inversion delays (TI1 and TI2) that provided the optimum solution for different ξ values (Eq. 6.4). In table 6.1 a group of solutions for RR=800, 900 and 1000 ms, and for ξ=10.0 and 20.0 (arbitrary units) are shown. For a given RR interval, the total pre-pulse duration (TI1+TI2) increase with lower ξ values. For an RR interval of less than 1000 ms, with an acquisition window of 120 ms in mid-diastole, the lowest ξ that allows keeping prepulse and image acquisition in one RR interval was ξ=10.

RR [ms]	ξ [Arbitrary units]	TI_1 [ms]	TI_2 [ms]
1000	10.0	424	146
900	10.0	380	131
800	10.0	335	115
1000	20.0	407	123
900	20.0	364	106
800	20.0	321	86

Table 6.1- Inversion times (TI1 and TI2) obtained from the optimization procedures for TIR4ASL sequence (Eq. 6.4) that maximize contrast between target blood and surrounding tissues for a given RR interval and ξ. A gradient echo readout with 20 excitations and a flip angle of 30° was chosen.

For venograms we perform the same optimization protocol but we used a "corrected RR" which is basically twice the RR interval for a given heart rate. Table 6.2 shows the optimal solutions for ξ=10.0. Longer labelling times (TI1 + TI2) and excellent background suppression was observed for the "double RR" protocol (Figure 6.8) using the simulations.

Heart Rate [bpm]	RR original [ms]	Double RR [ms]	TI_1 [ms]	TI_2 [ms]
45	1,330	2,660	968	274
50	1,200	2,400	904	264
55	1,100	2,200	853	254
60	1,000	2,000	798	244
67	900	1,800	738	232
75	800	1,600	671	218
80	750	1,500	635	210
85	700	1,400	599	202
90	670	1,340	560	192

Table 6.2- Inversion times (TI1 and TI2) obtained from the optimization procedures (Eq. 6.4) with the "Double RR" TIR4ASL methodology for venous angiograms

Phantom Results:

For the phantom acquisition we used the optimal parameters: RR/TI1/TI2=1000/424/146 ms. The signal intensity of bottles with similar T1 values as that of blood followed the solution of the steady state equation of an inversion recovery prepulse (Eq. 6.2) because of the absence of inflow effect (Figure 6.5b-c). Good agreement ($y=0.8971x + 0.0349$, $R^2=0.96$, $P<0.001$) and no significant bias in Bland-Altman plots (Figure 6.5d) was found between simulations and acquired data in a T1 phantom.

Renal Artery angiography:

For renal angiography using TIR4ASL we used the scan planning showed in Figure 6.6 and the following optimal parameters (ξ=10): RR/TI1/TI2=1000/424/146 ms and 900/380/131 ms. The *in vivo* signal behaviours of tissues such as liver, kidneys and muscle and of labelled arterial blood are shown in Figure 6.5c. The signal of background tissues is almost completely suppressed while the signal intensity of labelled blood is between the solution of the steady state (Eq. 6.2) and free relaxation (fresh blood) (Eq. 6.3) magnetization, which supports our hypothesis that

labelled blood is a mix of fresh blood with fully recovered magnetization and blood that has already experienced an inversion pulse in a previous cardiac cycle.

Renal arteries including small branches were successfully visualized with TIR4ASL in all subjects. Figure 6.9 shows representative abdominal aorta angiograms obtained using TIR4ASL, showing the abdominal aorta main branches: superior mesenteric, celiac trunk and renal arteries including their main branches and the segmental arteries.

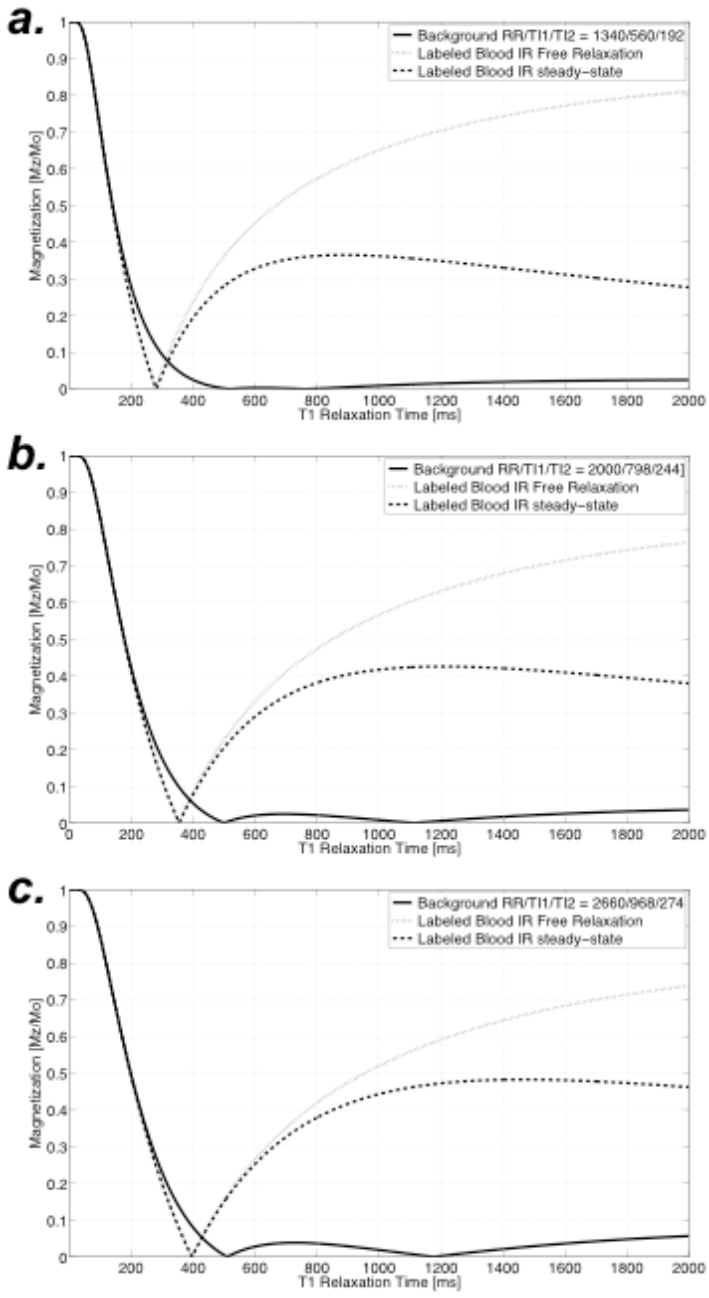

Figure 6.8- Expected magnetization of static tissues and labelled blood according to Eq. 6.1-6.3 for the "double RR" protocol. Parameters used were: (a) RR/TI1/TI2=1340/560/192 ms; (b) RR/TI1/TI2=2000/798/244 ms; (c) RR/TI1/TI2=2660/968/274 ms (Table 6.2)

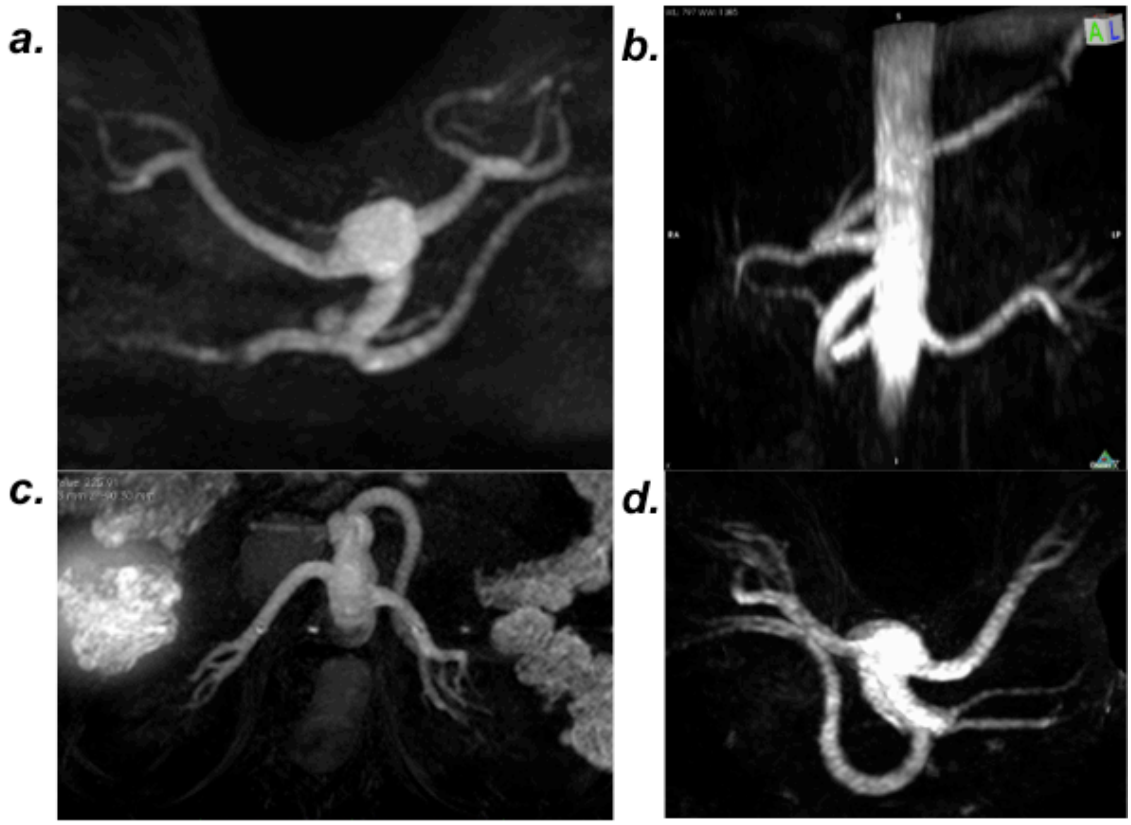

Figure 6.9- Maximum Intensity Projection (MIP) reconstruction showing different projections of the labelled blood in the abdominal aorta and its main branches: superior mesenteric, celiac trunk and renal arteries, including the distal renal branches: segmental and inter-lobar arteries.

TIR4ASL effectively suppressed the background signal over a wide range of T1 values as predicted by our simulations. Representative slices for TIR4ASL and DIR-ASL are shown at the level of renal arteries in the same subject (Figure 6.10a-d) demonstrating improved blood to background contrast with TIR4ASL.

The SNR of blood with TIR4ASL is almost 3 fold higher of that obtained with DIR-ASL ($P<0.001$) (Figure 6.11a). The CNR between blood and background was increased approximately 5 fold with TIR4ASL compared with DIR-ASL ($P<0.001$) (Figure 6.11b). DIR-ASL visualized the aorta and renal arteries from their origin in the abdominal aorta (level A) until their main branches (level C) with the three delays used. Renal arteries at level D were only visualized by DIR-ASL with delays of 450 and 600 ms (Figure 6.10c). None of the DIR-ASL images clearly visualized the segmental arteries, partially because the labelled blood did not have sufficient time to reach this distal area and because of the high background signal from the kidneys because of the long inversion time delay (TI). In contrast TIR4ASL clearly visualized the renal artery until their

segmental branches (level E) (Figure 6.11c) and in 4 of the 10 volunteers (40%) the inter-lobar arteries were also partially visualized.

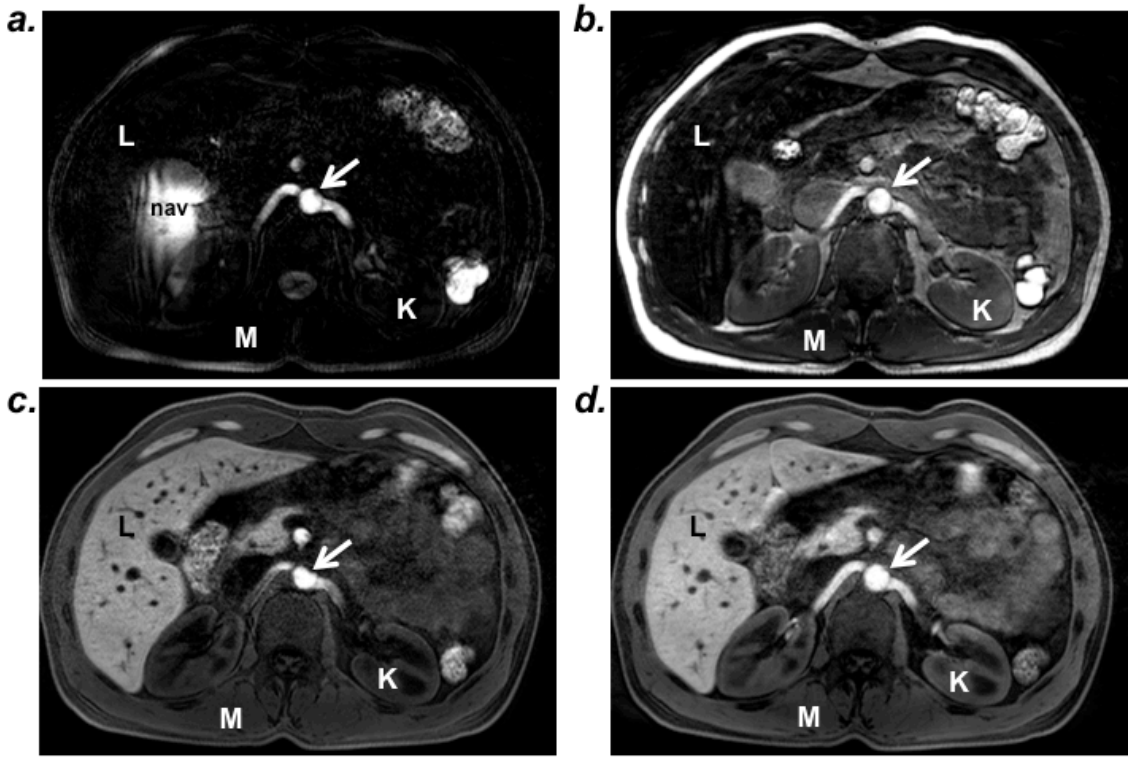

Figure 6.10- Transverse slice at the renal artery level demonstrating improved background suppression with TIR4ASL (e) compared with DIR-ASL (inversion time (TI) of 300 ms (f), 450 ms (g) and 600 ms (h)). L=liver; M=muscle; K=kidneys; nav=respiratory navigator artefact.

Venograms:

Portal venography and renal venography were successfully obtained with TIR4ASL using the "double RR" protocol. Figure 6.12 shows the MIP reconstruction of the portal venogram, showing clear delineation of the splenic veins, superior mesenteric vein, and the portal vein and its main and segmental branches in healthy volunteers. Excellent background suppression and clear vessel lumen definition were obtained wit TIR4ASL–double RR protocol.

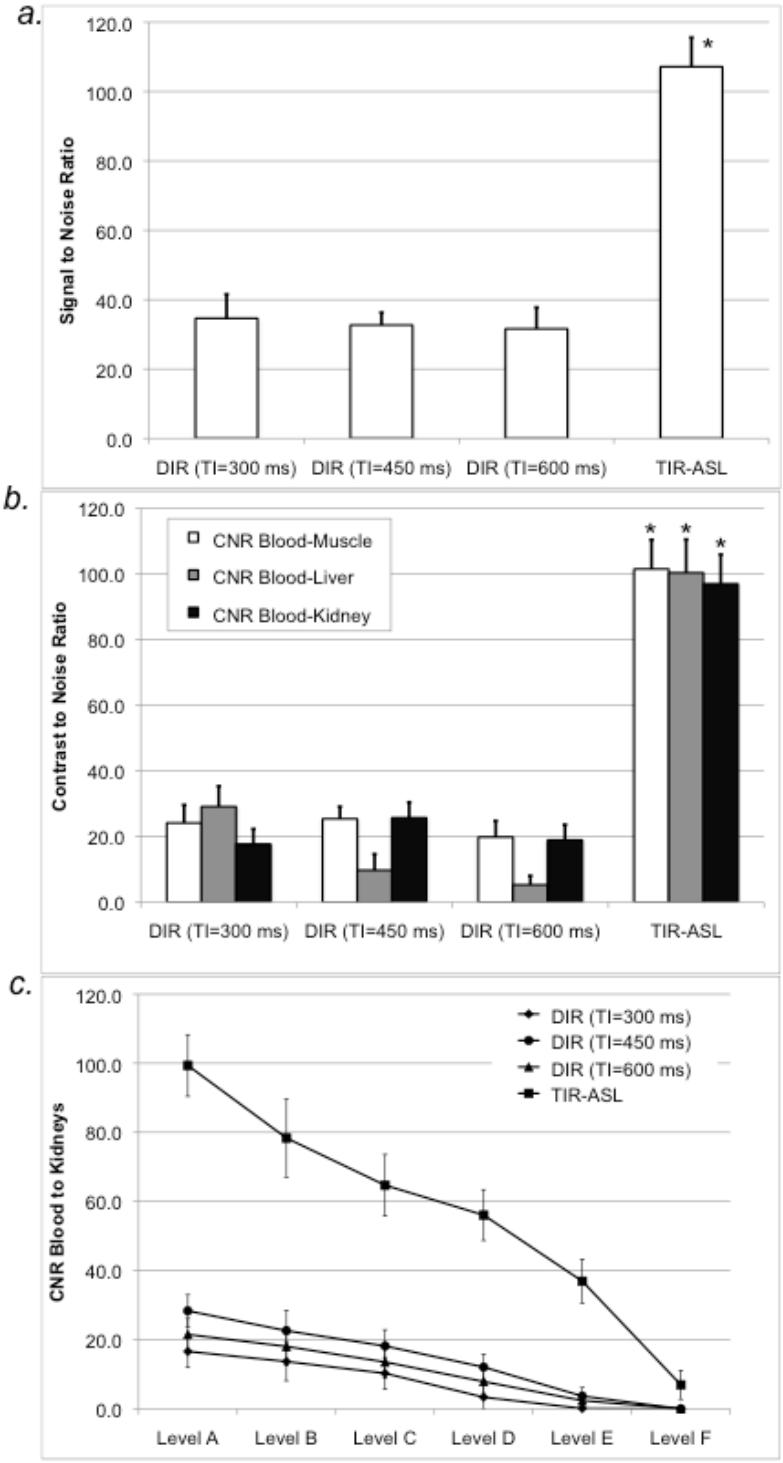

Figure 6.11- SNR (a) and CNR (b) of labelled blood and background tissue (muscle, liver, kidneys) for TIR4ASL (RR/TI1/TI2 = 1000/424/146 ms) and DIR (TI = 300, 450, and 600 ms) (*) P<0.001. (c) CNR between labelled blood and kidneys at different levels (from proximal to distal: Level A: abdominal aorta; Level B: proximal renal artery; Level C: renal artery just before its main branches; Level D: main renal artery branches (anterior and posterior branches of renal artery); Level E: segmental arteries and Level F: Inter-lobar arteries).

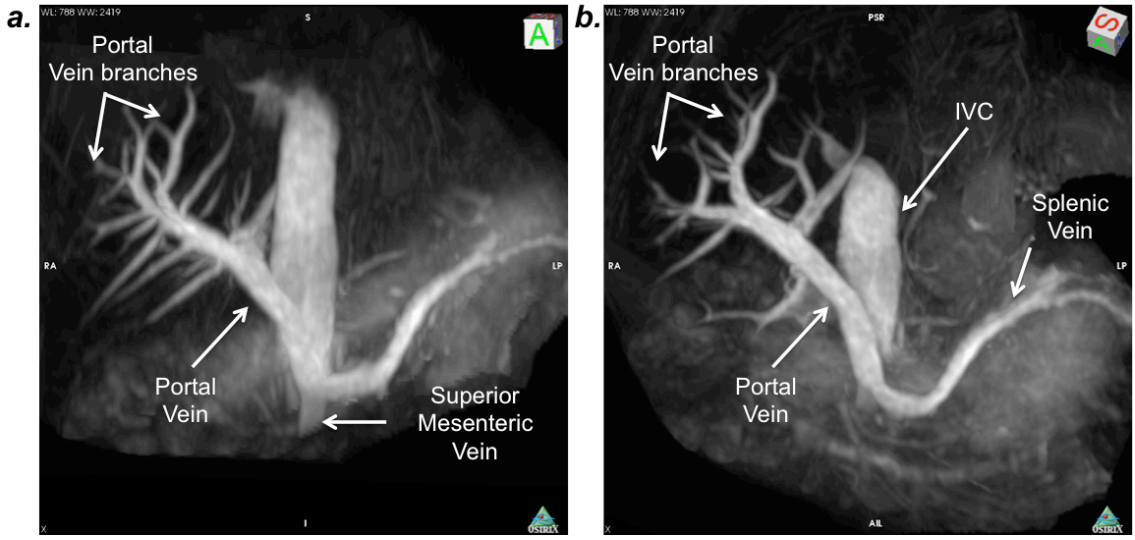

Figure 6.12- Maximum Intensity Projection (MIP) reconstruction of the Portal Veins using TIR4ASL. Anterior (a) and oblique (b) views are shown. Because of the rest-slab location, it is possible to visualize the portal vein and its main and segmental branches, the superior mesenteric vein, the splenic vein, and the inferior vena cava (IVC).

Figure 6.13 shows transverse slices at different abdominal levels in a healthy volunteer showing the renal veins (6.13a) and arteries (6.13b). Because the rest slab was located over the kidneys it was possible to visualize both renal veins. In case of the renal arteries the rest slab was located over the heart and the image shows the labelled blood both in the abdominal aorta and the renal arteries.

Iliac arteries and veins were also successfully imaged using TIR4ASL. First, the rest slab was located over the abdominal aorta and the iliac artery angiograms were obtained, showing a good delineation of the distal portion of the abdominal aorta, the common iliac arteries until their main bifurcation (Figure 6.14a). The imaging of the iliac veins represent a more challenging task, firstly because of the slow movement of the venous iliac blood, and secondly because the rest slab position. It just labelled a small volume of blood in the femoral and internal iliac veins (Figure 6.7b). However it was possible to visualize the iliac vein from the confluence of the internal and external iliac vein until the distal portion of the inferior vena cava (Figure 6.14b). The image shows a decrease in the signal intensity from the iliac vein until the IVC, and this effect could be explained because the small volume of labelled blood. We hypothesise that this problem could be solved using a flow independent technique that will be presented in the next section.

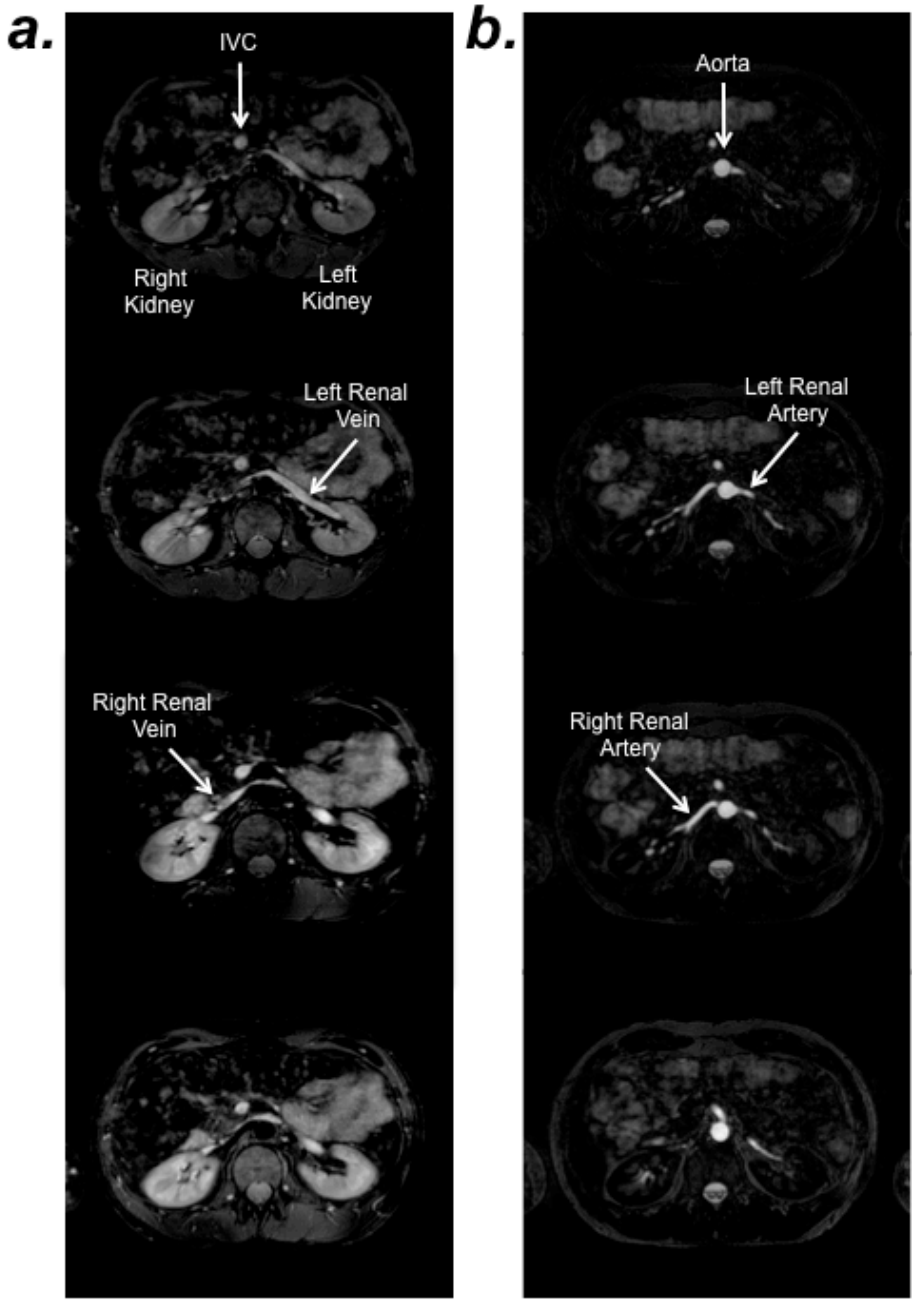

Figure 6.13- Transverse view of the right and left (a) renal veins and (b) renal arteries obtained with TIR4ASL. IVC: inferior vena cava

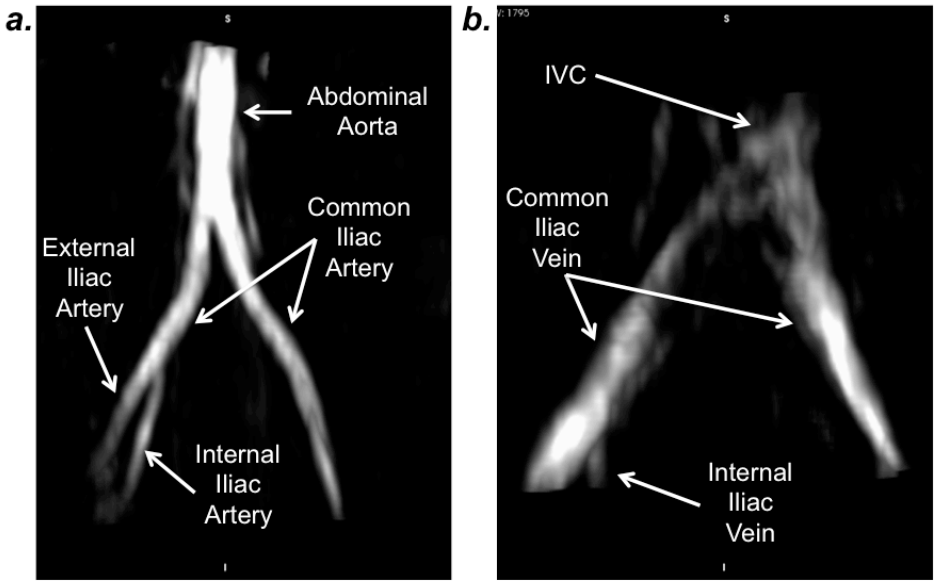

Figure 6.14- Maximum Intensity Projection (MIP) reconstruction of the (a) Iliac artery and (b) iliac veins using TIR4ASL.

Pulmonary artery angiogram:

Pulmonary angiograms were obtained in 10 healthy volunteers. Figure 6.15 shows a representative MIP reconstruction of the pulmonary angiograms. It is possible to visualize the right and left pulmonary arteries, and some of their lobar and segmental arteries. The images also show the Aortic arch and some residual signal from the heart, where the rest slab was located.

6.2.5 Conclusion and Discussion

The visualization of lumen integrity is an important diagnostic tool in medicine. The small difference in T1 relaxation time between blood and surrounding tissue often leads to insufficient contrast and thus inadequate vessel visualization and delineation for diagnostic purposes. This problem can be addressed by the use of extracellular or intravascular contrast agents, which improve vessel visualization, but its application in children, pregnant women or patients with renal dysfunction is not recommended except in clinically justified situations.

The DIR-ASL (124) technique partially solves these problems, however, this methodology cannot completely null signal from the background tissue over the entire FOV. Thus, contrast between the vessel lumen and background tissue may be decreased, leading to suboptimal vessel delineation.

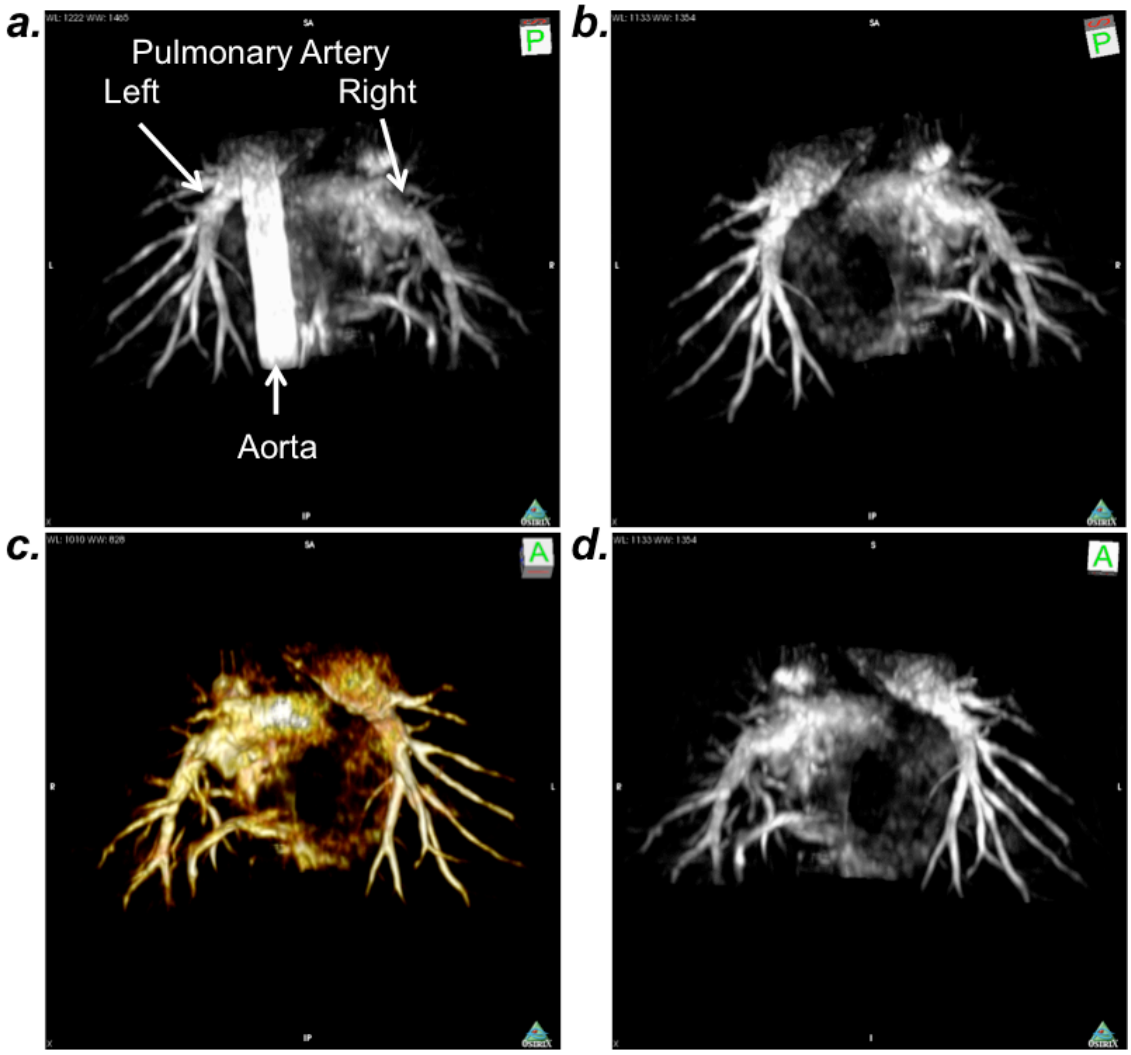

Figure 6.15- Pulmonary Artery Angiography using TIR4ASL

The use of multiple inversion pulses to reduce the background signal in ASL angiograms was proposed almost 20 years ago (127), however this approach requires image subtraction. Recently, Yarnykh et al (125) has shown that with the use of two inversion pulses and optimal inversion delays, background signal can be nulled over a wide range of T1 relaxation times. In the present study, we demonstrate that adding a third slab selective inversion pulse (TIR4ASL) allows the acquisition of a non-contrast enhanced MR angiogram with excellent background suppression without increasing scan time. In comparison to DIR-ASL, TIR4ASL yielded higher blood signal, better background suppression and improved vessel delineation.

TIR4ASL provides an alternative for non-contrast enhanced angiography and addresses the challenges of traditional ASL techniques. TIR4ASL only requires one image acquisition and obviates the subtraction step. As TIR4ASL provides a group of optimal inversion times it is more

flexible and allows adjusting the extent of visible vessel without significantly compromising the suppression of background tissue. The optimal inversion delays only depend on the patient's heart rate and the prior defined strength of background signal suppression. Thus, it has potential to be applied in a clinical setting due to the minimized 'operator dependence'.

Because of the excellent background suppression and the long total labelling delay (TI1 + TI2), TIR4ASL even allows visualizing small side artery branches (e.g. segmental and inter-lobar arteries), and thus provides a promising tool for clinical applications requiring side branch visualization. Additionally the "double RR" protocol allows to further increase the labelling delay and thus also to visualize the venous system, like portal and renal veins.

TIR4ASL was implemented using a slab selective inversion pulse, but it also could be combined with a pencil beam inversion pulse, thereby allowing to selectively label arteries or veins and to investigate their individual contribution to tissue perfusion (123). Similarly, with the use of a pencil beam it could be feasible to label aortic and left ventricular blood to obtain coronary artery angiograms as previously shown by Katoh and co-workers using DIR-ASL (124).

One potential limitation of TIR-ASL may be the need of a constant heart rate in order to reach the steady state of the background tissue magnetization. Simulations show that even for a change in heart rate of ±10% background suppression is almost unaffected (Figure 6.16), which demonstrates the robustness of this technique with respect to heart rate variation.

In conclusion, TIR-ASL has been successfully demonstrated to obtain non-contrast enhanced angiograms and venograms in phantom and volunteer studies and may have potential to screen asymptomatic patients with suspected vascular disease or to follow patients after medical or interventional treatment. TIR-ASL is contrast-free and could be applied in children, pregnant women, elderly people and patients with renal dysfunction. In areas with very slow flow, like limb areas, a flow insensitive technique should improve our results.

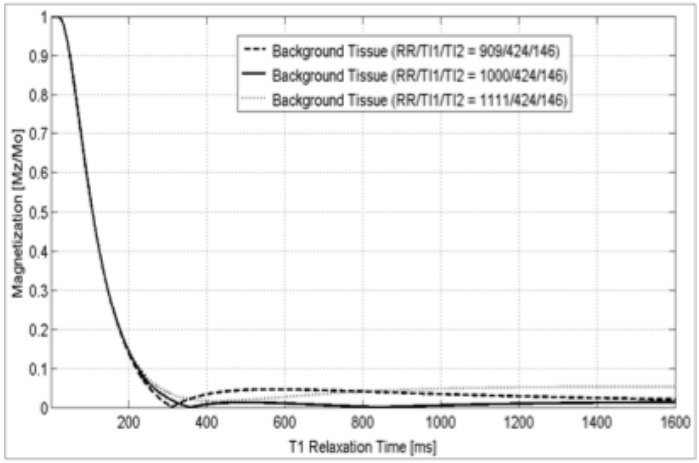

Figure 6.16. Simulation of the effect of heart rate variation (± 10% bpm) on the steady state longitudinal magnetization (Mz) of background tissue. Baseline: heart frequency=60 bpm, RR/TI1/TI2=1000/424/146 ms. +10% bpm: heart frequency of 66 bpm (RR=909 ms) and -10% bpm: 54 bpm (RR=1111 ms).

6.3 Flow independent Venography using a Dynamic T2-preparation acquisition

6.3.1 Introduction

The main challenge of flow dependent angiography sequence like ASL or TIR4ASL is that they rely on blood flow, which may be insufficient in some areas, like the limbs and in patients with vascular diseases. This problem is particularly important in the venography, where the venous blood flow is naturally slow and could be even slower in pathologic cases.

In this section we propose to use a balanced Steady-State Free Precession (b-SSFP) sequence (128) and the T2preparation pre-pulse (64) in order to decrease the signal of the background tissue and maintain the signal of venous and arterial blood, and therefore obtain a flow insensitive venogram. We optimized the protocol to obtain venograms and finally we propose a combined protocol between b-SSFP T2prep and TIR4ASL, which successfully visualizes the veins without the need of a contrast agent.

6.3.2 Theoretical Considerations

Balance SSFP is a modified gradient echo sequence in which a non-zero steady state develops for both components of magnetization (transverse and longitudinal) and also a condition where the TR is shorter than the T1 and T2 times of the tissue. If the RF pulses are close enough together, the MR signal will never completely decay, implying that the spins in the transverse plane never completely dephase. While the classical spin echo sequence either shows a T1- or

a T2-weighted contrast, b-SSFP, exhibit a relatively complicated contrast that is composed of T1 and T2 contributions, and in a simplified way the contrast is proportional to T2/T1 ratio (128,129). b-SSFP sequence has been successfully used in cardiovascular applications because of the T2/T1 ratio of arterial blood is larger than of most of other tissues (128).

T2 preparation (T2prep) is a pre-pulse that has been successfully applied to increase the contrast between coronary arteries and surrounding tissues, such as myocardium and fat, based on their T2 differences (64) ($T2_{arterial\ blood}$=290ms, $T2_{mucle}$=40ms) (88). In the presence of this pre-pulse, signal from tissues with a shorter T2 relaxation time decay faster while signal from tissues or fluids with longer T2 is maintained. Because arterial blood has a long T2, its signal only decays slowly while signal of muscle decays more rapidly, thereby increasing the contrast between arterial blood and myocardium (64,130).

A simulation of the steady-state magnetization using b-SSFP as a function of the T2prep duration is shown in Figure 6.17 for three different tissues: arterial blood (T1=1200 ms, T2=290 ms), venous blood (T1=1200 ms, T2=60 ms), and muscle (T1= 800 ms, T2=40 ms) (88).

Static tissue (muscle) experiences the RF pulses of the non-selective T2prep and the RF pulses of the image acquisition every heartbeat. Arterial blood outside the imaging volume only experiences the RF pulses of the T2prep while arterial blood within the imaging volume experiences both the T2prep and the imaging sequence. Venous blood should have an intermediate behaviour, because its flow velocity is slower than that of arterial blood. For the purpose of this simulation we will consider venous blood as a “static tissue”. The parameters considered for the simulation included: TR/TE=4.4/2.2 ms, flip angle of 70º, 7 dummy echoes, acquisition window of 120 ms, and 27 lines acquired per heartbeat. We used a heart rate of 60 beats/min (RR interval of 1000 ms). The T2 preparation prepulse was simulated with 2 adiabatic refocusing 180º pulses, with a spoiler gradient at the end of the pre-pulse and with a variable duration (T2prep duration). The steady state magnetization of the three tissues was simulated in the centre of k-space. Two cases were simulated, b-SSFP acquisition with and without T2prep (Figure 6.17).

In the b-SSFP acquisition without T2prep the magnetization of arterial blood is the highest because it has a longer T2 relaxation time than other tissues, and as the ratio consequently T2/T1 is biggest for arterial blood. Muscle and venous blood have similar magnetization

because they have similar a T2/T1 ratio. This is why this sequence has been successfully used to image the coronary arteries as it can suppress signal from the myocardium and venous blood, while maintaining the signal of coronary artery blood. When b-SSFP is combined with a T2prep prepulse, it is possible to further increase the contrast between venous blood and muscle. In fact, Figure 6.17d shows that there is an optimum T2 preparation duration that maximizes the contrast between these two tissues, which is around 60 ms. In this simulations we have assumed that venous blood behaves like “static-tissue”, and therefore we would expect that the actual venous blood magnetization should be slightly higher than in our simulations.

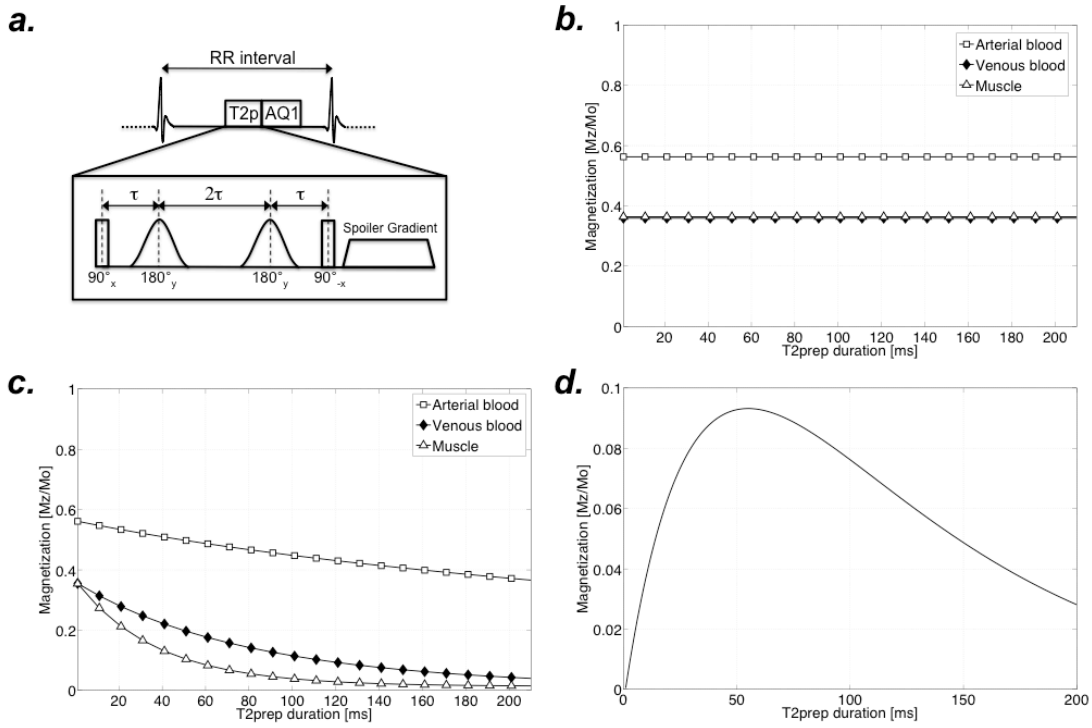

Figure 6.17- Balance SSFP acquisition simulation for muscle and arterial and venous blood with (c) and without (b) T2 preparation (a) pre-pulse (T2prep). Without T2prep there is a negligible difference between the magnetization of venous blood and muscle, however with T2prep this difference is increased, and reaches a maximum when T2prep duration is around 60-70 ms (d) for a heart frequency of 60 bpm (RR-interval=1,000 ms).

6.3.3 Materials and Methods

Experimental setup: We acquired b-SSFP images of the pelvis with and without T2prep in ten healthy adult subjects (8 men, mean age: 31 years; range 26–40). We used a T2 preparation pre-pulse (64,130) with a duration of 70 ms and 2 non-selective, adiabatic, 180° refocusing pulses. In the same group of volunteers we also applied a TIR4ASL protocol to image the iliac arteries using the planning showed in Figure 6.7a.

Imaging sequence: For the b-SSFP acquisition we used a 3D balanced Steady State Free Precession gradient echo sequence, with phase encoding in left-right direction. Imaging parameters included flip angle=70°, TR/TE=4.4/2.2 ms, acquired matrix=250x250, slice thickness=4 mm, acquired resolution=1x1 mm^2, reconstructed resolution=0.5x0.5 mm^2, and 70 reconstructed slices; acquisition window=120 ms, mid-diastolic trigger delay and a low-high profile order for k-space filling. A fat suppression pre-pulse preceded the imaging sequence. All images were obtained using a 32-element cardiac coil. For the TIR4ASL acquisition we used the same parameters as described in section 6.2.3.

Image analysis: Image post processing was performed using custom-made software implemented in Matlab (Mathworks, Natick, MA, USA) and OsiriX (The Osirix Foundation, Geneva, Switzerland).

6.3.4 Results

Figure 6.18 shows a representative transverse slice of the pelvis acquired with b-SSFP with (T2prep(+)) and without (T2prep(-)) T2 preparation pre-pulse. The application of the T2prep pre-pulse suppressed signal of muscle, but maintained both signal of arterial and venous blood.

Figure 6.19 shows the MIP reconstruction of both protocols: b-SSFP without (6.19a) and with (6.19b) T2prep. In both cases it was possible to reconstruct the inferior cava vein (IVC) and the Aorta, however vessel delineation and background suppression was improved with the T2prep(+) protocol.

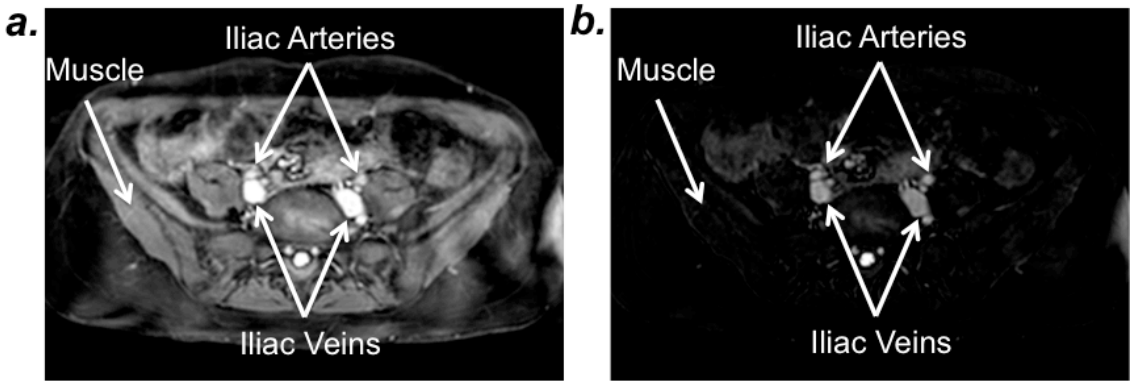

Figure 6.18- Transverse slice at the pelvis level acquired using a b-SSFP protocol without (a) and with (b) a T2 preparation pre-pulse (T2prep)

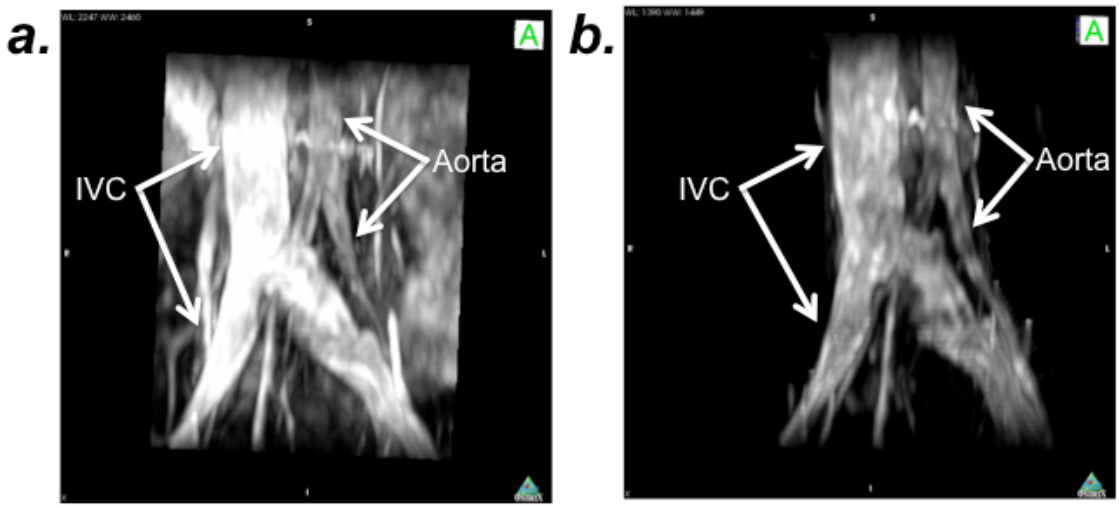

Figure 6.19- MIP reconstruction of the distal abdominal Aorta and Inferior Vena Cava (IVC) from a dataset acquired using a b-SSFP sequence without (a) and with (b) T2 preparation pre-pulse (T2prep)

In the reconstructed MIP in both b-SSFP protocols it was possible to visualize the Aorta and the IVC, and both angiograms were obtained in flow insensitive way. With this technique, however, it is not possible to separate veins from arteries. In the previous section we demonstrated that the TIR4ASL protocol is a robust technique for imaging arterial blood, while it is less robust for imaging very slow flowing venous blood. In order to obtain non-contrast enhanced venograms we used the aortic and iliac artery images obtained with TIR4ASL (Figure 6.19b) as a mask, and then subtracted the b-SSFP images to obtain a “selective” venogram (Figure 6.20c for b-SSFP without T2prep and Figure 6.21c for b-SSFP with T2prep).

In both cases (b-SSFP with and without T2prep) it was possible to obtain a non-contrast enhanced and flow insensitive venogram. We found that the T2prep(+) images showed slightly less noise and better background suppression compared to the T2prep(-) images.

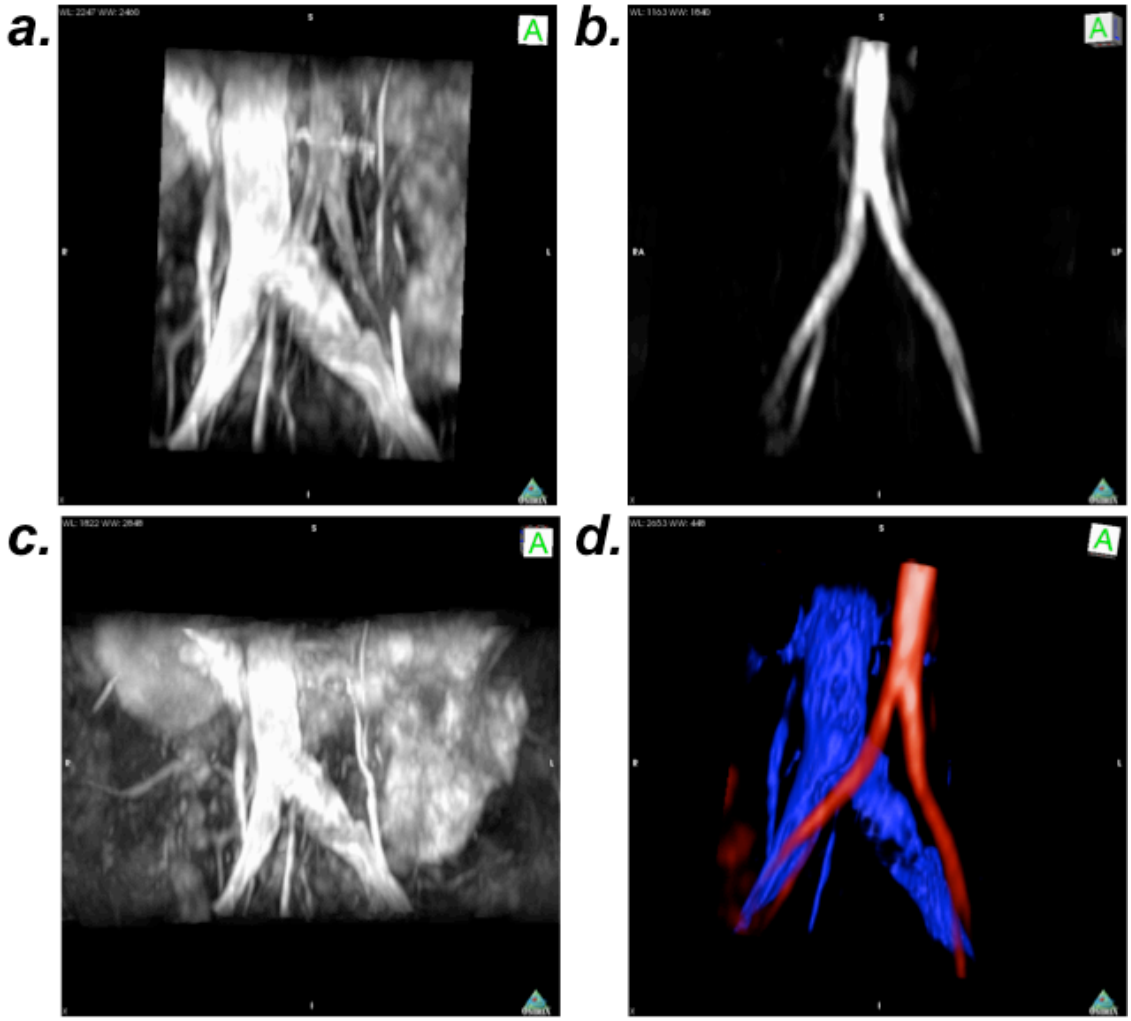

Figure 6.20- MIP reconstruction of the distal abdominal Aorta and Inferior Vena Cava (IVC) from (a) dataset acquired using b-SSFP without T2prep. (b) TIR4ASL MIP generated from a TIR4ASL protocol; (c) Subtraction of (a) and (b) showing the IVC venogram. (d) MIP reformatting showing the distal aorta and the iliac arteries in red, and the distal IVC and the iliac veins in blue

6.3.5 Conclusion and Discussion

In this chapter we demonstrate the feasibility to use a flow-independent protocol to obtain venograms in areas with very slow blood flow like the iliac veins. The b-SSFP protocol showed good visualization of the veins and arteries, however it is not possible to obtain a selective venogram using this protocol. However, the combination of b-SSFP and TIR4ASL allowed obtaining a flow-independent venogram without the use of contrast agent even in veins with very slow flowing blood.

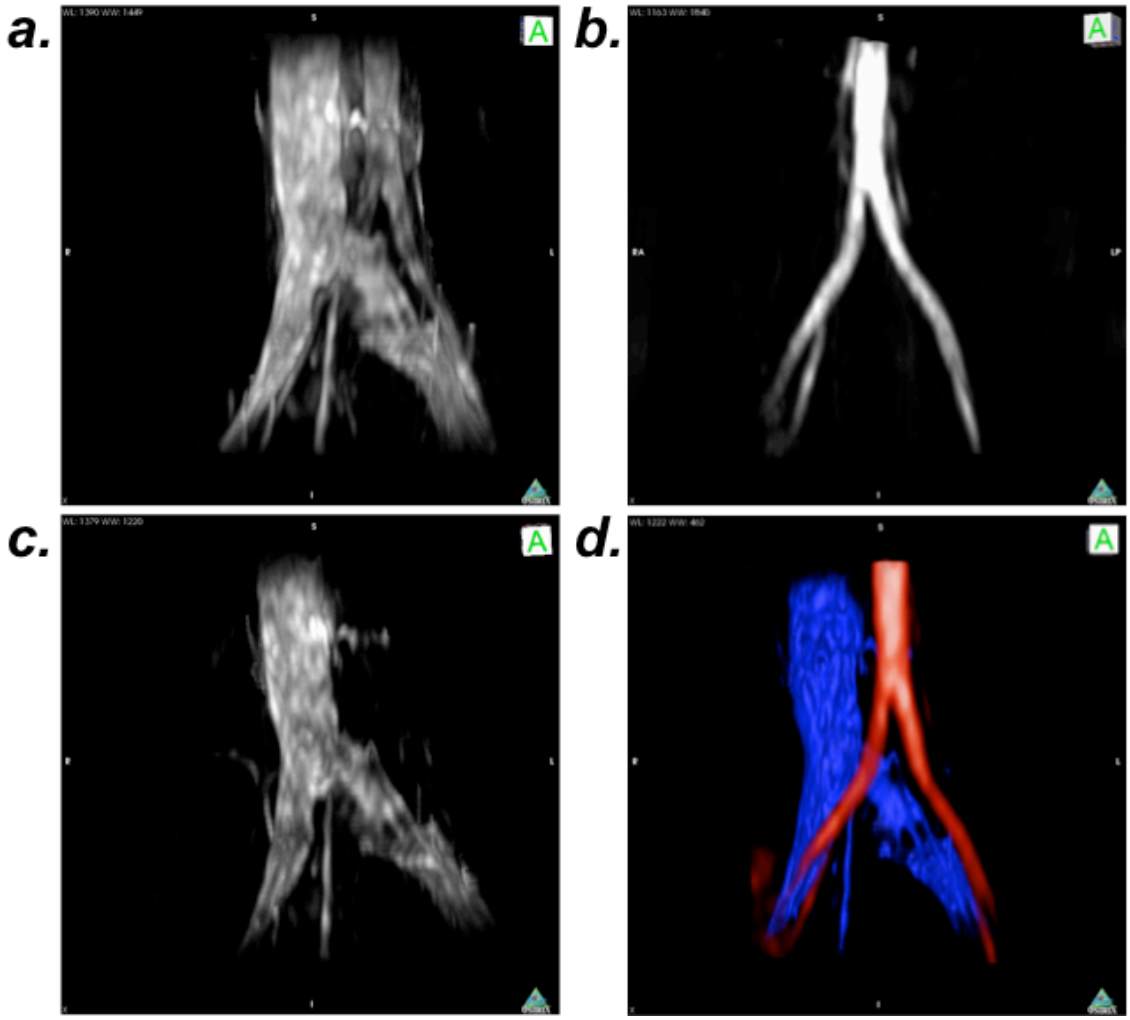

Figure 6.21- MIP reconstruction of the distal abdominal Aorta and Inferior Vena Cava (IVC) from (a) dataset acquired using b-SSFP with T2prep. (b) TIR4ASL MIP generated from the TIR4ASL protocol; (c) Subtraction of (a) and (b) showing the IVC venogram. (d) MIP reformatting showing the distal aorta and the iliac arteries in red, and the distal IVC and the iliac veins in blue

One potential limitation of this protocol is the need for two acquisitions, which effectively doubles the scan time. Nevertheless the whole protocol takes less than 15 minutes and has many advantages, such as obviation of radiation and it does not require the use of intravascular contrast agents which it a great advantage in pregnant women, children and patients with renal dysfunction.

Chapter 7 New methodology to evaluate patients with DVT

In this work we have investigated different MR imaging techniques that could facilitate the diagnosis of venous thrombosis, improve the selection criteria for thrombolytic treatment and reduce the exposure to X-ray radiation and intravenous ionizing contrast agents.

The majority of our results have been obtained in a mouse model of venous thrombosis and therefore have to be first validated in humans before new clinical guidelines for the diagnosis and therapy selection of DVT patients can be proposed. However, here we will assume that our results will be replicated in humans and based on this assumption suggest the following new diagnosis methodology for DVT patients that include our main findings (Figure 7.1).

DVT diagnosis should continue using D-Dimer and ultrasonography as the first-line diagnostic tools in patients with suspected DVT. Both techniques are non invasive, not expensive and widely available (Figure 7.1).

According to the current guidelines (Figure 1.3), DVT will be ruled out in patients with low risk of venous thrombosis and negative D-dimer (Figure 7.1). In patients with low or moderate risk and discordant results from ultrasonography and D-dimer, non-contrast enhanced MRI will be recommended in order to obtain MR venography, which should provide the same information as the currently used phlebography techniques, but without the use of iodinated contrast agents. In patients with high risk of venous thrombosis and normal ultrasonography, non-contrast MR venography would be the confirmation examination as phlebography in the current guidelines.

The proposed approach of DVT diagnosis has the advantage that is does not require X-rays or intravenous contrast media therefore could be used in children, pregnant women, older people and patients with renal dysfunction.

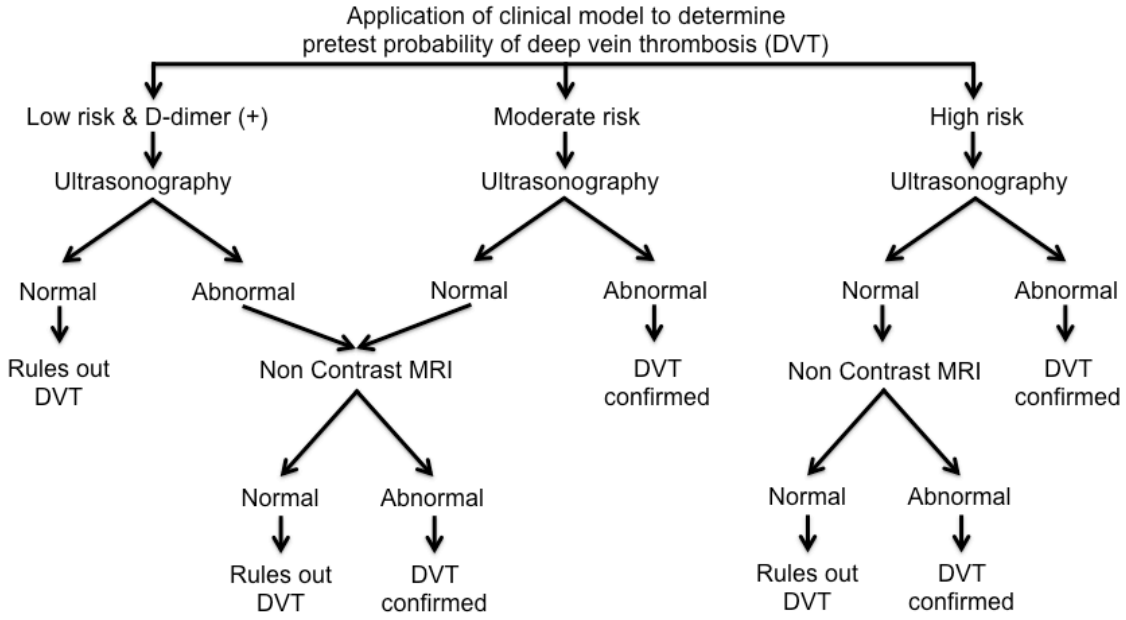

Figure 7.1- Suggested diagnostic approach in outpatients with suspected DVT without the use X-rays and intravascular contrast agent

In patients in whom DVT has been confirmed, we propose the following decision tree to choose the right treatment (Figure 7.2): Obtain a 3D T1 map of the thrombus. If the average thrombus T1 relaxation time is less than 730 ms the patient should be considered for thrombolytic therapy. This threshold had a specificity of 100% to select a mouse that will have a positive outcome post thrombolytic treatment (section 5.3). However this threshold may exclude a group of patients that would benefit from thrombolytic treatment because its sensitivity is very moderate (53%, section 5.3). In mice with thrombus T1 times longer that 823 ms our data shown that the chance of successful thrombolysis is extremely low (section 5.3). Therefore they would be managed using the current conservative approach with anticoagulation.

In patients with thrombus T1 relaxation times longer than 730 ms but shorter than 823 we propose to obtain another T1 map post EP-2104R injection in order to increase the sensitivity of the decision tree but without increase of false positive patients.

If the post-EP-2104R T1 relaxation time is shorter than 630 ms, this patient should be considered for thrombolytic therapy (Figure 7.2).

In this decision tree we are currently not considering the potential benefits of the accurate estimation of the thrombus fibrin content that may allow estimation of a patient specific

thrombolytic dose in mg per mm^3 of thrombus' fibrin content. Such patient-specific treatment could further improve the likelihood of successful thrombolysis, and reduce the potentially fatal side effects of an unnecessarily high dose of thrombolytic agent. Further studies are needed to validate this potential benefit.

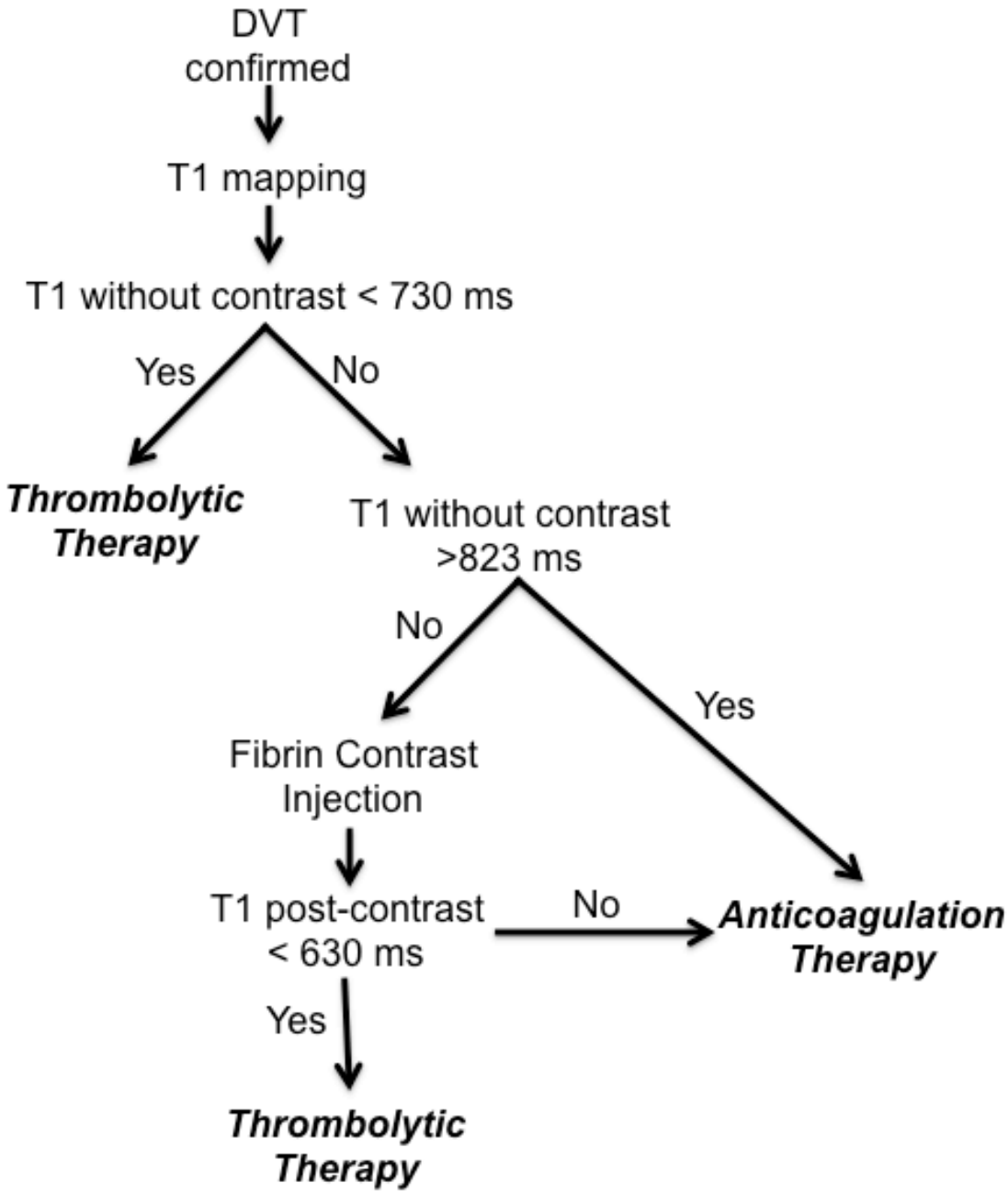

Figure 7.2- Suggested treatment decision tree for patients with confirmed venous thrombosis diseases

Chapter 8 Conclusion and Future Works

8.1 General Conclusion

In spite of the enormous disease burden associated with DVT there is still no consensus on the appropriate management of patients with this condition (1). A lack of “objective” criteria has resulted in most patients who are diagnosed with DVT being treated conservatively, often leading to re-thrombosis and chronic side effects such as PTS (7,10,24). The development of new thrombolytic drugs have stimulated the need for better diagnostic tools that allow identification of patients that are likely to benefit from these therapies while minimizing procedure related complications such as bleeding and intracerebral haemorrhage (13,17). Additionally, the actual gold standard for the diagnosis of DVT is contrast venography (phlebography) (30,31). This technique is invasive, expensive, exposes the patient to a high dose of radiation, and can cause complications related to nephrotoxicity and allergic reactions to iodinated contrast agents (32). Phlebography relies on the anatomy of the venous system and lacks physiological information. Additionally, most guidelines suggest avoiding the use of iodinated contrast agents in pregnant women, elderly and patients with renal dysfunction (33-35), who, paradoxically, are the patients with the highest risk of developing DVT (6).

Therefore there is a need for a less invasive diagnostic technique and new methodologies that provide molecular information of thrombus composition at the moment of diagnosis.

In order to study venous thrombosis we used the St Thomas’ mouse model of venous thrombosis, which is highly reproducible (>95% of animals have thrombosis), has low mortality (<1%) and produces thrombi with a similar structure to those found in man (44). We performed all our imaging studies using a clinical 3T MR scanner (Achieva Gyroscan, Philips Healthcare, Best, The Netherlands) in order to facilitate translation of our results into clinical practice.

One of the main advantages of Magnetic Resonance Imaging (MRI) over other diagnostic imaging modalities is the excellent soft tissue contrast. MR pulse sequences can be designed to emphasize different tissue properties.

In Chapter 2 we demonstrated that it is feasible to visualise mice IVC thrombus *in vivo* and obtain several MRI parameters like: MTC, ADC, T2* and T1 relaxation times of thrombus during its organization stages. We have shown that the T2* time is shortest in the very early stages of thrombus organisation because of the high content of RBCs and therefore haemoglobin and iron. This effect decreases during thrombus organisation and it is very well correlated with the decrease in the content of RBCs in the thrombus. We demonstrated that the shortening of the thrombus T1 relaxation time during its organisation is due to methemoglobin formation and the availability of free water protons in the thrombus. These findings confirm that the MR signal changes during the different stages of thrombus organisation are correlated with the biological process occurring inside the thrombus. We have shown that T1 and T2* mapping are very useful to detect different stages of thrombus organisation and therefore could be useful to guide medical decisions.

In Chapter 3 we have demonstrated that quantification of the thrombus fibrin content in a mouse model of DVT using a fibrin binding MRI contrast agent, EP-2104R, provides accurate information on the stage of thrombus organisation. The absolute decrease in thrombus T1 relaxation time post contrast and the change in the visualized thrombus enhanced volume pre and post contrast were very well correlated with the histologically measured fibrin content and provided useful information on the stage of thrombus organisation.

In Chapter 4, we used a superparamagnetic very small iron oxide particle (VSOP) to identify macrophage infiltration during thrombus organisation. Our results showed that quantification of nanoparticle uptake using T2* mapping was related with stage of thrombus organisation, however due to the presence of endogenous iron in the thrombus it was difficult to differentiate between iron from RBCs and VSOP. T2* mapping did not allow a good differentiation between both sources of iron.

In Chapter 5 we used T1 and T2* mapping and quantification of EP-2104R uptake to identify venous thrombi amenable for thrombolysis. In our mice DVT model, we demonstrate that venous thrombus with an evolution time between 7 to 10 days showed the highest rate of successful thrombolysis, while subacute (day 2) and older thrombus (day 21) responded poorly to thrombolytic therapy. This small “window of treatment” was well identified with T1mapping without pre contrast injection. However this technique did not provide good selection criteria to

minimize false positive and true negative findings. In order to increase the sensitivity and specificity of the selection criteria, we studied the predictive value of the post EP-2104R images, and found that they provided the best information to identify thrombus that has the highest likelihood of successful thrombolytic treatment outcome.

In Chapter 6, we developed a new non-contrast spin labelling sequence for Magnetic Resonance Angiography that could be used to visualize the venous systems and therefore to facilitate the diagnosis of DVT, and providing the same morphological information as phlebography, but without the exposure to X-ray and without the need for intravascular contrast agents.

Finally in Chapter 7, we proposed a new methodology for the diagnosis of DVT and a new guideline to choose the right treatment based on our results. Most of the decision algorithm could be done without the need of a contrast agent, and the use of EP-2104R is reserved for a group of cases where the thrombus relaxation time pre contrast is not sufficient to make a decision, and more information is needed to choose between invasive or conservative treatment.

The translation of our results to humans may have great potential to change current clinical management of patients suffering from DVT by improving the diagnosis and the selection criteria of patients scheduled for thrombolytic therapy.

8.2 Limitations of the study

The main limitation of our work is the use of a murine model of deep venous thrombosis. DVT is not known to occur in mouse naturally. Therefore drawing parallels to the human condition may be questionable. The thrombus in the mouse model is created in the inferior vena cava, which does not contain valves. This is in contrast to DVT in humans which generally develop in the vicinity of venous valves, and which can lead to the post-thrombotic syndrome (PTS). For both ethical and financial reasons inducing thrombi in larger animal models, including primates, has generally been reserved to testing therapy immediately prior to entering human trials. It is however likely that performing MRI on animals closer to the size of man would have been easier as thrombi could have been more readily visualised. However the St Thomas' mice model of venous thrombosis has been used for more than 15 years and it has shown similar histological and physiological characteristics compared to human venous thrombi.

We tested all venous thrombus sequences in a mouse DVT model and in in-vitro human clots. Further studies are needed to evaluate the reproducibility of our results in human venous thrombus in-vivo.

Additionally, the successful thrombolysis criterion that we have used was an arbitrary cut off of over 50% improvement in IVC blood flow. In man, outcomes of successful thrombolysis would be better measured by serial examination to include re-thrombosis rate and more importantly the development of PTS. As there are no established methods to examine PTS rates in the mouse, it is difficult to ascertain whether identification of lysable thrombi would result in better outcomes.

8.3 Future works

The main challenge of this work is to validate the results in patients. The first step would be to introduce the T1 mapping protocol without contrast agent as a routine clinical examination in all patients admitted with suspected DVT. In patients who have clinical indications of thrombolysis, the T1 relaxation time pre-treatment could be used as a predictor of the outcome that could be extended not just to recovery of venous flow after thrombolytic treatment, but also include the rate of re-thrombosis and the rate of PTS post treatment.

The use of EP-2104R in patients is currently not possible. At this time a successful Phase II studied has been finished (58) and a Phase III studied is needed in order to obtain the authorization to use this contrast in humans. However using the mice model of DVT it is still possible to improve our results. In our study we have used a constant dose of thrombolytic drugs expressed in mg per kg of mice. However, with the accurate estimation of the thrombus fibrin content, it may allow estimation of a “subject specific” thrombolytic dose in mg per mm^3 of thrombus’ fibrin content. Such subject-specific treatment could further improve the chance of successful thrombolysis, and reduce the potentially fatal side effects of an unnecessarily high dose of thrombolytic agent. Such a study could further improve our methodology and identify new clinical applications for the use of a fibrin contrast agent.

REFERENCES

1. Lopez J, Kearon C, Lee AY. Deep Venous Thrombosis. Hematology 2004:439-256.
2. Laine C, Goldmann D. The Deep Venous Thrombosis. Annals of Internal Medicine 2008:ITC1-ITC16.
3. Heit JA. The Epidemiology of Venous Thromboembolism in the Community. Arteriosclerosis, Thrombosis, and Vascular Biology 2008;28(3):370-372.
4. Prandoni P, Bilora F, Marchiori A, and Bermardi E, Petrobelli F, Lensing AW, Prins MH, Girolami A. Association between Atherosclerosis and Venous Thrombosis. N Engl J Med 2003;348:1435-1441.
5. Bagot CN, Arya R. Virchow and his triad: a question of attribution. Br J Haematol 2008;143(2):180-190.
6. Goldhaber SZ. Risk factors for venous thromboembolism. Journal of the American College of Cardiology 2010;56(1):1-7.
7. Schulman S, Lindmarker P, Holmström M, Lärfars G, Carlsson A, Nicol P, Svensson E, Ljungberg B, Viering S, Nordlander S, Leijd B, Jahed K, Hjorth M, Linder O, Beckman M. Post-thrombotic syndrome, recurrence, and death 10 years after the first episode of venous thromboembolism treated with warfarin for 6 weeks or 6 months. J Thromb Haemost 2006;4(4):734-742.
8. Heit JA, Silverstein MD, Mohr DN, Petterson TM, O'Fallon WM, Melton LJ. Predictors of survival after deep vein thrombosis and pulmonary embolism: a population-based, cohort study. Archives of internal medicine 1999;159(5):445-453.
9. Lensing A, Prandoni P, Prins M, Buller H. Deep-vein thrombosis. Lancet 1999;353:479-485.
10. Kahn SR, Ginsberg JS. Relationship between deep venous thrombosis and the postthrombotic syndrome. Arch Intern Med 2004;164(1):17-26.
11. Kahn SR. The post thrombotic syndrome. Thrombosis Research 2011;127 Suppl 3:S89-92.
12. Bergan J, Schmid-Schonbein GW, Coleridge-Smith PD, Nocolaides AN, Boisseau MR, Eklof B. Chronic Venous Disease. N Engl J Med 2006;355:488-498.
13. Patterson BO, Hinchliffe R, Loftus IM, Thompson MM, Holt PJE. Indications for catheter-directed thrombolysis in the management of acute proximal deep venous thrombosis. Arteriosclerosis, Thrombosis, and Vascular Biology 2010;30(4):669-674.
14. Spyropoulos AC, Hurley JS, Ciesla GN, de Lissovoy G. Management of acute proximal deep vein thrombosis: pharmacoeconomic evaluation of outpatient treatment with enoxaparin vs inpatient treatment with unfractionated heparin. Chest 2002;122(1):108-114.
15. Raju S, Neglen P. Chronic Venous Insufficiency and Varicose Veins. N Engl J Med 2009;360:2319-2327.
16. Kahn SR, Ginsberg JS. The post-thrombotic syndrome: current knowledge, controversies, and directions for future research. Blood Rev 2002;16(3):155-165.
17. Popuri RK, Vedantham S. The role of thrombolysis in the clinical management of deep vein thrombosis. Arteriosclerosis, Thrombosis, and Vascular Biology 2011;31(3):479-484.
18. Laiho MK, Oinonen A, Sugano N, Harjola V-P, Lehtola AL, Roth W-D, Keto PE, Lepäntalo M. Preservation of venous valve function after catheter-directed and systemic thrombolysis for deep venous thrombosis. Eur J Vasc Endovasc Surg 2004;28(4):391-396.
19. Watson LI, Armon MP. Thrombolysis for acute deep vein thrombosis. Cochrane Database Syst Rev 2004(4):CD002783.
20. Comerota AJ. The ATTRACT Trial: Rationale for Early Intervention for Iliofemoral DVT. Perspectives in vascular surgery and endovascular therapy 2010.
21. Schweizer J, Kirch W, Koch R, Elix H, Hellner G, Forkmann L, Graf A. Short- and long-term results after thrombolytic treatment of deep venous thrombosis. Journal of the American College of Cardiology 2000;36(4):1336-1343.
22. Cesarman-Maus G, Hajjar KA. Molecular mechanisms of fibrinolysis. Br J Haematol 2005;129(3):307-321.
23. Kearon C, Kahn SR, Agnelli G, Goldhaber S, Raskob GE, Comerota AJ, Physicians ACoC. Antithrombotic therapy for venous thromboembolic disease: American College of Chest Physicians Evidence-Based Clinical Practice Guidelines (8th Edition). Chest 2008;133(6 Suppl):454S-545S.

24. Klein SJ, Gasparis AP, Virvilis D, Ferretti JA, Labropoulos N. Prospective determination of candidates for thrombolysis in patients with acute proximal deep vein thrombosis. J Vasc Surg 2010;51(4):908-912.
25. Ramzi DW, Leeper KV. DVT and pulmonary embolism: Part I. Diagnosis. Am Fam Physician 2004;69(12):2829-2836.
26. Line B. Pathophysiology and Diagnosis of Deep Venous Thrombosis. Sem Nuclear Med 2001;31(2):90-101.
27. Wells PS, Anderson DR, Bormanis J, Guy F, Mitchell M, Gray L, Clement C, Robinson KS, Lewandowski B. Value of assessment of pretest probability of deep-vein thrombosis in clinical management. Lancet 1997;350(9094):1795-1798.
28. Wells P. Advances in the Diagnosis of Venous Thromboembolism. J Thromb Thrombolysis 2006;21(1):31-40.
29. Linkins LA, Bates SM, Ginsberg JS, Kearon C. Use of different D-dimer levels to exclude venous thromboembolism depending on clinical pretest probability. J Thromb Haemost 2004;2(8):1256-1260.
30. Orbell JH, Smith A, Burnand KG, Waltham M. Imaging of deep vein thrombosis. Br J Surg 2008;95(2):137-146.
31. Sidhu PS, Alikhan R, Ammar T, Quinlan DJ. Lower limb contrast venography: a modified technique for use in thromboprophylaxis clinical trials for the accurate evaluation of deep vein thrombosis. Br J Radiol 2007;80(959):859-865.
32. Gaitini D. Multimodality Imaging of the Peripheral Venous System. Int J Biomed Imag 2007;2007:1-10.
33. Thomsen HS. Guidelines for contrast media from the European Society of Urogenital Radiology. AJR Am J Roentgenol 2003;181(6):1463-1471.
34. Aspelin P, Aubry P, Fransson S-G, Strasser R, Willenbrock R, Berg KJ, Investigators NiH-RPSoI-OaL-ON-ICMS. Nephrotoxic effects in high-risk patients undergoing angiography. N Engl J Med 2003;348(6):491-499.
35. Webb JAW, Thomsen HS, Morcos SK, (ESUR) MoCMSCoESoUR. The use of iodinated and gadolinium contrast media during pregnancy and lactation. Eur Radiol 2005;15(6):1234-1240.
36. Kanne JP. Role of Computed Tomography and Magnetic Resonance Imaging for Deep Venous Thrombosis and Pulmonary Embolism. Circulation 2004;109(12_suppl_1):I-15-I-21.
37. Bates S, Ginsberg JS. Treatment Deep Vein Thrombosis. N Engl J Med 2004;351:268-277.
38. Grewal NK, Martinez JT, Andrews L, Comerota AJ. Quantity of clot lysed after catheter-directed thrombolysis for iliofemoral deep venous thrombosis correlates with postthrombotic morbidity. J Vasc Surg 2010.
39. Elsharawy M, Elzayat E. Early results of thrombolysis vs anticoagulation in iliofemoral venous thrombosis. A randomised clinical trial. Eur J Vasc Endovasc Surg 2002;24(3):209-214.
40. Enden T, Haig Y, Kløw N-E, Slagsvold C-E, Sandvik L, Ghanima W, Hafsahl G, Holme PA, Holmen LO, Njaastad AM, Sandbæk G, Sandset PM, Group CS. Long-term outcome after additional catheter-directed thrombolysis versus standard treatment for acute iliofemoral deep vein thrombosis (the CaVenT study): a randomised controlled trial. Lancet 2012;379(9810):31-38.
41. Enden T, Kløw N-E, Sandvik L, Slagsvold C-E, Ghanima W, Hafsahl G, Holme PA, Holmen LO, Njaastad AM, Sandbaek G, Sandset PM, Group CS. Catheter-directed thrombolysis vs. anticoagulant therapy alone in deep vein thrombosis: results of an open randomized, controlled trial reporting on short-term patency. J Thromb Haemost 2009;7(8):1268-1275.
42. Enden T, Sandvik L, Kløw N-E, Hafsahl G, Holme PA, Holmen LO, Ghanima W, Njaastad AM, Sandbaek G, Slagsvold C-E, Sandset PM. Catheter-directed Venous Thrombolysis in acute iliofemoral vein thrombosis--the CaVenT study: rationale and design of a multicenter, randomized, controlled, clinical trial (NCT00251771). Am Heart J 2007;154(5):808-814.
43. Ali T, Humphries J, Burnand KG, Sawyer B, Bursill CA, Channon KM, Greaves DR, Rollins B, Charo IF, Smith A. Monocyte recruitment in venous thrombus resolution. Journal of Vascular Surgery 2006;43:601-608.
44. Modarai B, Burnard KG, Humphries J, Waltham M, Smith A. The role of neovascularisation in the resolution of venous thrombus. Thromb Haemost 2005;93:801-809.

45. Wakefield TW, Myers DD, Henke PK. Mechanisms of Venous Thrombosis and Resolution. Arteriosclerosis, Thrombosis, and Vascular Biology 2008;28(3):387-391.
46. Woollard KJ, Sturgeon S, Chin-Dusting JPF, Salem HH, Jackson SP. Erythrocyte hemolysis and hemoglobin oxidation promote ferric chloride-induced vascular injury. J Biol Chem 2009;284(19):13110-13118.
47. Varma MR, Varga AJ, Knipp BS, Sukheepod P, Upchurch GR, Kunkel SL, Wakefield TW, Henke PK. Neutropenia impairs venous thrombosis resolution in the rat. J Vasc Surg 2003;38(5):1090-1098.
48. Saha P, Humphries J, Modarai B, Mattock K, Waltham M, Evans CE, Ahmad A, Patel AS, Premaratne S, Lyons OTA, Smith A. Leukocytes and the natural history of deep vein thrombosis: current concepts and future directions. Arteriosclerosis, Thrombosis, and Vascular Biology 2011;31(3):506-512.
49. Meissner M, Zierler BK, Bergelin RO, Chandler WL, Strandness DE. Coagulation, fibrinolysis, and recanalization after acute deep venous thrombosis. Journal of Vascular Surgery 2002;35(2):278-285.
50. Henke PK, Varga A, De S, Deatrick CB, Eliason J, Arenberg DA, Sukheepod P, Thanaporn P, Kunkel SL, Upchurch GR, Wakefield TW. Deep vein thrombosis resolution is modulated by monocyte CXCR2-mediated activity in a mouse model. Arteriosclerosis, Thrombosis, and Vascular Biology 2004;24(6):1130-1137.
51. Henke PK, Pearce CG, Moaveni DM, Moore AJ, Lynch EM, Longo C, Varma M, Dewyer NA, Deatrick KB, Upchurch GR, Wakefield TW, Hogaboam C, Kunkel SL. Targeted deletion of CCR2 impairs deep vein thombosis resolution in a mouse model. J Immunol 2006;177(5):3388-3397.
52. McGuinness C, Humphries J, Waltham M, Burnand KG, Collins M, Smith A. Recruitment of labelled Monocytes by Experimental Venous Thrombi. Thromb Haemost 2001;85:1018-1024.
53. Modarai B, Burnand KG, Sawyer B, Smith A. Endothelial Progenitor Cells Are Recruited Into Resolving Venous Thrombi. Circulation 2005;111(20):2645-2653.
54. Mackman N. Triggers, targets and treatments for thrombosis. Nature 2008;451(7181):914-918.
55. Modarai B, Burnand KG, Humphries J, Waltham M, Smith A. The role of neovascularisation in the resolution of venous thrombus. Thromb Haemost 2005;93(5):801-809.
56. Overoye-Chan K, Koerner S, Looby RJ, Kolodziej AF, Zech SG, Deng Q, Chasse JM, Mcmurry TJ, Caravan P. EP-2104R: A Fibrin-Specific Gadolinium-Based MRI Contrast Agent for Detection of Thrombus. J Am Chem Soc 2008;130(18):6025-6039.
57. Botnar RM, Perez AS, Witte S, Wiethoff AJ, Laredo J, Hamilton J, Quist W, Parsons EC, Vaidya A, Kolodziej A, Barrett JA, Graham PB, Weisskoff RM, Manning WJ, Johnstone MT. In vivo molecular imaging of acute and subacute thrombosis using a fibrin-binding magnetic resonance imaging contrast agent. Circulation 2004;109(16):2023-2029.
58. Vymazal J, Spuentrup E, Cardenas-Molina G, Wiethoff AJ, Hartmann MG, Caravan P, Parsons EC. Thrombus imaging with fibrin-specific Gadolinium-Based MR Contrast Agent EP2104R. Investigative Radiology 2009;44:697-704.
59. Wagner S, Schnorr J, Pilgrimm H, Hamm B, Taupitz M. Monomer-Coated Very Small Superparamagnetic Iron Oxide Particles as Contrast Medium for Magnetic Resonance Imaging: Preclinical In Vivo Characterization. Investigative Radiology 2002;37(4):167-177.
60. Taupitz M, Wagner S, Schnorr JR, Kravec I, Pilgrimm H, Bergmann-Fritsch H, Hamm B. Phase I Clinical Evaluation of Citrate-coated Monocrystalline Very Small Superparamagnetic Iron Oxide Particles as a New Contrast Medium for Magnetic Resonance Imaging. Investigative Radiology 2004;39(7):394-405.
61. Nishimura DG, Macovski A, Pauly JM, Conolly SM. MR angiography by selective inversion recovery. Magn Reson Med 1987;4(2):193-202.
62. Andia ME, Botnar RM. Arterial spin labeling angiography using a triple inversion recovery prepulse. Magn Reson Med 2012;67(2):477-483.
63. Andia ME, Botnar RM. Unenhanced MR liver circulation imaging using a Triple Inversion Recovery ASL technique. Proceedings of the 20th Meeting of the ISMRM, Melbourne, Australia 2012;A4847:1-1.
64. Brittain J, Hu BS, Wright GA, Meyer C, Macovski A, Nishimura DG. Coronary Angiography with Magnetization-Prepared T2 contrast. Magn Reson Med 1995;33:689-696.

65. Andia ME, Henningsson M, Hussain T, Phinikaridou A, Protti A, Greil G, Botnar RM. Flow-independent 3D whole heart vessel wall imaging using an interleaved T2-preparation acquisition. Magn Reson Med 2012; accepted for publication.
66. Wohner N, Sótonyi P, Machovich R, Szabó L, Tenekedjiev K, Silva MMCG, Longstaff C, Kolev K. Lytic Resistance of Fibrin-Containing Red Blood Cells. Arteriosclerosis, Thrombosis, and Vascular Biology 2011.
67. Umbreit J. Methemoglobin—It's not just blue: A concise review. Am J Hematol 2007;82(2):134-144.
68. Hentze MW, Muckenthaler MU, Galy B, Camaschella C. Two to tango: regulation of Mammalian iron metabolism. Cell 2010;142(1):24-38.
69. Carpenter J-P, He T, Kirk P, Roughton M, Anderson LJ, de Noronha SV, Sheppard MN, Porter JB, Walker JM, Wood JC, Galanello R, Forni G, Catani G, Matta G, Fucharoen S, Fleming A, House MJ, Black G, Firmin DN, St Pierre TG, Pennell DJ. On T2* magnetic resonance and cardiac iron. Circulation 2011;123(14):1519-1528.
70. Anderson LJ. Assessment of iron overload with T2* magnetic resonance imaging. Prog Cardiovasc Dis 2011;54(3):287-294.
71. Wood JC, Enriquez C, Ghugre N, Tyzka JM, Carson S, Nelson MD, Coates TD. MRI R2 and R2* mapping accurately estimates hepatic iron concentration in transfusion-dependent thalassemia and sickle cell disease patients. Blood 2005;106(4):1460-1465.
72. He T, Gatehouse PD, Smith GC, Mohiaddin RH, Pennell DJ, Firmin DN. Myocardial T2* measurements in iron-overloaded thalassemia: An in vivo study to investigate optimal methods of quantification. Magn Reson Med 2008;60(5):1082-1089.
73. Bradley WG. MR Apparearance of Hemorrhage in the Brain. Radiology 1993;189:15-26.
74. Moody AR. Direct imaging of deep-vein thrombosis with magnetic resonance imaging. Lancet 1997;350(9084):1073.
75. Jensen JH, Tang H, Tosti CL, Swaminathan SV, Nunez A, Hultman K, Szulc KU, Wu EX, Kim D, Sheth S, Brown TR, Brittenham GM. Separate MRI quantification of dispersed (ferritin-like) and aggregated (hemosiderin-like) storage iron. Magnetic resonance in medicine : official journal of the Society of Magnetic Resonance in Medicine / Society of Magnetic Resonance in Medicine 2010;63(5):1201-1209.
76. Blume U, Orbell J, Waltham M, Smith A, Razavi R, Schaeffter T. 3D T 1-mapping for the characterization of deep vein thrombosis. Magn Reson Mater Phy 2009;22(6):375-383.
77. Grossman RI, Gomori JM, Ramer KN, Lexa FJ, Schnall MD. Magnetization transfer: theory and clinical applications in neuroradiology. Radiographics 1994;14(2):279-290.
78. Henkelman RM, Huang X, Xiang Q-S, Stanisz GJ, Swanson SD, Bronskill MJ. Quantitative Interpretation of Magnetization Transfer. Magnetic Resonace in Medicine 1993;29:759-766.
79. Wolff SD, Balaban RS. Magnetization transfer imaging: practical aspects and clinical applications. Radiology 1994;192(3):593-599.
80. Henkelman RM, Stanisz GJ, Graham SJ. Magnetization transfer in MRI: a review. NMR Biomed 2001;14(2):57-64.
81. Qiao Y, Hallock KJ, Hamilton JA. Magnetization Transfer Magnetic Resonance of Human Atherosclerotic Plaques ex vivo Detects Areas of High Protein Density. J Cardiovasc Magn Reson 2011;13(1):73.
82. Lendrum A. Studies on the character and staining of fibrin. J Clin Path 1962;15:401-413.
83. Saha P, Andia ME, Blume U, Modarai B, Waltham M, Smith A, Schaeffter T, Wiethoff AJ. In Vivo Correlation of T1 and Methemoglobin in a Mouse Model of Deep Vein Thrombosis. Proceedings of the 19th Meeting of the ISMRM, Montreal, Canada 2011:A4489.
84. Stark DD, Moseley ME, Bacon BR, Moss AA, Goldberg HI, Bass NM, James TL. Magnetic resonance imaging and spectroscopy of hepatic iron overload. Radiology 1985;154(1):137-142.
85. Thulborn KR, Sorensen AG, Kowall NW, McKee A, Lai A, McKinstry RC, Moore J, Rosen BR, Brady TJ. The role of ferritin and hemosiderin in the MR appearance of cerebral hemorrhage: a histopathologic biochemical study in rats. AJR Am J Roentgenol 1990;154(5):1053-1059.
86. Gersh KC, Nagaswami C, Weisel JW. Fibrin network structure and clot mechanical properties are altered by incorporation of erythrocytes. Thromb Haemost 2009;102(6):1169-1175.
87. Wolff S, Balaban RS. Magnetization Transfer Contrast (MTC) and Tissue Water Proton Relaxation in vivo. Magn Reson Med 1989;10:135-144.

88. Stanisz GJ, Odrobina EE, Pun J, Escaravage M, Graham SJ, Bronskill MJ, Henkelman RM. T1, T2 relaxation and magnetization transfer in tissue at 3T. Magn Reson Med 2005;54(3):507-512.
89. Weber OM, Speier P, Scheffler K, Bieri O. Assessment of magnetization transfer effects in myocardial tissue using balanced steady-state free precession (bSSFP) cine MRI. Magn Reson Med 2009;62(3):699-705.
90. McLean MA, Barker GJ. Concentrations and magnetization transfer ratios of metabolites in gray and white matter. Magn Reson Med 2006;56(6):1365-1370.
91. Vidmar J, Blinc A, Sersa I. A comparison of the ADC and T2 mapping in an assessment of blood-clot lysability. NMR Biomed 2010;23(1):34-40.
92. Undas A, Ariëns RAS. Fibrin Clot Structure and Function: A Role in the Pathophysiology of Arterial and Venous Thromboembolic Diseases. Arteriosclerosis, Thrombosis, and Vascular Biology 2011.
93. Katoh M, Haage P, Wiethoff AJ, Gunther RW, Bucker A, Tacke J, Spuentrup E. Molecular Magnetic Resonance Imaging of Deep Vein Thrombosis Using a Fibrin-Targeted Contrast Agent A Feasibility Study. Invest Radiol 2009;44:146-150.
94. Spuentrup E, Buecker A, Katoh M, Wiethoff AJ, Parsons EC, Botnar RM, Weisskoff RM, Graham PB, Manning WJ, Günther RW. Molecular magnetic resonance imaging of coronary thrombosis and pulmonary emboli with a novel fibrin-targeted contrast agent. Circulation 2005;111(11):1377-1382.
95. Sirol M, Aguinaldo JGS, Graham PB, Weisskoff R, Lauffer R, Mizsei G, Chereshnev I, Fallon JT, Reis E, Fuster V, Toussaint J-F, Fayad ZA. Fibrin-targeted contrast agent for imporovement of in vivo acute thrombus detection with MRI. Atherosclerosis 2005;182:79-85.
96. Wakefield TW, Myers DD, Henke PK. Mechanisms of venous thrombosis and resolution. Arterioscler Thromb Vasc Biol 2008;28(3):387-391.
97. Nosaka M, Ishida Y, Kimura A, Kondo T. Time-dependent organic changes of intravenous thrombi in stasis-induced deep vein thrombosis model and its application to thrombus age determination. Forensic Sci Int 2009;195(1-3):143-147.
98. Weissleder R, Elizondo G, Wittenberg J, Rabito CA, Bengele HH, Josephson L. Ultrasmall superparamagnetic iron oxide: characterization of a new class of contrast agents for MR imaging. Radiology 1990;175(2):489-493.
99. Ruehm S, Corot C, Vogt P, Kolb S, Debatin J. MR Imaging of Atherosclerotic Plaque with Ultrasmall Superparamagnetic Particles of Iron Oxide in Hyperlipidemic Rabbits Circulation 2001. Circulation 2001;103:415-422.
100. Schmitz SA, Taupitz M, Wagner S, Wolf KJ, Beyersdorff D, Hamm B. Magnetic resonance imaging of atherosclerotic plaques using superparamagnetic iron oxide particles. J Magn Reson Imaging 2001;14(4):355-361.
101. Kooi ME, Cappendijk VC, Cleutjens KBJM, Kessels AGH, Kitslaar PJEHM, Borgers M, Frederik PM, Daemen MJAP, van Engelshoven JMA. Accumulation of ultrasmall superparamagnetic particles of iron oxide in human atherosclerotic plaques can be detected by in vivo magnetic resonance imaging. Circulation 2003;107(19):2453-2458.
102. Moore A, Weissleder R, Bogdanov A. Uptake of dextran-coated monocrystalline iron oxides in tumor cells and macrophages. J Magn Reson Imaging 1997;7(6):1140-1145.
103. Taupitz M, Schnorr J, Abramjuk C, Wagner S, Pilgrimm H, Hünigen H, Hamm B. New generation of monomer-stabilized very small superparamagnetic iron oxide particles (VSOP) as contrast medium for MR angiography: preclinical results in rats and rabbits. J Magn Reson Imaging 2000;12(6):905-911.
104. Vieira LM, Dusse LMS, Fernandes AP, Martins-Filho OA, de Bastos M, Ferreira MFR, Cooper AJ, Lwaleed BA, Carvalho MG. Monocytes and plasma tissue factor levels in normal individuals and patients with deep venous thrombosis of the lower limbs: potential diagnostic tools? Thrombosis Research 2007;119(2):157-165.
105. Litovsky S, Madjid M, Zarrabi A, Casscells SW, Willerson JT, Naghavi M. Superparamagnetic iron oxide-based method for quantifying recruitment of monocytes to mouse atherosclerotic lesions in vivo: enhancement by tissue necrosis factor-alpha, interleukin-1beta, and interferon-gamma. Circulation 2003;107(11):1545-1549.
106. Raynal I, Prigent P, Peyramaure S, Najid A, Rebuzzi C, Corot C. Macrophage endocytosis of superparamagnetic iron oxide nanoparticles: mechanisms and comparison of ferumoxides and ferumoxtran-10. Investigative Radiology 2004;39(1):56-63.
107. Kramer C. MR Imaging to identify the High-Risk Plaque. Am J Cardiol 2002;90:15L-17L.

108. Tang TY, Muller KH, Graves MJ, Li ZY, Walsh SR, Young V, Sadat U, Howarth SPS, Gillard JH. Iron Oxide Particles for Atheroma Imaging. Arteriosclerosis, Thrombosis, and Vascular Biology 2009:1-10.
109. Spuentrup E, Botnar RM, Wiethoff AJ, Ibrahim T, Kelle S, Katoh M, Ozgun M, Nagel E, Vymazal J, Graham PB, Günther RW, Maintz D. MR imaging of thrombi using EP-2104R, a fibrin-specific contrast agent: initial results in patients. Eur Radiol 2008;18(9):1995-2005.
110. Kahn SR, Shbaklo H, Lamping DL, Holcroft CA, Shrier I, Miron MJ, Roussin A, Desmarais S, Joyal F, Kassis J, Solymoss S, Desjardins L, Johri M, Ginsberg JS. Determinants of health-related quality of life during the 2 years following deep vein thrombosis. J Thromb Haemost 2008;6(7):1105-1112.
111. Lencioni R, Fattori R, Morana G, Stacul F. Contrast-induced nephropathy in patients undergoing computed tomography (CONNECT) - a clinical problem in daily practice? A multicenter observational study. Acta Radiol 2010;51(7):741-750.
112. Smith-Bindman R, Lipson J, Marcus R, Kim K-P, Mahesh M, Gould R, Berrington de González A, Miglioretti DL. Radiation dose associated with common computed tomography examinations and the associated lifetime attributable risk of cancer. Arch Intern Med 2009;169(22):2078-2086.
113. Shah PK. Screening asymptomatic subjects for subclinical atherosclerosis: can we, does it matter, and should we? Journal of the American College of Cardiology 2010;56(2):98-105.
114. Creasy JL, Price RR, Presbrey T, Goins D, Partain CL, Kessler RM. Gadolinium-enhanced MR angiography. Radiology 1990;175(1):280-283.
115. Haustein J, Niendorf HP, Krestin G, Louton T, Schuhmann-Giampieri G, Clauss W, Junge W. Renal tolerance of gadolinium-DTPA/dimeglumine in patients with chronic renal failure. Investigative Radiology 1992;27(2):153-156.
116. Prince MR, Arnoldus C, Frisoli JK. Nephrotoxicity of high-dose gadolinium compared with iodinated contrast. J Magn Reson Imaging 1996;6(1):162-166.
117. Sam AD, Morasch MD, Collins J, Song G, Chen R, Pereles FS. Safety of gadolinium contrast angiography in patients with chronic renal insufficiency. J Vasc Surg 2003;38(2):313-318.
118. Ledneva E, Karie S, Launay-Vacher V, Janys N, Derray G. Renal Safety of Gadolinium-based Contrast Media in PAtients with Chronic Renal Insufficiency. Radiology 2009;250(3):618-628.
119. Thomsen HS. Gadolinium-based contrast media may be nephrotoxic even at approved doses. Eur Radiol 2004;14(9):1654-1656.
120. Sadowski EA, Bennett LK, Chan MR, Wentland AL, Garrett AL, Garrett RW, Djamali A. Nephrogenic systemic fibrosis: risk factors and incidence estimation. Radiology 2007;243(1):148-157.
121. Miyazaki M, Lee VS. Nonenhanced MR Angiography. Radiology 2008;248(1):20-43.
122. Roditi G, Maki JH, Oliveira G, Michaely HJ. Renovascular imaging in the NSF Era. J Magn Reson Imaging 2009;30(6):1323-1334.
123. Stuber M, Bornert P, Spuentrup E, Botnar RM, Manning WJ. Selective three-dimensional visualization of the coronary arterial lumen using arterial spin tagging. Magn Reson Med 2002;47(2):322-329.
124. Katoh M, Spuentrup E, Barmet C, Stuber M. Local re-inversion coronary MR angiography: Arterial spin-labeling without the need for subtraction. J Magnetic Resonance Imaging 2008;27(4):913-917.
125. Yarnykh VL, Yuan C. T1-insensitive flow suppression using quadruple inversion-recovery. Magn Reson Med 2002;48(5):899-905.
126. Heit JA. The Epidemiology of Venous Thromboembolism in the Community. Arterioscler Thromb Vasc Biol 2008;28(3):370-372.
127. Dixon WT, Sardashti M, Castillo M, Stomp GP. Multiple Inversion Recovery Reduces Static Tissue Signal in Angiograms. Magnetice Resonance in Medicine 1991;18:257-268.
128. Scheffler K, Lehnhardt S. Principles and applications of balanced SSFP techniques. Eur Radiol 2003;13(11):2409-2418.
129. Hänicke W, Vogel HU. An analytical solution for the SSFP signal in MRI. Magn Reson Med 2003;49(4):771-775.
130. Botnar RM, Stuber M, Danias PG, Kissinger KV, Manning WJ. Improved coronary artery definition with T2-weighted, free-breathing, three-dimensional coronary MRA. Circulation 1999;99(24):3139-3148.